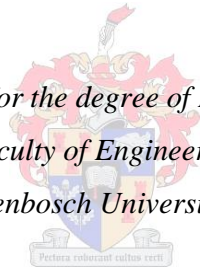


Next generation high-temperature gas reactors: A failure methodology for the design of nuclear graphite components

by

Michael Philip Hindley

*Dissertation presented for the degree of Doctor of Philosophy
in the Faculty of Engineering at
Stellenbosch University*



Supervisor: Dr D Blaine

Co-supervisor: Prof. AA Groenwold

March 2015

DECLARATION

By submitting this dissertation electronically, I declare that the entirety of the work contained therein is my own, original work, that I am the sole author thereof (save to the extent explicitly otherwise stated), that reproduction and publication thereof by Stellenbosch University will not infringe any third party rights and that I have not previously, in its entirety or in part, submitted it for obtaining any qualification.

Date: 21 November 2014

Copyright © 2015 Stellenbosch University

All rights reserved

ABSTRACT

This thesis presents a failure evaluation methodology for nuclear graphite components used in high-temperature gas reactors. The failure methodology is aimed at predicting the failure of real parts based on the mechanical testing results of material specimens. The method is a statistical failure methodology for calculating the probability of failure of graphite components, and has been developed and implemented numerically in conjunction with a finite element analysis. Therefore, it can be used on any geometry and load configuration that can be modelled using finite element analysis.

The methodology is demonstrated by mechanical testing of NBG-18 nuclear grade graphite specimens with varying geometries under various loading conditions. Some tests were developed as an extension of the material characterisation, specifically engineered to assess the effect of stress concentrations on the failure of NBG-18 components.

Two relevant statistical distribution functions, a normal distribution and a two-parameter Weibull distribution are fitted to the experimental material strength data for NBG-18 nuclear graphite. Furthermore, the experimental data are normalised for ease of comparison and combined into one representative data set. The combined data set passes a goodness-of-fit test which implies the mechanism of failure is similar between data sets.

A three-parameter Weibull fit to the tensile strength data is only used in order to predict the failure of independent problems according to the statistical failure methodology. The analysis of the experimental results and a discussion of the accuracy of the failure prediction methodology are presented. The data is analysed at median failure load prediction as well as at lower probabilities of failure.

This methodology is based on the existence of a “link volume”, a volume of material in a weakest link methodology defined in terms of two grouping criteria. The process for approximating the optimal size of a link volume required for the weakest link failure calculation in NBG-18 nuclear graphite is demonstrated. The influence of the two grouping criteria on the failure load prediction is evaluated. A detailed evaluation of the failure prediction for each test case is performed for all proposed link volumes. From the investigation, recommended link volumes for NBG-18 are given for an accurate or conservative failure prediction.

Furthermore, failure prediction of a full-sized specimen test is designed to simulate the failure condition which would be encountered if the reactor is evaluated independently. Three specimens are tested and evaluated against the predicted failure. Failure of the full-size component is predicted realistically but conservatively. The predicted failure using link volume values for the test rig design is 20% conservative. The methodology is based on the Weibull weakest link method which is inherently volume dependent. Consequently, the conservatism shows that the methodology has volume dependency as experienced in the classic Weibull theory but to a far lesser extent.

OPSOMMING

Hierdie tesis beskryf 'n metode wat gebruik kan word om falings in kern grafiet komponente te voorspel. Hierdie komponente word in hoë temperatuur gas reaktore gebruik. Die falings metodologie beoog om die falings van regte komponente te voorspel wat gebaseer is op meganiese toets resultate van materiaal monsters. Dit is 'n statistiese falings metodologie wat die waarskynlikheid van faling vir grafiet komponente bereken. Die metode is numeries ontwikkel en geïmplementeer deur middel van die eindige element metode, dus kan die metodologie toegepas word op enige geometrie en belastingsgeval wat dan gemodelleer kan word deur gebruik te maak van eindige element metodes.

Die metodologie word gedemonstreer deur gebruik te maak van NBG-18 kern grafiet toets monsters. Sommige van hierdie toetse is ontwikkel as 'n uitbreiding van die materiaal karakterisering wat spesifiek ontwerp is om die effek van die spannings konsentrasies op die faling van die NBG-18 komponente te evalueer.

Twee relevante statistiese verspreiding funksies word gekoppel aan die eksperimentele sterkte data van die NBG-18 kern grafiet, naamlik 'n normale verspreiding en 'n twee-parameter Weibull verspreiding. Die data stelle word ook genormaliseer vir gemak van vergelyking en gekombineer in een verteenwoordigende data stel. Die gekombineerde data stel slaag 'n korrelasie toets wat impliseer dat die meganisme van faling soortgelyk is tussen die data stelle.

'n Drie-parameter Weibull korrelasie op die trek toets monsters word gebruik vir die statistiese falings metodologie. Die analise van die eksperimentele resultate sowel as 'n bespreking van die akkuraatheid van die faling voorspelling metodologie word voorgelê. Die data word geanaliseer by gemiddelde faling voorspelling asook by laer voorspellings van falings. Hierdie metode is gebaseer op die bestaan van 'n "ketting volume" wat die volume van 'n materiaal wat gebruik word in die swakste ketting voorstel en koppel aan die metodologie.

'n Metode vir die benadering van die ketting volume word voorgestel en daaropvolgend gebruik om die ketting volume te bereken vir NBG-18. 'n Gedetailleerde evaluasie van die falings voorspelling vir elke toets geval word uitgevoer vir die voorgestelde ketting volumes. Gebaseer op hierdie ondersoek is voorgestelde ketting volumes vir NBG-18 gegee vir beide akkurate en konserwatiewe falings voorspellings.

Verder was 'n volgrootte strukturele toets ontwikkel om dieselfde falings omstandighede te simuleer wat verwag is gedurende normale werking van die reaktor. Drie monsters word getoets en geëvalueer teen die voorspelde faling vir beide die berekende ketting volume groottes. Faling van die volgrootte komponente word realisties asook konserwatief voorspel. Die voorspelling is 20% konserwatief. Die metodologie is gebaseer op die Weibull metode wat inherent volume afhanklik is; gevolglik dui die konserwatisme aan dat die metodologie oor

volume afhanklikheid beskik soos ondervind word in die klassieke Weibull teorie, maar tot 'n baie kleiner mate.

ACKNOWLEDGEMENTS

This thesis is dedicated to my wife Sabrina, son Liam and daughter Mia. Their patience and support throughout the completion of this work was unparalleled and for that I am explicitly thankful.

I would like to express my sincere gratitude towards the following persons and entities:

- The PBMR project: It was an honour and a great learning experience to be able to work on this project for so long and a great tragedy that funding was discontinued before it was completed.
- Mark Mitchell for his guidance and insight into all aspects of this work even after leaving PBMR (Pty) Ltd.
- The PBMR (Pty) Ltd structural analysis team, Christiaan Erasmus, Jaco du Plessis and Ross McMurtry, who all contributed to the structural analysis and meticulously ensured that every result was verified and validated.
- The PBMR (Pty) Ltd materials graphite team, Mary Fechter (now Botha-Snead) and Dr Shahed Fuzluddin, who effortlessly provided the required information.
- The Submerge Publishers editing team: Thank you for your professional support and unequivocal editing expertise through the “back and forths” over the last four years.

TABLE OF CONTENTS

Declaration.....	i
Abstract.....	ii
Opsomming.....	iii
Acknowledgements	v
1. Introduction	1
1.1 Background of high-temperature gas reactors and Pebble Bed Modular Reactor	1
1.2 High-temperature gas reactor moderator	2
2. Background on graphite failure.....	4
2.1 Graphite characteristics.....	4
2.2 Nuclear graphite strength	4
2.3 Stress and strain	5
2.4 Statistical fracture models	7
2.5 Failure criteria for tensile test problems.....	10
2.6 Failure criteria for multi-axial test problems	11
3. Hypothesis	13
4. History of work	15
5. Methodology	16
6. Observations in the statistical analysis of NBG-18 nuclear graphite strength tests [77]	18
6.1 Introduction	18
6.2 Methodology	19
6.3 Results.....	22
6.3.1 Tensile test	22
6.3.2 Flexural test	23
6.3.3 Compressive test	23
6.4 Statistical data fitting	27
6.5 Normalisation of data	29
6.6 Summary	30

7.	A numerical stress based approach for predicting failure in NBG-18 nuclear graphite components with verification problems [78]	32
7.1	Introduction	32
7.2	Material reliability	34
7.3	Failure calculation method	35
	7.3.1 Assessment method	36
	7.3.2 Stress calculation.....	36
	7.3.3 Volume definitions.....	37
	7.3.4 Algorithm for calculation of probability of failure	37
7.4	Verification	40
	7.4.1 Geometry	40
	7.4.2 Mesh convergence.....	40
	7.4.3 Acceptance criteria	40
7.5	Results.....	43
	7.5.1 Mesh refinement	44
	7.5.2 Observations at a failure load of 50% probability of failure	44
	7.5.3 Full range failure probability predictions	44
7.6	Conclusion	51
8.	Optimisation of the link volume for weakest link failure prediction in NBG-18 nuclear graphite [79]	52
8.1	Introduction	52
8.2	Methodology	54
	8.2.1 Test cases	54
	8.2.2 Failure methodology	55
	8.2.3 Optimisation methodology.....	59
8.3	Results.....	60
	8.3.1 Response surface	60
	8.3.2 Optimisation volume results	62
8.4	Discussion: Individual test case error prediction	63
	8.4.1 Unpenalised individual test case predictions	64
	8.4.2 Penalised individual test case predictions	66
8.5	Summary	66
8.6	Conclusion	69
9.	Failure prediction of full-size reactor components from tensile specimen data on NBG-18 nuclear graphite [80]	70
9.1	Introduction	70
9.2	Numerical framework	72

9.3	Verification experiments.....	75
9.3.1	Tensile testing.....	75
9.3.2	Full-size specimen testing.....	75
9.3.3	Failure methodology implementation.....	78
9.3.4	Material properties and assumptions.....	78
9.4	Results.....	79
9.4.1	Stress results.....	79
9.4.2	Failure prediction results.....	81
9.4.3	Full range predictions.....	84
9.5	Conclusion.....	86
10.	Concluding remarks.....	87
11.	Discussion of published work.....	90
12.	References.....	92
A.	Appendix: Geometric layout optimisation of graphite reflector components [103].....	99
A.1	Introduction.....	99
A.2	Background.....	100
A.2.1	Automated analysis system.....	100
A.3	Proposed layout improvements.....	102
A.3.1	Baseline design.....	102
A.3.2	Proposed design.....	105
A.4	Results.....	106
A.4.1	Stress intensity.....	106
A.4.2	Full power years.....	107
A.4.3	Baseline design.....	107
A.4.4	Proposed design.....	110
A.5	Further development.....	114
A.6	Conclusion.....	119
B.	Appendix: Test case descriptions.....	120
C.	Appendix: Test case prediction at lower probabilities of failure.....	126
C.1	Best estimate failure predictions.....	126
C.1.1	General trends and observations at median failure load.....	130
C.2.1	Group observations at median failure load.....	130
C.2	Effect of finite element mesh refinement on prediction trends.....	134

D. Appendix: MATLAB implementation of failure methodology 136

LIST OF FIGURES

Figure 3-1: Representation of graphite structure	14
Figure 6-1: TS normal distribution fit.....	23
Figure 6-2: TS Weibull distribution fit.....	24
Figure 6-3: FS normal distribution fit.....	24
Figure 6-4: FS Weibull distribution fit.....	25
Figure 6-5: CS normal distribution fit	25
Figure 6-6: CS Weibull distribution fit	26
Figure 6-7: CS visual bimodal Weibull identification	26
Figure 7-1: Flow chart of algorithm	41
Figure 7-2: Prediction for 50% PoF	45
Figure 7-3: VP-00 (tensile specimen) Weibull probability failure prediction plot .	49
Figure 7-4: VP-01 (four-point bending test) Weibull probability failure prediction plot.....	50
Figure 7-5: VP-02 (compression specimen) Weibull probability failure prediction plot.....	50
Figure 8-1: Flow diagram of failure methodology highlighting grouping criteria..	57
Figure 8-2: Unpenalised error (RMS average) function	61
Figure 8-3: Penalised error (RMS average) function penalised by 0.5 for error larger than 1.00	62
Figure 8-4: Unpenalised failure prediction results.....	65
Figure 8-5: Penalised failure prediction results for load factors exceeding 1.00.	68
Figure 8-6: Penalised failure prediction results for load factors exceeding 1.06.	68
Figure 9-1: Flow diagram of failure methodology highlighting grouping criteria..	74
Figure 9-2: Vertical section through the upper central reflector [126].....	76
Figure 9-3: Central reflector corner block [126].....	77
Figure 9-4: Full-size reactor component test rig setup [127]	77
Figure 9-5: Symmetry model maximum principal stresses (TS)	80
Figure 9-6: Minimum principal stresses (CS)	80
Figure 9-7: MDE stress using compression to tensile ratio	81
Figure 9-8: Actual failure locations [127].....	82

Figure 9-9: MDE stress distribution for integration volume used for failure calculation below 60.3% load factor	85
Figure 9-10: Full range prediction.....	85
Figure A-1: Example of workflow set up in ISight to create a post-process and report on a completed analysis.....	103
Figure A-2: View of baseline SR design	104
Figure A-3: View of a single layer of the SR made up by the baseline reflector blocks.....	104
Figure A-4: View of an SR design utilising control rod block and key block	105
Figure A-5: View of a single layer of the SR made up of the control rod blocks and key blocks	106
Figure A-6: Maximum stress intensity anywhere in the baseline block at a given time. Blue line (+) for stress under normal operation. Red line (*) for stress at shutdown.	108
Figure A-7: Predicted failure probability for the baseline block at a given time. Blue line (+) for stress under normal operation. Red line (*) for stress at shutdown.....	108
Figure A-8: Stress intensity contour plot of block at predicted end of life	109
Figure A-9: Stress intensity contour plot of the baseline block at 18 FPY	109
Figure A-10: Stress intensity contour plot of the proposed control rod block at 18 FPY.....	110
Figure A-11: Stress intensity contour plot of the proposed key block at 18 FPY	110
Figure A-12: Maximum stress intensity anywhere in the proposed control rod block at a given time. Blue line (+) for stress under normal operation. Red line (*) for stress at shutdown.....	111
Figure A-13: Maximum stress intensity anywhere in the proposed key block at a given time. Blue line (+) for stress under normal operation. Red line (*) for stress at shutdown.....	111
Figure A-14: Predicted failure probability for the proposed control rod block at a given time. Blue line (+) for stress under normal operation. Red line (*) for stress at shutdown.....	112
Figure A-15: Predicted failure probability for the proposed key block at a given time. Blue line (+) for stress under normal operation. Red line (*) for stress at shutdown.	112
Figure A-16: Stress intensity contour plot of block at predicted end of life	113
Figure A-17: Stress intensity contour plot of block at predicted end of life	113
Figure A-18: Stress intensity contour plot of block at predicted end of life	114

Figure A-19: Stress intensity contour plot of block at predicted end of life	114
Figure A-20: Improved geometry using curved edges	115
Figure A-21: Maximum stress intensity of curved sided control rod block	116
Figure A-22: Life prediction of curved sided control rod block.....	116
Figure A-23: Stress intensity contour plot of curved sided control rod block	117
Figure A-24: Maximum stress intensity of curved sided key block	117
Figure A-25: Life prediction of curved sided key block.....	118
Figure A-26: Stress intensity contour plot of curved sided key block	118
Figure C-1: Back off limit failure prediction	129
Figure C-2: Cumulative distribution plot for VP-01 with a log scale for clarity at low failure probabilities: comparing test data with predictions for two finite element meshes of different refinement	135

LIST OF TABLES

Table 6-1: Data sets used and number of tests performed	20
Table 6-2: Statistical data fit parameters	27
Table 6-3: A-D GOF values	27
Table 6-4: GOF test with bottom 2% of data removed	28
Table 6-5: GOF test for bottom 10% of data	29
Table 6-6: Normalised statistical fit.....	30
Table 6-7: GOF for combined data set	30
Table 7-1: Material parameters used for the failure calculations	35
Table 7-2: Breakdown of the experimental VP.....	42
Table 7-3: Test case geometry descriptions	46
Table 8-1: Test case geometry descriptions [78]	54
Table 8-2: Optimisation results.....	63
Table 8-3: Significant digits affecting grouping criteria for unpenalised grouping	63
Table 8-4: Failure prediction for unpenalised results	64
Table 8-5: Failure prediction for penalised results	67
Table 8-6: Obtained link volume values for NBG-18 failure prediction	69
Table 9-1: Obtained link volume grouping values for NBG-18 failure prediction	73
Table 9-2: Statistical information of test cases.....	75
Table 9-3: NBG-18 material properties used in the FE model [128].....	78
Table 9-4: Material parameters used in the failure calculation	79
Table 9-5: Normalised statistical fit.....	79
Table 9-6: Predicted failure loads for various meshes	83
Table 9-7: Results for failure prediction	83
Table 11-1: Comparison between Initial grouping criteria and optimal reactor design values	90
Table A-1: Speed up experienced due to automation of process.....	101
Table B-1: VP-00 test cases.....	120
Table B-2: VP-01 test cases.....	121
Table B-3: VP-19 test cases.....	121
Table B-4: VP-15 test cases.....	122
Table B-5: VP-17 test cases.....	122

Table B-6: VP-18 test cases.....	123
Table B-7: VP-12 Geometry 1, test direction 1 test cases.....	123
Table B-8: VP-12 Geometry 1, test direction 2 test cases.....	124
Table B-9: VP-12 Geometry 2, test direction 1 test cases.....	124
Table B-10: VP-12 Geometry 2, test direction 2 test cases.....	125
Table C-1: Predicted failure loads and load scales for each test case	126

LIST OF ABBREVIATIONS

<i>Abbreviation or Acronym</i>	<i>Definition</i>
3D	Three-dimensional
A-D	Anderson-Darling
AGR	Advanced gas-cooled reactor
ASME	American Society of Mechanical Engineers
AVR	Arbeitsgemeinschaft Versuchsreaktor
CS	Compressive strength
CSs	Core structures
CSC	Core structure ceramics
CTE	Coefficient of thermal expansion
DPP 200	Demonstration Power Plant 200° MWt
DPP 400	Demonstration Power Plant 400° MWt
FE	Finite element
FEA	Finite element analysis
FPY	Full power years
FS	Flexural strength
GOF	Goodness of fit
HTGR	High-temperature gas reactors
HTTR	High-temperature test reactor
K-S	Kolmogorov-Smirnov
LEFM	Linear Elastic Fracture Mechanics
LFOP	Leap-frog optimisation
MDE	Maximum deformation energy
Mgs	Maximum grain size
PBMR	Pebble Bed Modular Reactor
PIA	Principle of Independent Action
PoF	Probability of failure
PoS	Probability of survival
RMS	Root mean square
RSS	Reserve shutdown system
SR	Side reflector
THTR	Thorium High-Temperature Reactor
TS	Tensile strength
VP	Verification problem

LIST OF SYMBOLS

<i>Symbol</i>	<i>Definition</i>
A	Crack size
α	Significance
D	Diameter
h_o	Characteristic grain size
K_{IC}	Fracture toughness
$\eta_V(\sigma)$	Crack-density function
m_V	Shape parameter
M	Weibull shape parameter
P_f	Probability of failure
P_s	Probability of survival
V	Volume
V_o	Characteristic volume
V_e	Effective volume
V_{tot}	Total volume of the component
N	Total number of test cases
Σ	Stress
σ_1, σ_2 and σ_3	Three components of principal stress
σ_f	Maximum stress
σ_v	Stress intensity
σ_o	Weibull scale parameter
Σt	Tensile rupture stress
Σc	Compressive rupture stress
S_c	Characteristic strength
S_o	Weibull strength threshold
S_o'	Adjusted Weibull strength threshold
σ_j	Deformation Energy (MDE) stress j
Θ	Angle to grain direction
ν	Poisson's ratio
R	Ratio of mean tensile to mean compressive strength
f	Load factor
F	Compressive to tensile multiplier
P	Penalty
C	Prescribed limit

1. INTRODUCTION

1.1 Background of high-temperature gas reactors and Pebble Bed Modular Reactor

Nuclear energy is a viable alternative to fossil fuel for power generation and a process heat source. Throughout the world, governmental organisations and private sectors are under increasing pressure to reduce global warming and endorse sustainable resources that lower the emission of greenhouse gases into the atmosphere. Renewable energy sources are offering a viable peak load solution. However, the fact remains that nuclear energy is an immediately available and significant source of base load power that does not cause extensive global warming [1].

One of many nuclear designs currently being investigated is high-temperature gas cooled reactors (generally known as HTGRs). These reactors offer a clean, compact and modular design with high cycle efficiencies and high levels of nuclear safety. They are generally much smaller in power and core power density than other reactors. However, due to limitations on the size of the reactor core due to the low power density, these systems are most effective as modular designs where a large number of units can be combined to supply electricity, steam or process heat. The considerable cost advantages of designing these systems in modular clusters were already identified by Reutler and Lohnert [2] in 1984.

HTGR technology was pioneered in the late sixties in Germany and it first took shape in the form of the Arbeitsgemeinschaft Versuchsreaktor (AVR) [3]. The AVR was an experimental reactor that operated for 22 years after going online in 1967. Walmsley [4] presents an overview of the historical aspects of HTGRs that were designed and built before the Chernobyl incident. He finds that the first demonstration projects, namely Dragon (UK), the AVR (Germany) and Peach Bottom (USA), either worked well or extremely well. They proved the basic HTGR concept and, in the case of the AVR, operated for 22 years with a high reliability. Two of the larger systems, Thorium high-temperature reactor (THTR) (Germany) and Fort St Vrain (USA), both suffered from technical problems and operated for short periods only. Walmsley indicates that these technical issues were easily overcome, but due to political pressure after the Chernobyl incident, both systems were shut down [4]. This was a major setback to the development of nuclear power stations and heralded a long period of ceased development on this front in the Western world.

In the East, however, the development of HTGRs was not completely abandoned. The 166 MW Tokai Commercial Power Plant in Japan has been operating for over 30 years and the high-temperature engineering test reactor (HTTR) went critical for the first time in 1997 [5]. In 2000, China built a 10 MW research reactor that has also been operating very successfully since 2003 [6]. With global warming becoming the new political hot topic, the focus is again on

nuclear power as a source of energy, with the requirement of developing safe nuclear energy. The inherent safety features that HTGR technology offers, together with no carbon dioxide (CO₂) emission levels, make it an environmentally attractive alternative to fossil-based power generation technologies.

Due to this change in sentiment towards nuclear power, Eskom (the major electricity utility in South Africa) became interested in HTGR technology. The HTGR design was resurrected in South Africa in 1999. Since then, South Africa was at the forefront in the development of this technology for 11 years. The Pebble Bed Modular Reactor (PBMR) project was a joint commercial and government venture, utilising this technology to design a 400 MW demonstration plant, initiated in 2001 [7]. Over the course of the project, the design strategy shifted to ensure a more marketable reactor, and a 200 MW design was effected. The PBMR concept evolved from the Interatom HTR-Modul reactor design, which is a high-temperature, helium-cooled nuclear reactor with fully-ceramic spherical fuel elements and graphite as structural material [2]. In 2010, the PBMR project was stopped due to financing and the commercial plant was never built. Additionally, the 2011 Fukushima accident will most probably further delay the development of nuclear power generation worldwide.

The inherent safety characteristics of the HTGR is that the mode of reactor control, for safety can be designed to utilise solely the basic laws of physics, inherent material properties and physical geometry.. This means that, in the event of a loss of cooling, the reactor will automatically shut down without the insertion of control rods or deployment of other shutdown systems. This feature is one of the most important inherent safety features of this type of nuclear power generation technology. The ceramic composition of the fuel has the added advantage that the fuel elements can operate safely up to 1 200°C and can withstand loss of cooling events with maximum fuel temperatures of up to 1 600°C.

1.2 High-temperature gas reactor moderator

The core of a modular HTGR is constructed of ceramic materials capable of withstanding extremely high temperatures. This capability is an essential property for the passive heat removal feature of the modular HTGR designs [8]. Graphite, the predominant ceramic material, serves as an effective neutron moderator and reflector with low neutron absorption properties. A neutron moderator is a medium that slows down fast neutrons and turns them into thermal neutrons which are essential to sustain the nuclear chain reaction in the reactor [9]. The graphite moderator also forms a major structure, which houses the core and provides a guide to channel the coolant into the fuel region where the main heat generation takes place due to the fission reaction. The core reflectors are made from graphite due to its good thermal, neutron/physical, and mechanical properties (ultimate tensile strength = 20 MPa from room temperature up to 2 000°C). It further provides access for control and safety shut-off devices in addition to its thermal and neutron physics role [10]. In the PBMR design, the core structures (CSs) are the structural components around the core that define

and maintain the pebble bed geometry. The graphite is in the form of blocks that are stacked vertically to create columns.

The long-term behaviour of graphite under the temperature and irradiation conditions representative of the designs is a complex function of the initial material properties and service conditions [8]. In the older nuclear reactors, such as UK Magnox, the graphite moderators were made from highly anisotropic graphite, while more recent graphite moderator designs are made from uniform semi-isotropic graphite. Extensive experience with graphite behaviour under irradiation has been obtained through experimental testing as well as the operation of HTGR plants. In addition, a large body of experience is available from the operation of the CO₂ cooled reactors (Magnox and advanced gas-cooled reactor [AGR]) developed in the UK [8]. The effect of irradiation damage on nuclear graphite has been studied extensively and is an ongoing process on various grades of graphite. For comprehensive details on the neutron irradiation effect on graphite, see Marsden [10].

Typically, when graphite is subject to damage by fast neutron irradiation, the following occurs [11]:

- The material experiences dimensional changes, initially shrinking and later swelling. This dimensional change is not isotropic, but is transversely anisotropic as per the virgin material.
- The elastic modulus of the material changes. The change in elastic modulus is coupled with a corresponding change in the material's strength.
- The coefficient of thermal expansion (CTE) changes.
- The thermal conductivity changes.
- The material is subject to creep under stress at significantly lower temperatures than what graphite would creep at without irradiation.

These changes in material properties induce stress in the graphite core components. Designers are required to ensure structural integrity of the graphite core components with these induced stresses during operation.

NBG-18 nuclear grade graphite was the material selected for the neutron moderator for the core structures, and consequently the reflector, of the reactor of the PBMR plant.

2. BACKGROUND ON GRAPHITE FAILURE

2.1 Graphite characteristics

A detailed explanation of graphite characteristics can be found in Smith [12], Burchell [13] and Pierson [14]. Graphite is a composite material consisting of the coke filler particles and the carbonised pitch or resin binder (which is usually coal-tar pitch) [15]. When nuclear graphite is manufactured, easily graphitised materials, such as petroleum coke, are commonly chosen as a filler material [16]. Nuclear graphite is made from a very pure feed stock to minimise impurities that can absorb neutrons parasitically during reactor operation. The graphite is manufactured by compressing the coke and impregnating it with the binder at temperature. Depending on the type of graphite, this process is repeated more than once to ensure a low void density. Finally, with a heat treatment at 2 800-3 000°C, which is called graphitisation, the material becomes fully graphitised and the result is a material which is all graphite [17].

Different grades of graphite can show widely different textures, pore size distributions and the presence of sub-critical crack-like formations [18]. Graphite contains a variety of defect structures and typically has between 15-25% void volume [15]. Nuclear grade graphite refers to bulk graphite of accepted and characterised properties with high purity (such as low boron content) certified for use inside a nuclear reactor core [15].

Graphite can be manufactured with different average grain sizes. Coarse-grained material has grains larger than 4 mm. Medium-grained material has grains smaller than 4 mm. Fine-grained material has grains smaller than 100 µm and superfine, ultrafine and microfine materials have grains smaller than 50 µm, 10 µm and 2 µm respectively [15]. Manufactured graphite can be extruded or moulded and, subsequently, the resulting grain structure will have a biased orientation [15]. Material properties are often measured relative to the forming direction. NBG-18 is a vibration-moulded, medium-grained nuclear graphite designed to be near-isotropic.

2.2 Nuclear graphite strength

Graphite is similar to other brittle materials in that it does not exhibit plastic deformation and shows wide scatter in strength [19]. However, graphite differs from other classically brittle materials in that it can show non-linear stress strain response and it exhibits acoustic emission (damage accumulation from micro cracking) prior to rupture [18, 20]. Nuclear graphite is a quasi-brittle material and has the presence of inherent defects, such as crystal irregularities, pores, inclusions and cracks. These defects can reduce the material strength and act as stress-concentrating features and can thus initiate material failure under sufficient applied stress. The variability of defect size and orientation and their random distribution through the material volume leads to a large scatter in experimental

material strength test measurements. This makes it difficult to define the load at which the material will fail.

For specimens of a similar size, graphite is stronger in compression than bending and stronger in bending than in tension. It is more likely that low void content, fine-grained materials are more brittle than high void content, larger-grained materials [15]. Brittle and quasi-brittle structures are those in which failure is caused by a fracture rather than plastic yield. Failure initiates in a zone in which progressive distributed cracking or other damage takes place [21]. Regardless of the processing, the strength of graphite is always stochastic and nominally identical specimens will display a significant fluctuation in strength from the population mean [15]. The structural integrity of nuclear graphite has historically been assessed with either a probabilistic approach such as the Weibull theory [22-38] or the fracture mechanics approach [23, 39-52].

A statistical approach can be used to decide upon an acceptably low risk of part failure and by defining the material strength using an appropriate probability density function; the part can be designed to meet the required specification. Kennedy [26] identified the phenomenon of disparate flaws where the test data are consistent with a bimodal normal distribution. He proposed a combination of binomial and order statistics to represent these disparate flaws. Price [28] identifies various relations between strength and the position at which the sample was removed from the billet.

In the probabilistic approach, the Weibull theory is mainly used. In the Weibull theory, the strength of a brittle solid is assumed to be controlled by flaws and this has potential uses in the engineering design of load-bearing structures made from brittle materials, because it relates the probability of failure (PoF) to the volume of material under load, the stress gradient and the multi-axial stress states [28]. However, Brocklehurst and Darby [22], Mitchell *et al.* [35] and Price [28] unanimously concluded that the Weibull model is inconsistent with the material behaviour of nuclear graphite. Strizak [30], and Kennedy and Eatherly [26] investigated the size and volume of nuclear graphite and also posited trends inconsistent with the Weibull theory. Modification of the Weibull theory for nuclear graphite is proposed by Schmidt [37] and Ho [24] to account for this behaviour.

The other approach for assessing failure is the use of fracture mechanics. This approach has been studied by Burchell [44], Ho *et al.* [23], Kennedy and Kehne [46], Wang and Liu [49], Sakai *et al.* [52] and Becker *et al.* [42].

2.3 Stress and strain

Many materials display a rheological behaviour which, until a certain point, may be considered as elastic perfectly plastic. To quantify the behaviour of materials, experimental results are used as a basis for the quantification of the rheological behaviour. The oldest and simplest model to describe this phenomenon is the one defined by Robert Hooke in 1678 (Hooke's law) [53], which states that strain is proportional to stress. In this case, the mathematical model of proportionality is

used in the definition of the material behaviour. Graphite shows very little plastic deformation before failure.

To predict the stress conditions under which ductile materials fail in three-dimensional (3D) stress states, the most widely-accepted theory is the Mohr criterion [54]. This theory is based on the intrinsic strength curve of the material. This curve is defined as the envelope of the Mohr circles, defined by the maximum and minimum principal stresses (σ_1 and σ_3) of the stress states which cause rupture. These stresses may be related to the rupture stresses measured in experimental tensile and compressive tests, σ_t and σ_c [54]. Further expansion of this leads to the Von Mises cylinder that touches the Tresca prism in ductile materials.

For brittle materials, which are stronger in compression than in tension, an approximation to the Von Mises criterion which was proposed by Drucker and Prager [55] in 1952. This criterion is represented by a cone with a circular cross-section which touches the Mohr-Coulomb pyramid in three of its six longitudinal edges.

In graphite, the moulding preferentially orients the graphite grains in such a way that the strength response is transversely isotropic. Strength anisotropy is a physical phenomenon that should be considered in a general failure theory for graphite. The relationship between the stress strain behaviour of graphite and the weakest link theory has to be established in order to formulate representative failure criteria.

Drucker-Prager has been used as a representative model for nuclear graphite [41-43, 51, 52].

Schmidt [29, 36, 48, 56, 57] introduced a modified Weibull approach which uses an equivalent stress. The formulation of the stress is on the hypothesis that the elastic energy per unit volume, stored in a given material element at the moment of fracture, is equal to the energy that is stored in the uni-axially loaded test specimen at fracture [56]. The compressive strength (CS) of graphite is almost four times higher than the tensile strength (TS). To enable direct comparison of tensile and compressive stress components, all compressive principal stress components are converted to their equivalent tensile stress (in terms of likelihood to cause failure) by multiplying it by a weighting factor (R) equal to the ratio of mean tensile to mean CS.

To quantify the elastic strain energy, the stress intensity (σ_v) is introduced, as defined by Schmidt [37] and calculated in accordance with Equation 2-1. This equivalent stress intensity is also referred to as the maximum deformation energy (MDE) stress.

$$\sigma_v = \sqrt{\bar{\sigma}_1^2 + \bar{\sigma}_2^2 + \bar{\sigma}_3^2 - 2 \cdot \nu \cdot (\bar{\sigma}_1 \cdot \bar{\sigma}_2 + \bar{\sigma}_1 \cdot \bar{\sigma}_3 + \bar{\sigma}_2 \cdot \bar{\sigma}_3)} \quad (2-1)$$

where

$\sigma_1, \sigma_2, \sigma_3$ are the three components of principal stress

$\sigma_i = f \cdot \sigma_j$ where j is the direction of the principal stress _{1,2,3}

$f = 1$ if σ_i is a tensile stress

$f = R$ if σ_i is a compressive stress (where R is the ratio of mean tensile to mean CS)

ν = Poisson's ratio

MDE stress for NBG-18 nuclear grade graphite was shown as a valid approach by Roberts [20].

2.4 Statistical fracture models

The question arises as to whether design methodologies, developed to describe classically brittle material failure, are suitable for graphite or whether alternative approaches are needed [15]. A review of failure methodologies that may be applicable to graphite is done by Tucker *et al.* [18], Tucker and McLachlan [58], and Nemeth [15].

Fracture in engineering materials can be represented by two different methodologies, namely series systems and parallel systems. Series systems assume the material to be represented by a chain of links. It is assumed that the links are connected in series in such a manner that the structure fails whenever any of the links fail.

Parallel system models assume the links are arranged in parallel. When one link fails, the load is redistributed to the remaining links. Subsequently, the remaining links carry a higher load but the structure may still survive. The structure fails when the distributed load increases to the extent that none of the links survive.

Failure of brittle materials, such as glasses and ceramics, are represented well by series systems. Materials with fibre strains, like fibre-reinforced composite materials, are realistically represented by parallel failure systems.

Fracture of brittle materials usually initiates from flaws [59] which are randomly distributed in the material. The strength of the specimen depends on the size of the major flaw which varies from specimen and orientation. Therefore, the strength of brittle materials is described by a probability function [60-63]. Experiments show that the probability of failure increases with load and also with the size of the specimens [60, 61, 64]. The fact that the probability increases with the increase in size is due to the fact that it is more likely to find a major flaw in a large specimen than in a small one. Subsequently, the mean strength of larger specimens is lower than the mean strength of smaller specimens. This size effect on strength is the most prominent and relevant consequence of the statistical behaviour of strength in brittle materials [65]. Traditionally, the size effect in failure of brittle material has been explained using Weibull's statistical theory [7, 66]. The Weibull theory is extended to multidimensional solids by the weakest

link model for a chain proposed by Peirce [67] and also used the extreme value statistics originated by Tippett [68]. This size effect, however, is not valid for nuclear graphite as shown by Strizak [69].

In Weibull's theory, the failure is determined by the minimum value of the strength of the material [70]. The weakest link model assumes a series system in which the structure is analogous to a chain of links. Each link may have a different limiting strength. When a load is applied to the structure to such an extent that when the weakest link fails, then the structure fails [65].

Consider a chain containing many links and assume that failure is due to any number of independent and mutually exclusive mechanisms. Each link involves an infinitesimal PoF. Discretise the component into incremental links. The probability of survival (PoS) $(P_s)_i$ of the i^{th} link is related to the PoF, $(P_f)_i$ of the i^{th} link by $(P_s)_i = [1-(P_f)_i]$ and the resultant PoS of the whole structure is the product of the individual PoSs [15]:

$$P_s = \prod_{i=1}^n (P_s)_i = \prod_{i=1}^n [1 - (P_f)_i] \quad (2-2)$$

$$= \prod_{i=1}^n \exp[-(P_f)_i] = \exp \left[- \sum_{i=1}^n (P_f)_i \right]$$

Equation 2-2 describes a series system where failure of any one element means failure of the whole system. The PoF (P_f) is defined as the complement of the PoS (P_s) . This equation leads to the prediction of a size effect. When more links are added to the chain, the PoF increases for a given load. The system is weaker due to the probability of having a weaker link present. To maintain the same PoF, the load would have to be decreased. The prediction of size effect is an important consideration when trying to determine an appropriate probabilistic distribution to model a material [15].

Waloddi Weibull [66, 71] formulated the distribution function associated with his name. He applied the weakest link concept to a solid volume of a brittle material rather than to a fibre as was done by Peirce [67]. Weibull [71] assumed that, for a volume V under a uni-axial stress, the PoF of the component may be described as Equation 2-3:

$$P_{fV} = 1 - P_{sV} = 1 - \exp[-\eta_V(\sigma)V] \quad (2-3)$$

In Equation 2-3, V as a subscript denotes a quantity that is a function of volume. $\eta_V(\sigma)$ is referred to as the crack-density function and indicates the number of flaws per unit volume having a strength equal to or less than σ . If the stress magnitude is a function of location, then substituting into Equation 2-3 yields the following [71]:

$$P_{fV} = 1 - \exp \left[- \int_V \eta_V(\sigma) dV \right] \quad (2-4)$$

Weibull then introduced a power function for the crack-density function $\eta_V(\sigma)$ in Weibull [71] as shown in Equation 2-5:

$$\eta_V(\sigma) = \frac{1}{V_o} \left(\frac{\sigma}{\sigma_o} \right)^{m_V} = \left(\frac{\sigma}{\sigma_{oV}} \right)^{m_V} \quad (2-5)$$

In Equation 2-5, V_o represents a characteristic volume, which is assumed to be a unit volume. This is a two-parameter Weibull distribution which inherently allows for a possibility of failure at any small load [64]. With the two-parameter model, the scale parameter σ_o corresponds to the stress level where 63.21% of tensile specimens with unit volumes would fracture [15]. The scale parameter σ_{oV} has dimensions of *stress•volume*^{1/m} where m_V is the shape parameter (Weibull modulus), a dimensionless parameter that measures the degree of strength variability [66]. As m_V increases, the dispersion is reduced. These parameters are considered to be material properties and are used to calculate failure in the material. The two-parameter Weibull equation can be expressed as Equation 2-6:

$$P_{fV} = 1 - \exp \left[- V_e \left(\frac{\sigma_f}{\sigma_{oV}} \right)^{m_V} \right] \quad (2-6)$$

where σ_f is the maximum stress in the component and V_e is known as the effective volume. For discrete volumes, Weibull's formula can be expressed as Equation 2-7:

$$P_f = 1 - \exp \left\{ - \sum_{j=1}^n \left(\frac{\sigma_j}{\sigma_o} \right)^m V_j \right\} \quad (2-7)$$

where σ_o = Weibull scale parameter and has units of *stress•volume*^{1/m}. This parameter is geometry-dependent. It is claimed in almost every experimental work on ceramics that the strength is Weibull distributed [65].

2.5 Failure criteria for tensile test problems

One approach for assessing failure in materials with inherent defects is the use of fracture mechanics. This approach has been studied by numerous researchers. Some theories behind graphite failure are based on the microstructure. An early model was developed by Buch [72] for fine-grain aerospace graphite. The Buch model was further developed and applied to nuclear graphite by Tucker *et al.* [18]. The Tucker *et al.* [18] model assumes that graphite consists of an array of cubic particles representative of the material's filler particle size. Within each block or particle, the graphite was assumed to have a randomly oriented crystalline structure, through which basal plane cleavage may occur when a load is applied. This was later expanded. The Burchell model [44] was specifically developed for graphite and combines fracture mechanics with a physics-based microstructural description of graphite failure. It directly incorporates specific graphite features such as the grain size, pore size, pore distribution, particle fracture toughness, graphite density and specimen size (size effect) into the model. With Burchell's model assuming transgranular fracture, the PoF of an individual graphite grain, i , ahead of a crack tip and oriented at an angle θ to the grain direction, is given by Equation 2-8:

$$P_{\tilde{i}}(\sigma, a) = \frac{4}{\pi} \cos^{-1} \left(\frac{K_{Ic}}{\sigma \sqrt{\pi a}} \right)^{1/3} \quad (2-8)$$

where K_{Ic} is the grain fracture toughness, a is the crack size and σ is the remote applied tensile stress. For details on the model see Burchell [44], although this method is cumbersome in the amount of material parameters required. This model has been proven to be valid for multiple grades of graphite [44].

Ho [24] introduces a scale parameter to the weakest link formulation. This is shown in Equation 2-9:

$$P_{fV} = 1 - \exp \left[-V \left(\frac{\sigma}{\sigma_{ov} f(h_o, d)} \right)^{m_v} \right] \quad (2-9)$$

$$f(h_o, d) = \frac{2}{\pi} \cos^{-1} \left(\frac{h_o}{d} \right)$$

In Equation 2-9, h_o is the characteristic grain size and d is the diameter of the specimen. Tucker and McLachlan [58] explained that the fall-off of strength with a small diameter was because the characteristic flaw size penetrates a greater fraction of the specimen diameter.

2.6 Failure criteria for multi-axial test problems

With the Weibull weakest link methodology, the chain of links is only defined for a one-dimensional stress state. Subsequently, to formulate a weakest link theory for a three-dimensional (3D) stress field, further work is required. Barnett [73] proposes a method called the Principle of Independent Action (PIA) in which it is assumed that each of the principal stress directions contribute independently to the failure of the component. The PIA criterion is expressed as Equation 2-10:

$$P_{fV} = 1 - \exp \left[- \frac{1}{\sigma_{oV}^{m_V}} \int_V (\sigma_1^{m_V} + \sigma_2^{m_V} + \sigma_3^{m_V}) dV \right] \quad (2-10)$$

In Equation 2-10, the Weibull theory is expanded for a multi-axial stress state where σ_1 , σ_2 and σ_3 are the three components of principal stress, and m_V is the shape parameter (Weibull modulus). The Weibull equation assumes that catastrophic crack propagation initiates from a critically-loaded flaw; however, it does not describe the physical mechanism behind this. Batdorf [39, 40] incorporates linear elastic fracture mechanics (LEFM) into the Weibull theory. Batdorf developed his theory for aerospace-grade graphite, which is a finer-grained material than nuclear grade material. Batdorf provided an improved physical basis for failure by incorporating an assumed crack geometry, mixed-mode fracture criterion and a crack orientation function [15].

Schmidt [36-38, 48, 56] introduces a volume normalisation into Equation 2-6, as shown in Equation 2-11:

$$P_f = 1 - \exp \left\{ - \sum_{j=1}^n \left(\frac{\sigma_j}{\sigma} \right)^m \frac{V_j}{V_{tot}} \right\} \quad (2-11)$$

where

P_f = component failure probability

σ_j = MDE stress j

σ = characteristic strength of the tensile test specimens

m = Weibull shape parameter

V_{tot} = total volume of the component

V_j = volume of element j

n = number of elements

This was developed to empirically fit the data from graphite rupture experiments that did not correlate well to the traditional Weibull distribution. This method works well on problems with uniform stress fields of various sizes. Caution must

be exercised when using this volume normalisation [15]. For example, Equation 2-11 predicts that the PoF of a notched rod under tensile load will change as the length of the rod is changed [15]. All of the methods listed have their own limitation in applicability.

3. HYPOTHESIS

In the design of safety-critical parts for nuclear applications, it is desirable to be able to quantify the part probability of failure (PoF) and thus ensure that the risk of failure is acceptably low. To achieve this, any failure assessment methodology adopted for graphite parts in a nuclear core has to employ a level of conservatism.

If a part is to be made of a brittle material like graphite, which has a significant variability in strength, it may not be possible to do this using a deterministic design approach. Alternatively, a probabilistic approach can be used to determine an acceptably low risk of part failure and, by defining the material strength using an appropriate probability density function, to design the part to meet the required specification. The variability of measured strength in nuclear graphite also suggests that using a probabilistic design approach is well suited to model failure for this material. A statistical approach can be used to decide upon an acceptably low risk of part failure and, by defining the material strength using an appropriate probability density function, the part can be designed to meet the required specification.

Due to the manufacturing process, graphite forms a very unique microstructure consisting of the coke filler particles and the carbonised pitch binder. Thus far, several of the failure methodologies on nuclear graphite are based on this microstructure of the material.

However, when performing strength tests on graphite, the macroscopic rheological response of the material is measured. It has generally been observed that a test sample needs to be larger than a certain volume before consistent test values are obtained. Ho [24] shows a grain-size effect where the strength of graphite decreases drastically as the specimen diameter decreases to a grain size; Strizak [30] obtains a similar effect. Ho [24] states that the grain size effect is minimised as the specimen diameter is 10 to 15 times the maximum grain size (Mgs). For NBG-18 Yoon *et al.* [74] show no significant volume effect on tensile strength tests.

A change in philosophy is proposed where the failure criterion is based on the measured macroscopic homogeneous rheological material response, rather than the microstructure. It is suggested that when the volume of material becomes significant, dissipation of deformation energy through the material (composite material consisting of the coke filler particles and the carbonised pitch) creates a uniform mechanical response in the material. This uniform response can be used to formulate a failure methodology that is applicable to parts larger than the minimum volume. Figure 3-1 shows a representation of the microstructure of nuclear graphite in a volume hereafter referred to as “link volume” – the volume of material required to reproduce a uniform rheological response in the material.

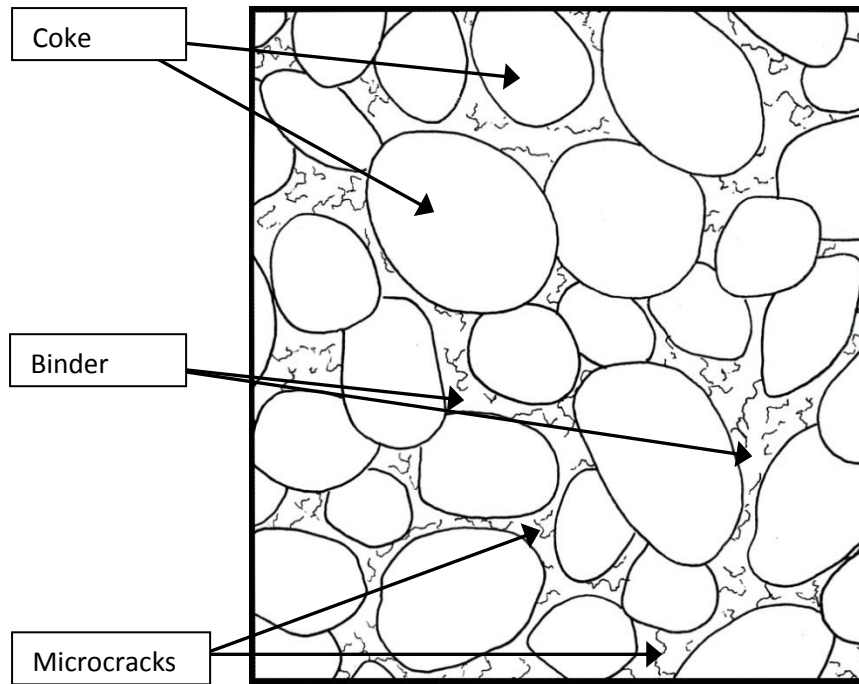


Figure 3-1: Representation of graphite structure

In the design of a reactor core like the Pebble Bed Modular Reactor (PBMR), the real components are far larger than the minimum volume used in testing. Therefore, these components should react with homogeneous mechanical properties. It is proposed that, by using this macroscopic homogeneous material response, a representative failure model can be approximated in such a way that this can be extended for use on graphite under irradiated conditions.

4. HISTORY OF WORK

In 2004, the Pebble Bed Modular Reactor (PBMR) commissioned a material characterisation programme in order to establish an acceptance criterion for manufactured nuclear graphite parts as well as verify a design methodology for these nuclear graphite parts. Initially, the design methodology was based on KTA 3232 [75], a design methodology and criterion for graphite parts. Preliminary results in 2005 indicated that Schmidt's method [36, 48, 56], which was used in KTA 3232 [75], was non-conservative on the failure load on some of the components. The scope of testing was expanded continuously to try to establish the design methodology of which the failure criteria were an integral part.

The author investigated existing methodologies on the available test data. It was found that none of the methodologies were capable of making reasonably accurate or conservative failure predictions on all test cases. Very few methods had the capability of handling three-dimensional (3D) stress distribution in irradiated analyses. Based on the above findings, a number of tests were designed to assess the effect of stress concentrating features on graphite components. Implementation of the testing and supporting tests were conducted by the PBMR team. This material testing and modelling research took place from 2004 until 2009. This was done in a stepwise process; tests were designed and performed over five years. After each test was conducted, finite element analysis (FEA) models were built by the author and verified by the PBMR team to determine the stress in the component. Various methodologies, including ones newly invented by the author were compared with the real failure loads. In early 2008, the author established a method that can accurately or conservatively predict the failure for the complex components by only using the tensile test data. In July 2008, the decision was made by the PBMR to release the author's new method into the public domain to gain regulator acceptance for the methodology. In February 2009, the method and verification problems (VPs) were presented to the American Society of Mechanical Engineers' (ASME's) Codes and Standards Committee. The method was accepted for inclusion in the new section of the code that was completed and published in 2010 [76]. The development of the author's methodology with a detailed description of the underlying fundamental theories upon which it is based is now presented for consideration of a doctoral thesis, along with supporting experimental data.

This thesis is presented as a collection of four separate published papers. All the papers were completed by the author after leaving PBMR (Pty) Ltd. Recognition for input by peers is given by naming them as co-authors on the publications. Mark Micthell provided technical insight and suggestions into the development of the programming framework used in the calculations. Christiaan Erasmus and Ross McMurtry provided independent verification and validation to each of the FEA models used. In all four the publications, the University of Stellenbosch co-authors reviewed the work, highlighted omitted information and provided guidance in writing and structuring the papers prior to submission.

5. METHODOLOGY

The approach used in this work is to formulate a failure assessment methodology based on the macroscopic homogeneous material behaviour of NBG-18 graphite. For the methodology to be applicable to the design of reactor components it needs to be able to handle material models used to model damage in nuclear graphite during the operation of a reactor. Subsequently, the failure methodology needs to be based on either the deformation field or the stress field in the component. The methodology proposed is based on the stress field. The full details of the failure methodology is presented in the following sections. Each section deals with a fundamental underlying part of the failure methodology and was written as a separate paper.

Section 6 [77] deals with the variability in material strength. The results from Section 6 [77] are used as the Weibull parameters used in the failure calculation. This section also searches for a bimodal distribution (disparate flaws initially shown by Price [28]) which would affect failure at low probabilities. The disparate flaws increase the risk of material failure significantly at low probabilities. Subsequently, this is of great concern when designing components for nuclear reactors. One of the data sets is found to have a bimodal distribution; however, its variance is smaller than those of the other data sets.

Section 7 [78] contains the failure methodology, its implementation and the results of predicting failure. Figure 7-2 plots the predicted load scale corresponding to a probability of failure (PoF) of 0.5 (50%). Due to limited space, only the crucial results were shown in Hindley *et al.* [78]. For completeness, all the results not included in Hindley *et al.* [78] are shown in Appendix C. Figure C-1 plots the predicted load scale corresponding to 10^{-2} and 10^{-4} for each of the test cases.

Section 8 [79] details the influence of the two grouping criteria used in the failure calculation. These criteria are the values used in the grouping of the stress results to define the size of the link volume used in failure calculation. The section proposes a method for approximating the size of the link volume from experimental results and sets forth to calculate the size for NBG-18 nuclear graphite. The size of the calculated link volume correlates with the gauge diameter size effect experimentally seen by Ho [24]. Two link volume sizes are calculated for NBG-18: one for a test rig design and one for a reactor component design.

Section 9 [80] uses all the results from the previous sections to independently predict failure on a full-size reactor component. A full-size specimen structural test was developed to simulate the same failure conditions expected during normal operation of the reactor. The full-size specimen is a component designed for use in the Pebble Bed Modular Reactor (PBMR) core. This component is almost one hundred times larger than the tensile test specimen, has a different geometry and experiences a different loading condition to the standard tensile test specimen. Failure of the full-size component is predicted realistically, but

conservatively. Thus, real reactor components can be safely designed using data obtained from standard tensile testing. This section provides independent verification of the proposed method.

6. OBSERVATIONS IN THE STATISTICAL ANALYSIS OF NBG-18 NUCLEAR GRAPHITE STRENGTH TESTS [77]

Michael P Hindley*, Mark N Mitchell*, Deborah C Blaine** and Albert A Groenwold**

*Formerly Pebble Bed Modular Reactor (Pty) Ltd., P.O. Box 9396, Centurion, South Africa 0046

**Department of Mechanical and Mechatronics Engineering, Stellenbosch University, Private Bag X1, Matieland 7602

Keywords

Nuclear graphite, NBG-18, statistical strength

Abstract

The purpose of this paper is to report on the selection of a statistical distribution chosen to represent the experimental material strength of NBG-18 nuclear graphite. Three large sets of samples were tested during the material characterisation of the Pebble Bed Modular Reactor and core structure ceramics materials. These sets of samples are tensile strength, flexural strength and compressive strength measurements. A relevant statistical fit is determined and the goodness of fit is also evaluated for each data set. The data sets are also normalised for ease of comparison and combined into one representative data set. The validity of this approach is demonstrated. A second failure mode distribution is found on the compressive strength test data. Identifying this failure mode supports the similar observations made in the past. The success of fitting the Weibull distribution through the normalised data sets allows us to improve the basis for the estimates of the variability. This could also imply that the variability on the graphite strength for the different strength measures is based on the same flaw distribution and thus a property of the material.

6.1 Introduction

Quasi-brittle materials, like nuclear graphite, exhibit a large scatter of strength measurements which make it difficult to define the exact load at which the material will fail [78]. Typically, a statistical distribution should be used to characterise the material strength. Furthermore, for specimens of a similar size, graphite is stronger in compression than bending, and stronger in bending than tension. Experimental results published by Strizak demonstrate that the strength of medium-grained near-isotropic graphite is independent of the volume for practical sample sizes [30].

The mechanical design of the graphite moderator and reflector blocks of a high-temperature gas reactor (HTGR), like the Pebble Bed Modular Reactor (PBMR), requires a detailed knowledge of the statistical distribution of the strength of graphite [28]. The statistical data fit can be used in design work to assess the likelihood of graphite reactor core components failing during operation.

It is difficult to predict the failure of a graphite component from small specimen tests, even without considering the complexity of irradiation damage [81]. Attempting to predict the strength of parts is further compounded by the following phenomena:

- Kennedy and Eatherly [26] identify multiple flaw populations in the material. They designated the major population of flaws as the background flaw distribution. A smaller population of so-called disparate flaws results in higher probabilities of failure at the low end of the distribution. This phenomenon further compounds the attempt to predict part failure from small specimen data. Kennedy and Eatherly [26] observed that the test data are consistent with a bimodal normal distribution. Kennedy and Eatherly [26] proposed a combination of binomial and order statistics to represent these disparate flaws.
- Price [28] and Mitchell *et al.* [35] show various relations between strength and the position at which the sample was removed from the billet.

A statistical approach can, however, be used to decide upon an acceptably low risk of part failure and to define the material strength using an appropriate probability density function and a modified Weibull weakest link calculation.

6.2 Methodology

During the material characterisation of the PBMR core structure ceramics (CSC) materials [82], a significant amount of strength data was recorded for tensile strength (TS), flexural strength (FS) and compressive strength (CS). These data were taken from a broad selection of green batches, graphitisation charges, billets and locations in the billets of material manufactured under an in-house quality management system to ensure a statistically significant characterisation of the material. Although other tests were performed, the statistical analysis reported here only concerns itself with these three data sets since they are the only data sets with significant amounts of data for statistical analysis. The data sets and the number of tests performed are shown in Table 6-1.

Table 6-1: Data sets used and number of tests performed

<i>Data Set</i>	<i>Number of Tests Performed</i>
TS	370
FS	292
CS	228

Weibull's theory, in which the strength of a brittle solid is assumed to be controlled by flaws, has potential uses in the engineering design of load-bearing structures made from brittle materials. It affects this control by relating probability of failure (PoF) to the volume of material under load, the stress gradient and multi-axial stress states [28].

NBG-18 is vibration-moulded graphite produced to be near-isotropic. The analysis of statistical properties was performed, ignoring the orientation and position of the test sample. This approach is contradictory to the recommendations formed by Price [28], but was judged as acceptable as the sampling and specimen extraction plans ensured that approximately equal numbers of specimens were removed in each direction and from all locations within the billet. Furthermore, this ensured that no single portion of the data set dominated the results.

For the purpose of this study, the statistical distribution underlying the strength data was assumed to be either a normal distribution or a two-parameter Weibull distribution. The distributions are fitted to the data set and then compared to how well they fit the data. The data fits are done by using the MATLAB statistical toolbox's built-in functions. The choice of distribution function is first evaluated by visual comparison and then by an Anderson-Darling (A-D) goodness of fit (GOF) test.

The normal distribution, also known as a Gaussian distribution, is a continuous probability distribution that is often used as a first approximation to describe results that tend to cluster around a single mean value [83]. The graph of the associated probability density function is a bell shape and is known as the Gaussian function. The normal distribution is the most prominent probability distribution encountered in statistics and is applicable to a large amount of phenomena encountered in nature. The bell shape of the normal distribution makes it a convenient choice for modelling a large variety of random variables encountered in practice. For this reason, the normal distribution is a logical choice for a statistical evaluation on experimental results. The normal distribution is described in Equation 6-1.

$$f(x) = \frac{1}{\sqrt{2\pi\sigma^2}} e^{-\frac{(x-\mu)^2}{2\sigma^2}} \quad (6-1)$$

In Equation 6-1 μ is the mean (the average of all the values) and σ^2 is the variance (the measure of the width of the distribution around the mean). The

normal distribution is a symmetric distribution with similar amounts of data points on each side of the mean value.

Weibull [66, 71] formulated the distribution function associated with his name. He applied the weakest link concept to a solid volume of a brittle material. A Weibull distribution is a skewed distribution generally used for life estimates in failure analysis. The distribution is aimed at accuracy in the low tail of the distribution and subsequently allows for accurate failure forecast at very low load. The Weibull distribution is described in Equation 6-2.

$$f(x) = \left(\frac{x}{S_c}\right)^{m-1} \cdot \frac{m}{S_c} \cdot e^{-\left(\frac{x}{S_c}\right)^m}; x > 0 \quad (6-2)$$

The part can then be designed to meet the required specification. This is primarily supported by work completed in Germany [36, 37, 56] and South Africa [78].

A more fundamental consideration is whether a physical basis consistent with graphite failure can be associated with a particular distribution and if that distribution or model can be used to make other predictions that can be experimentally verified.

In this paper, two statistical distribution functions of experimental material strength data from NBG-18, a normal distribution and a two-parameter Weibull distribution, are fitted. The distribution functions are then evaluated by visual inspection of the graphical representations of the data and by a GOF test, by means of an A-D test [84]. Thus, a comparison of the distribution in terms of their appropriateness in describing the data is made.

In addition, this paper presents and validates the novel approach of combining the normalised data sets to improve the basis for the estimates of the variability. This could imply that the variability on the graphite strength for the different strengths is based on the same flaw distribution and thus a property of the material.

The Weibull parameter m is the shape parameter (which determines the slope of the Weibull function) and S_c is the scale parameter or characteristic strength value (which determines the point at which the most data points are located). Note that the selection of a two-parameter Weibull distribution for the assessment of strength data is not based on this distribution being the most accurate; the following rationale supports the use of this distribution:

- This is an extreme value distribution. That means that the estimates are sensitive to the values at the lowest probabilities. This is important to characterise the strength in the tails of the distribution.

- The failure probability increases monotonically from a zero stress.
- Negative failure strengths are not predicted.
- It is possible to establish confidence intervals for the fit with reasonable amounts of data.

After the data have been fitted to each distribution function, the GOF test is used in order to evaluate the appropriateness of the chosen distribution. It should be noted that GOF statistics are not intuitively easy to understand or interpret. They do not provide a true measure of the probability that the data fit the distribution. Instead, they provide a probability that random data generated from the fitted distribution would have produced a GOF statistic value as low as that calculated for the observed data. If the sample passes the GOF test, the distribution can confidently be used to describe the data. If the data fail the GOF test, the assumed distribution is not necessarily invalid. GOF tests are very sensitive to changes in data and a small change of data can have a large influence on the GOF test.

The A-D test, according to Anderson and Darling [84], can be used to determine if a sample of data comes from a specific distribution. It is derived from the Kolmogorov-Smirnov (K-S) [83] test, according to Stephens [85], but gives more weight to the tail of the distributions. The A-D statistic is generally a more useful measure of fit than the K-S statistic, especially where it is important to place equal emphasis on fitting a distribution at the tails as well as the main body, Stephens [86]. This has the advantage of allowing a more sensitive test and the disadvantage that critical values must be calculated for each distribution. Note that for a given distribution, the A-D statistic may be multiplied by a constant which depends on the sample size. These constants are given in the various papers by Stephens [85-89]. Thus, for a certain sample size, a critical value can be calculated. The fit is compared to this critical value to determine if the fit passes or fails the A-D test. A MATLAB script to calculate the A-D GOF for the normal distribution and Weibull distribution of any sample size can be found in Trujillo-Ortiz *et al.* [90, 91].

6.3 Results

6.3.1 Tensile test

The graphical representation of TS data can be seen in Figure 6-1 and Figure 6-2 for the normal distribution and the Weibull distribution, respectively. Please note that the normal distribution probability plot has a logarithmic scale on the probability axis while the Weibull probability plot has a logarithmic scale on both axes. The normal distribution shows divergence on both tails of the distribution, while the Weibull distribution only shows divergence from the fit on the lower end of the distribution. The parameters obtained from the fit are given in Table 6-2. As per visual inspection of Figure 6-1 and, Figure 6-2 the Weibull distribution seems to be the more appropriate fit for the distribution.

6.3.2 Flexural test

The graphical representation of FS data can be seen in Figure 6-3 and Figure 6-4 for the normal distribution and the Weibull distribution, respectively. Similarly to the TS data, the normal distribution shows divergence on both tails of the distribution, while the Weibull distribution only shows slight divergence from the fit on the lower end of the fit. The parameters obtained from the fit are given in Table 6-2. From the visual inspection of Figure 6-3 and Figure 6-4, the Weibull seems to be the more appropriate fit for the FS data.

6.3.3 Compressive test

The graphical representation of CS data can be seen in Figure 6-5 and Figure 6-6 for the normal distribution and the Weibull distribution, respectively. The normal distribution shows a large divergence on both tails of the distribution while the Weibull distribution shows a large divergence from the fit on the low end of the distribution. The parameters obtained from the fit are given in Table 6-2. From a visual inspection of Figure 6-5 and Figure 6-6, it appears that neither the Weibull nor the normal distribution fit the data well. However, if comparison must be made, the Weibull distribution is the more appropriate choice as only the lower tail deviates from the distribution function. Generally, deviation of the lower tail of the distribution of the data indicates the existence of a bimodal distribution in the data. Visual identification of this bimodal Weibull distribution in accordance with the method described in Abernethy [64] is shown in Figure 6-7.

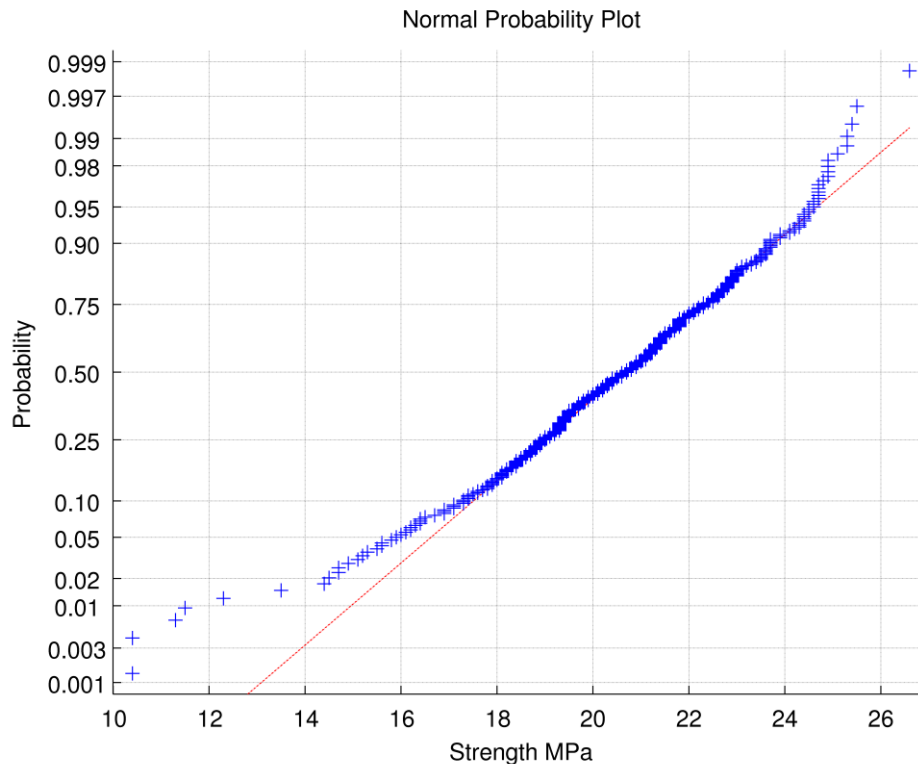


Figure 6-1: TS normal distribution fit

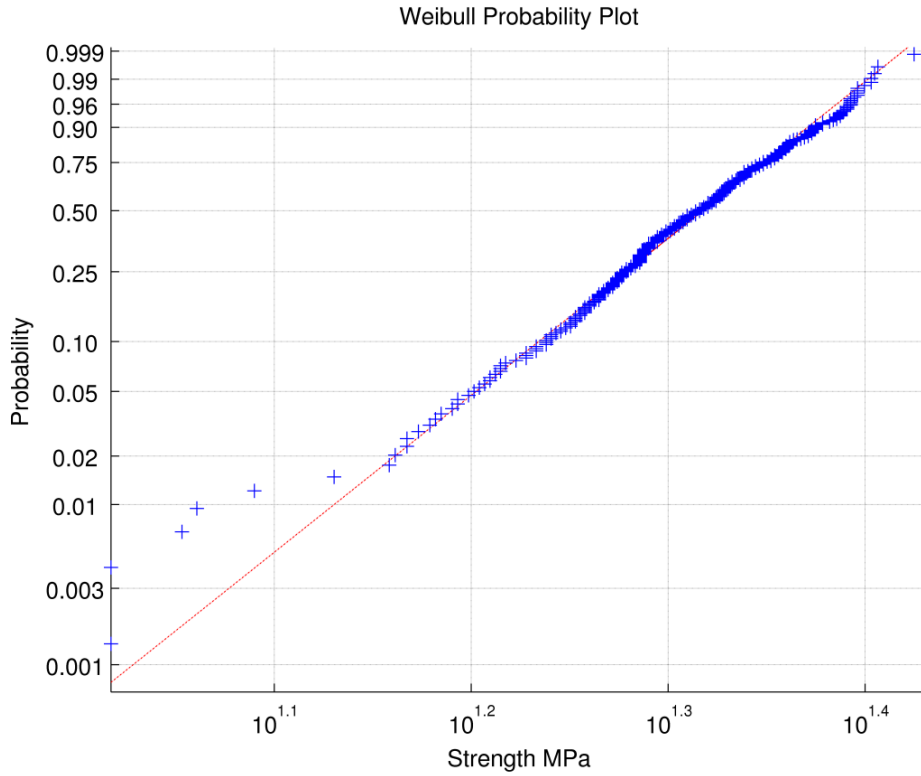


Figure 6-2: TS Weibull distribution fit

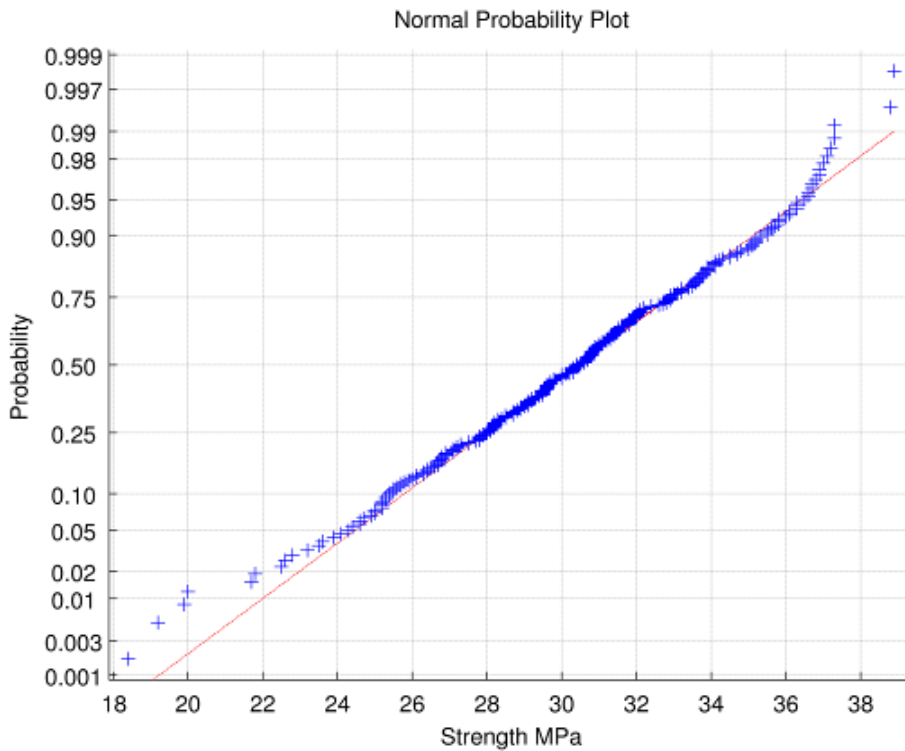


Figure 6-3: FS normal distribution fit

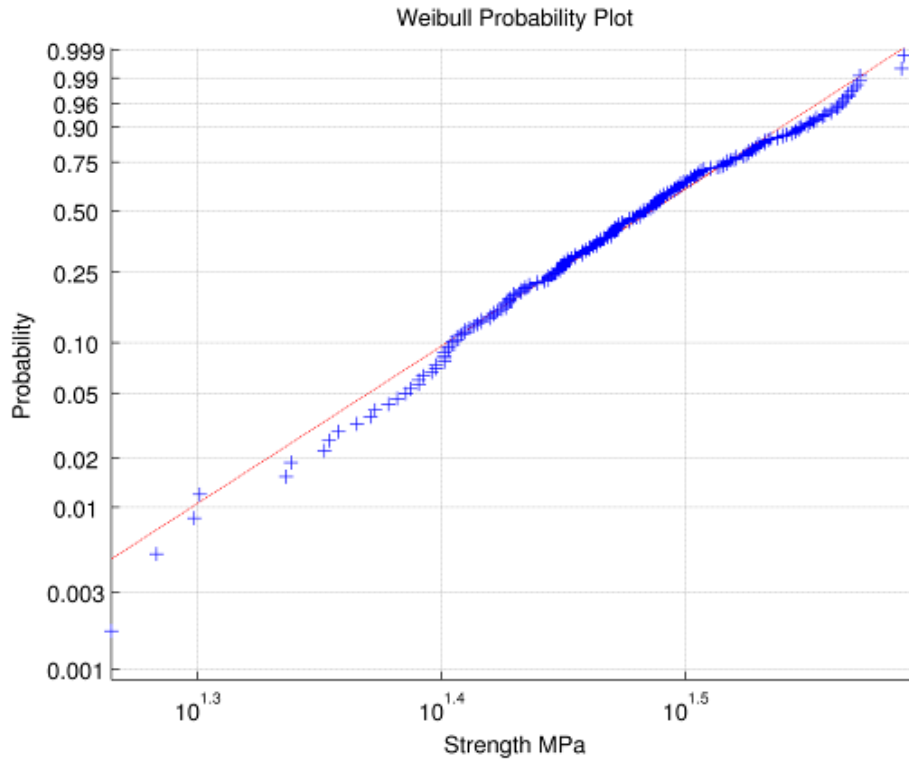


Figure 6-4: FS Weibull distribution fit

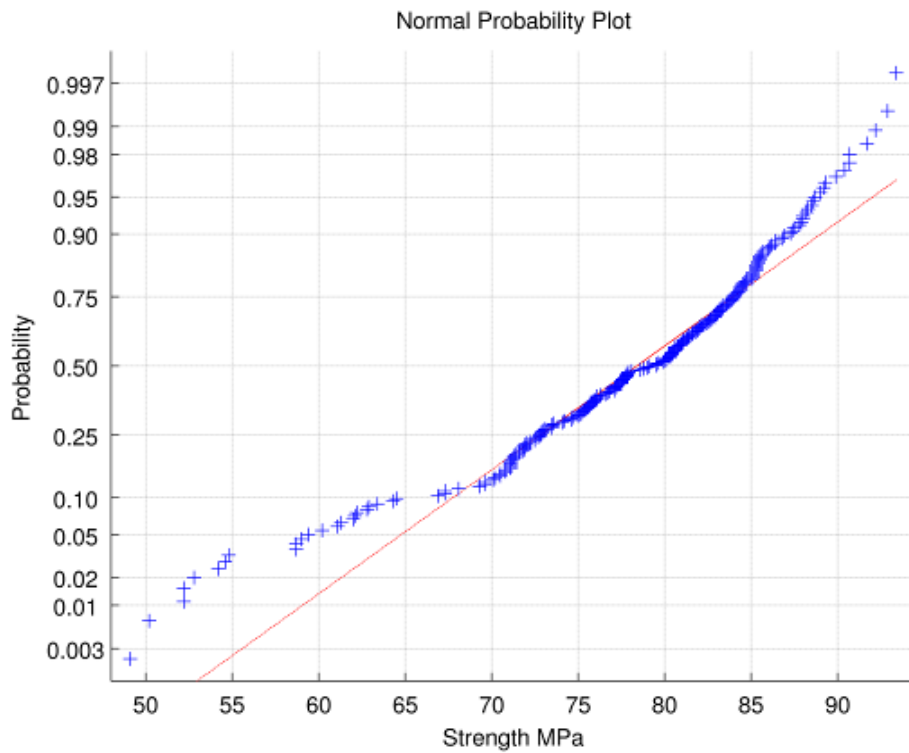


Figure 6-5: CS normal distribution fit

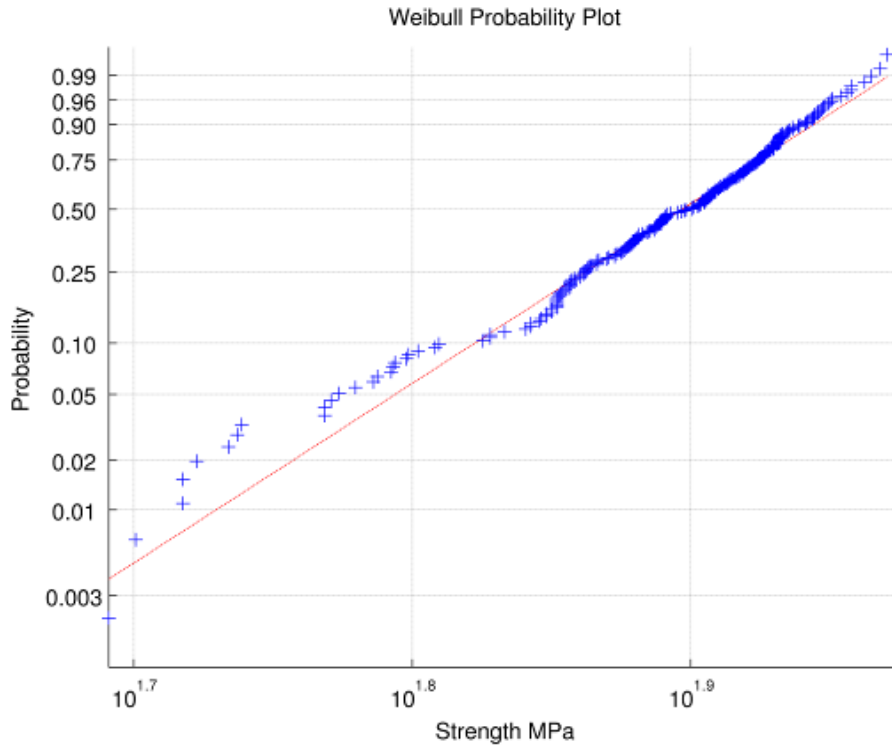


Figure 6-6: CS Weibull distribution fit

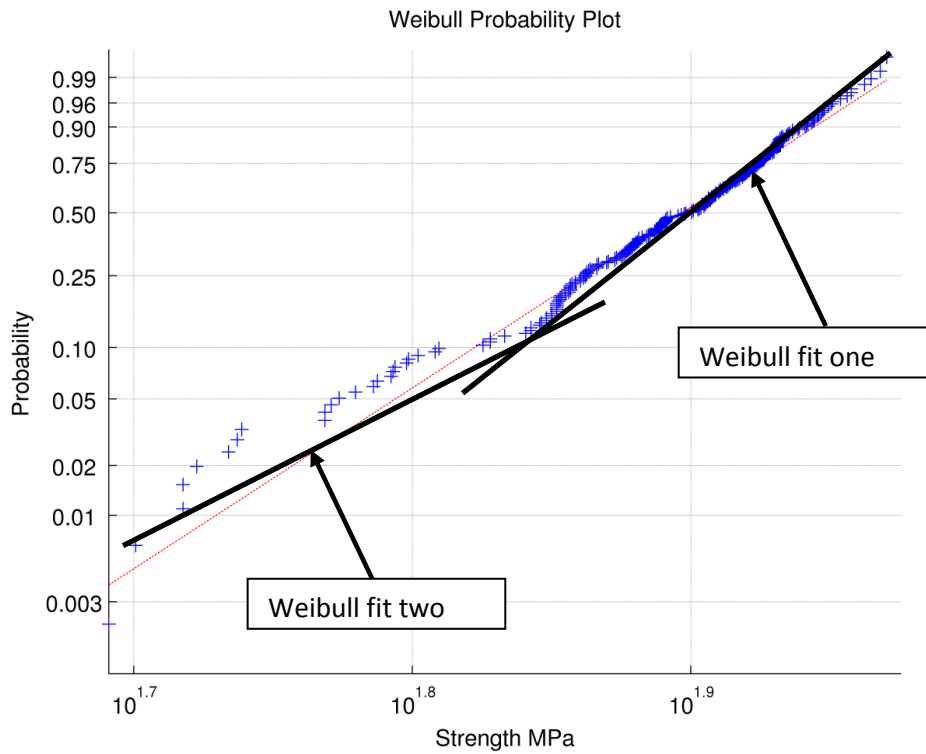


Figure 6-7: CS visual bimodal Weibull identification

6.4 Statistical data fitting

Using visual inspection to evaluate the graphical representations of data, it seems that the Weibull distribution may fit all three data sets reasonably well. The normal distribution deviates on the tails of the distribution for all data sets and would thus significantly underestimate the PoF for low probabilities (<2%). Note that Nemeth's [92] comments on the possible pitfalls of drawing conclusions from visual interpretation of data are valid. The values obtained from MATLAB for each of the fits can be found in Table 6-2.

Table 6-2: Statistical data fit parameters

Data Set	Normal Distribution			Weibull Distribution	
	Mean	Standard Deviation (SD)	SD / Mean	Scale Parameter	Shape Parameter
TS	20.49 MPa	2.64 MPa	12.9%	21.60 MPa	9.26
FS	30.31 MPa	3.74 MPa	12.3%	31.94 MPa	9.20
CS	77.62 MPa	8.73 MPa	11.2%	81.23 MPa	11.55

The A-D test parameters for each of the data sets are presented in Table 6-3. The GOF test is done testing against a significance α of 0.05. If the probability value is above 0.05, the test is passed and if it is below, the test is failed. Since the GOF test is very sensitive, a value close to passing the test should be carefully considered.

The TS data fits a Weibull distribution well, a normal distribution fits the FS data well and the CS data were not well fitted by either of the distributions. However, with a probability of 0.037, this data can possibly be from a Weibull distribution.

Table 6-3: A-D GOF values

Data Set	No. of Samples Used in Test	α	Normal				Weibull			
			A-D Stat	A-D Adjusted	Probability	Pass	A-D Stat	A-D Adjusted	Probability	Pass
TS	370	0.05	1.2945	1.2971	0.0023	N	0.6567	0.6635	0.086	Y
FS	292	0.05	0.3623	0.3633	0.4409	Y	1.0579	1.0703	0.0083	N
CS	228	0.05	3.679	3.6913	0	N	0.7994	0.81	0.0367	N

Kennedy and Eatherly [26] concluded that a bimodal distribution exists in the test data they analysed. They postulated the existence of a background mode which contains most of the data in a disparate mode in which only a small number of the specimens fail at a low load. Kennedy and Eatherly [26] findings indicates that this disparate mode exists in the lower end of the data. More recently, a disparate flaw mode in NBG-18 is reported by Burchell and Strizak [45].

To assess if such bimodal distribution exists in the data presented here, the bottom 2% of the data is removed from each of the data sets and the A-D GOF

test is performed on the remaining data. If a bimodal distribution exists in the original data set, the results obtained from the A-D GOF test will significantly differ once the tail is removed from the original data, while if it does not exist, the results will be very similar. However, since the Weibull distribution is more accurate in the tail than a normal distribution, if the data changes from a Weibull to a normal distribution, this condition does not necessarily confirm the existence of a bimodal distribution. It only suggests that the data should be checked for bimodality.

The results obtained from refitting the data with the tail removed are presented in Table 6-4. The TS data changes from a Weibull distribution to a normal distribution. Since this change can be expected, the existence of a bimodal distribution is not clear. The FS data clearly remains a normal distribution which implies that a bimodal distribution clearly does not exist in this data. The CS data set changes from not having clear distribution to a strong Weibull fit. This indicates the possible existence of a bimodal distribution, as indicated by Kennedy and Eatherly [26].

Table 6-4: GOF test with bottom 2% of data removed

<i>Data Set</i>	<i>No. of Samples Used in Test</i>	α	<i>Normal</i>				<i>Weibull</i>			
			<i>A-D Stat</i>	<i>A-D Adjusted</i>	<i>Probability</i>	<i>Pass</i>	<i>A-D Stat</i>	<i>A-D Adjusted</i>	<i>Probability</i>	<i>Pass</i>
TS	364	0.05	0.4618	0.4627	0.2572	Y	1.122	1.1338	0.0059	N
FS	287	0.05	0.3761	0.3771	0.4098	Y	1.6503	1.6698	0.0003	N
CS	224	0.05	2.5202	2.5288	0	N	0.4942	0.5008	0.2165	Y

According to the GOF test, the TS and CS data may have a bimodal distribution. To confirm this, the process is reversed and an A-D GOF test performed on the bottom part of each data set. To assess the GOF test, at least seven samples, according to Stephens [88], are needed. To fit a Weibull distribution, a general rule of thumb is to have at least 32 samples [64]. To ascertain whether the bottom samples have a clear distribution, the A-D GOF test is performed on sets, starting from 2% and then increasing the percentage. Initially, all the data sets pass all GOF tests as soon as they have seven or more samples. When the percentage reaches 10%, an interesting phenomenon occurs. The results for an A-D GOF test on the bottom 10% of each data set is shown in Table 6-5. The TS and FS change from passing an A-D GOF test on both distributions, to failing on both distributions. The CS data changes from both to a clear Weibull distribution. The process is repeated up until 20% of the sample and the results remain the same with the CS data having a clear Weibull distribution. This confirms the existence of a bimodal Weibull distribution in the CS data.

Table 6-5: GOF test for bottom 10% of data

<i>Data Set</i>	<i>No. of Samples Used in Test</i>	α	<i>Normal</i>				<i>Weibull</i>			
			<i>A-D Stat</i>	<i>A-D Adjusted</i>	<i>Probability</i>	<i>Pass</i>	<i>A-D Stat</i>	<i>A-D Adjusted</i>	<i>Probability</i>	<i>Pass</i>
TS	37	0.05	2.1760	2.2237	0	N	1.2022	1.2417	0.0032	N
FS	29	0.05	1.6969	1.7453	0.0002	N	1.2491	1.2955	0.0024	N
CS	23	0.05	0.8144	0.8444	0.0298	N	0.6597	0.6872	0.0749	Y

6.5 Normalisation of data

Each of the data sets is normalised to its own mean, as shown in Equation 6-3, to enable comparison between the sets.

$$\bar{x}_i = \frac{x_i}{\mu} \quad (6-3)$$

In Equation 6-3, \bar{x}_i is the new data point created, x_i is the existing data point, and μ is the mean of the original data set. Subsequently, the mean of the new data set will be one. Normalisation of each data set accommodates and accounts for the differences in the variance [64, 83]. Since each of the data points are multiplied by a factor $(1/\mu)$, the new variance σ_{new}^2 is calculated by multiplying the original variance σ_{org}^2 with $(1/\mu)^2$, as shown in Equation 6-4:

$$\sigma_{new}^2 = \left(\frac{1}{\mu}\right)^2 \sigma_{org}^2 \quad (6-4)$$

$$\sigma_{new} = \frac{\sigma_{org}}{\mu}$$

By combining the data sets, the fit can assess whether the data sets are from the same statistical population or not. The respective parameters obtained from fitting the normalised data for each data set to both the Weibull and normal distributions are shown in Table 6-6. The normalised data sets are also combined into one set, and both the Weibull and normal distributions are fit to this combined data set. For the normal distribution all the data are similar, except the CS test which actually has a smaller standard deviation than the other data sets. For the Weibull distribution, a similar trend with the CS data is identified, having a higher shape parameter than the other data.

Table 6-6: Normalised statistical fit

Data Set	Normal Distribution		Weibull Distribution	
	Mean	Standard Deviation	Scale Parameter	Shape Parameter
TS	1.0000	0.1286	1.0541	9.2670
FS	1.0000	0.1232	1.0536	9.2029
CS	1.0000	0.1124	1.0466	11.5464
Combined	1.0000	0.1228	1.0522	9.6388

Due to the automatic accommodation for variance as shown in Equation 6-4, the A-D GOF test results for the normalised data are exactly the same as the results obtained in Table 6-3. The A-D GOF test on the combined data set is shown in Table 6-7. The result indicates that the data fits a Weibull distribution with a significance α of 0.025. Table 6-7 implies that the data sets are very similar.

Table 6-7: GOF for combined data set

Data Set	No. of Samples Used in Test	α	Normal				Weibull			
			A-D Stat	A-D Adjusted	Probability	Pass	A-D Stat	A-D Adjusted	Probability	Pass
Combined	890	0.025	2.9149	2.9174	0	N	0.8455	0.8512	0.0289	Y

6.6 Summary

The three data sets investigated fail at different mean strengths, as shown in Table 6-2. From a graphical inspection, a Weibull distribution fits all the data reasonably well except for the CS data which appears to have a bimodal Weibull distribution.

The GOF test determines that a Weibull distribution is valid for the TS data, a normal distribution is valid for the FS data and a Weibull distribution is possible for the CS data.

By removing the bottom 2% of the CS data, the probability for a Weibull distribution increases substantially which indicates the existence of a second distribution in that data set. By performing an A-D GOF test on the bottom 10% of the data, the existence of a bimodal distribution in the CS data is confirmed.

When scaling the data sets, the TS and FS data have very similar fits. The CS data set has a lower variance than the other data even though the data have indications of a possible bimodal distribution.

The combined data set passes the GOF test for a Weibull distribution, which indicates that the mechanisms of failure between the three data sets are similar. The success at fitting the Weibull distribution through the combined normalised

data sets allows the improvement of the basis for the estimates of the variability. This could imply that the variability on the graphite strength for the different strengths is based on the same flaw distribution and thus, a property of the material. This observation is attributed to the use of a large and representative data set.

7. A NUMERICAL STRESS BASED APPROACH FOR PREDICTING FAILURE IN NBG-18 NUCLEAR GRAPHITE COMPONENTS WITH VERIFICATION PROBLEMS [78]

Michael P Hindley*, Mark N Mitchell*, Christiaan Erasmus*, Ross McMurtry**, Thorsten H Becker***, Deborah C Blaine*** and Albert A Groenwold***

*Formerly Pebble Bed Modular Reactor (Pty) Ltd., P.O. Box 9396, Centurion, South Africa 0046

**Frazer-Nash Consultancy, 1 Trinity Street, College Green, Bristol, BS1 5TE, UK

***Department of Mechanical and Mechatronics Engineering, Stellenbosch University, Private Bag X1, Matieland 7602

Keywords

Nuclear graphite, failure prediction, NBG-18

Abstract

This paper presents a methodology that can be used for calculating the probability of failure of graphite core components in a nuclear core design, such as that of the Pebble Bed Modular Reactor. The proposed methodology is shown to calculate the failure of multiple geometries using the parameters obtained from tensile specimen test data. Experimental testing of various geometries is undertaken to verify the results. The analysis of the experimental results and a discussion on the accuracy of the failure prediction methodology are presented. The analysis is done at 50% probability of failure as well as lower probabilities of failure.

7.1 Introduction

This paper describes the method used for calculating the probability of failure (PoF) of graphite components in the core of high-temperature gas reactors (HTGR), such as the Pebble Bed Modular Reactor (PBMR).

Nuclear graphite has inherent defects, such as crystal irregularities, pores, inclusions and cracks. These defects can reduce the material strength and act as stress-concentrating features, and can thus initiate fracture under a low load [15, 42]. The variability of defect size, orientation and their random distribution through the material have been shown to lead to a large scatter in experimental material strength test measurements [41, 77]. In addition, it has been shown that damage also accumulates in the material as it is loaded until a “critical” damage

level is reached [41]. Due to this material variability, it is difficult, if not impossible, to define an accurate load resulting in the failure of the component [93].

The observed experimental behaviour of graphite exhibits the following interesting phenomena:

- For specimens of a similar size, failure stresses are higher in compression compared to tension [77].
- For specimens of a similar size, failure stresses are higher in bending compared to tension [77].
- The experimental results have indicated that the strength of graphite is independent of the volume for practical sample sizes [22, 30, 77].

Graphite behaviour ranges from brittle to quasi-brittle, depending on the processing of the material [15]. It is more likely that low void content, fine-grained materials are more brittle than high void content, larger-grained materials [15]. Regardless of the processing, the strength of graphite is always stochastic, nominally identical specimens will display significant deviation in strength from the population mean [15]. The acceptability of fluctuation for NBG-18 has been defined by Mitchell [94]; these limits will be utilised in this paper. The strength of most grades of graphite tends to be transversely isotropic.

One approach for assessing failure is the use of fracture mechanics. This approach has been studied by Burchell [44], Ho *et al.* [23], Kennedy and Kehne [46], Wang and Liu [49], Sakai *et al.* [52] and Becker *et al.* [42]. Although some success in this area has been achieved, the methods are complex to implement in irradiated analysis and thus their applicability to design is limited. Furthermore, using the Double Torsion geometry [51] and an algorithm to calculate the fracture parameters from digital image correlation [43] Becker *et al.* [42] have shown that fracture mechanics failure parameters can be size dependent.

The variability of material strength suggests that using a probabilistic design approach is well suited for nuclear graphite. A statistical approach can be used to assess the acceptably low risk of part failure. By defining the material strength using an appropriate probability density function, the component can be designed to meet the required specifications. The Weibull theory, in which the strength of a brittle solid is assumed to be controlled by flaws, has potential uses in the engineering design of load-bearing structures made from brittle materials, because it relates the PoF to the volume of material under load, the stress gradient and multi-axial stress states [28]. Weibull's weakest link theory anticipates that the larger the volume of material, the greater the chance that a defect exists within the volume [71]. Subsequently, Weibull predicts that the PoF increases with increasing volume for the same stress. It follows that the probability of finding unfavourable defects increases with the increase in volume. The probability that such defects can propagate to failure increases with increasing stresses [36] (more commonly known as the volume effect in brittle materials). However, this is inconsistent with the experimental results of nuclear graphite [23, 30] since this volume effect does not show the expected effect in tensile specimens, but does exist to an extent in bending and other specimens

[77]. The Weibull theory also predicts that specimens in bending will fail at a higher stress than specimens under tension [15]. This is consistent with the experimental results [77]. Thus, it proves difficult to predict the failure of a graphite component from small specimen tests using a standard Weibull approach [81].

The application of Weibull's theory on nuclear graphite has been studied by Brocklehurst and Darby [22], Mitchell *et al.* [35], Kennedy and Eatherly [26] and Price [28]; however, all have concluded that the Weibull model is inconsistent with the material behaviour of nuclear graphite. Strizak [30] investigated the effect size and volume of nuclear graphite and has also concluded trends inconsistent with the Weibull theory for small test specimens. Ho [24] finds that the strength of a specimen decreases as the gauge diameter of the specimen approaches a grain size. Modification of the Weibull theory for the material is proposed by Schmidt [37] and Ho [24] to account for this behaviour.

Although the material behaviour of graphite is poorly represented by the standard Weibull approach, the Weibull method does offer characteristics which are well suited to graphite failure prediction. The basis of the work presented here is based on the Weibull modification done by Schmidt [36, 37, 48, 56]. This paper presents a numerical modification to Schmidt's volume normalisation in Schmidt [37] as well as the three-parameter Weibull weakest link theory to account for graphite material behaviour. The methodology is implemented in conjunction with linear elastic finite element analysis (FEA).

7.2 Material reliability

The mechanical design of the graphite moderator and reflector blocks of an HTGR requires a detailed knowledge of the statistical strength distribution in the graphite component [28].

Kennedy and Eatherly [26] concluded that a bimodal distribution exists in the failure data analysed. They postulated the existence of a background mode, which contains most of the data, and a disparate mode with only a relatively small number of specimen failures. Kennedy and Eatherly [26] finding indicates that this disparate mode exists in the lower band of the failures. More recently, a disparate flaw mode in NBG-18 was also reported by Burchell and Strizak [45]. Hindley *et al.* [77] found a bimodal distribution for NBG-18 in the compressive strength (CS) failure data but not for the tensile strength (TS) or flexural strength (FS) data.

In the methodology presented here, a three-parameter Weibull fit is utilised. The parameters have been obtained from tensile test cases (or a combined tensile equivalent). From Hindley *et al.* [77], it is important to understand that the Weibull fit on the tensile test case or the Weibull fit combined data set yield the same parameters. The basic three-parameter Weibull distribution as a function of the applied stress σ is shown in Equation 7-1. The parameters are the characteristic strength S_c , the shape parameter m and the threshold value S_0 .

$$f(\sigma) = e^{-\left(\frac{\sigma - S_0}{S_c - S_0}\right)^m}, \sigma > S_0 \quad (7-1)$$

The Weibull fit values used are shown in Table 7-1. In addition to these parameters, it is also necessary to determine the ratio of TS to CS, which is also shown in Table 7-1.

Table 7-1: Material parameters used for the failure calculations

S_c [MPa]	Shape Parameter m	Tensile/Compressive Strength Ratio R	S_0 [MPa]
21.6	5.78	0.264	8.25

7.3 Failure calculation method

This section explains the steps required to calculate the PoF. A summary of the calculation method is provided in Hindley *et al.* [78]. The requirement of the failure assessment methodology presented is to predict the PoF of a graphite component under a given stress state. The methodology employed is a modified volume normalised Weibull weakest link failure criterion. This is based on the volume normalised method described by Schmidt [37]. This paper presents the methodology and accuracy of results. The implementation of this method presented is currently also incorporated into the American Society of Mechanical Engineers' (ASME's) codes and standards [76].

The three-parameter Weibull weakest link method (extension of Equation 7-1) for the calculation of the PoF with the volume normalisation as proposed by Schmidt [37] is shown in Equation 7-2. The key difference between the Weibull formulation to follow and Schmidt's [37] approach is that in the formulation to follow, Equation 7-2 is used on a single link in a weakest link calculation instead of the full component as was previously done. The total PoF is then the product of the PoF of each link in this weakest link formulation in Equation 7-2.

$$PoF = 1 - e^{-\sum_{i=1}^{n_i} \left(\frac{\sigma - S_0}{S_c - S_0}\right)^m \frac{v_i}{v_l}} \quad (7-2)$$

Where

v_i = volume associated with a link

v_l = total volume of the component (volume normalisation proposed by Schmidt [37])

n_i, n_{ii} = link number in the weakest link calculation

S_c = characteristic strength

m = shape parameter

$S_{0.}$ = threshold value

7.3.1 Assessment method

The failure assessment methodology essentially consists of the following processes:

- The three-parameter Weibull probability distribution is fitted to experimental TS measurement data. The Weibull fit values are given in Table 7-1. (For more details on the fits, refer to Hindley *et al.* [77].)
- The stress state in the component is determined. Generally, this will involve a three-dimensional (3D) FEA of the component in order to calculate the principal stresses and the corresponding volumes. The experimentally determined average failure load is applied to the FEA model.
- A numerical weakest link theory is applied to evaluate the PoF of the part based upon the equivalent stress and volume in each element.

7.3.2 Stress calculation

The formulation of the stress-based failure criterion is founded on the hypothesis that the elastic energy per unit volume, stored in a given material element at the moment of fracture, is equal to the elastic energy that is stored per unit volume in the uni-axially loaded test specimen at fracture [56]. The CS of NBG-18 graphite is almost four times higher than the TS [77]. To enable direct comparison of tensile and compressive stress components, all compressive principal stress components are converted to their equivalent tensile stress (in terms of likelihood to cause failure) by multiplying by a weighting factor (R) equal to the ratio of mean tensile to mean compressive strength.

To quantify the elastic strain energy, the stress intensity (σ_v) is introduced as defined by Schmidt [37], and calculated using Equation 7-3 assuming a linear elastic material behaviour. This equivalent stress intensity is also referred to as the maximum deformation energy (MDE) stress [37, 57].

$$\sigma_v = \sqrt{\bar{\sigma}_1^2 + \bar{\sigma}_2^2 + \bar{\sigma}_3^2 - 2 \cdot \nu \cdot (\bar{\sigma}_1 \cdot \bar{\sigma}_2 + \bar{\sigma}_1 \cdot \bar{\sigma}_3 + \bar{\sigma}_2 \cdot \bar{\sigma}_3)} \quad (7-3)$$

where

$\sigma_1, \sigma_2, \sigma_3$ = the three components of principal stress

$\sigma_i = f \cdot \sigma_i$ where i is the direction of the principal stress ^{1,2,3}

$f = 1$ if σ_i is a tensile stress

$f = R$ if σ_i is a compressive stress (where R is the ratio of mean tensile to mean compressive strength)

ν is Poisson's ratio

7.3.3 Volume definitions

The methodology is based on the hypothesis that once the material reaches a certain volume or size, the dissipation of energy between the microstructural elements is sufficient to show homogeneous mechanical rheological response in the material on a macroscopic scale. The macroscopic rheological response is measured during mechanical testing of components (tensile test, bending test etc.). The approximation of this response is achieved by a volume grouping method which defines the size of a link in the weakest link calculation. The heuristic rationale behind this is that a "link volume" is required for the material to exhibit a macroscopic rheological response. The "link volume" is proposed to be of the order of 10 times the maximum grain size (Mgs). This is proposed by Denninghoff and reported by Schmidt [29]. Ho [24] found that the grain size effect comes into existence when a tensile test specimen gauge diameter is reduced below 10 to 15 times the Mgs. Ho [24] found that the materials become far weaker when the gauge diameter is reduced to this extent.

In the finite element (FE) model, each element contains a number of Gauss integration points, the precise number depending upon the order and type of the element used. Each Gauss point has an associated material volume which will, from here on, be referred to as a "sub-element". For the analysis performed in this paper, MSC Marc was used. The three principal stresses and the associated volume for each stress were obtained using a user subroutine in accordance with the subroutine manual [95]. The finite element analysis of a graphite core part will produce a table of principal stresses and volume values for each sub-element in the FE model. From the principal stresses, the equivalent stress-intensity is then calculated for each sub-element.

7.3.4 Algorithm for calculation of probability of failure

7.3.4.1 Application of the weakest link theory

First, the array of principal stresses and sub-element volumes are obtained from the FEA. The principal stresses are used to calculate the stress intensity for each sub-element, which is sorted in descending order of stress-intensity magnitude. This is done so that the sub-elements with a similar stress intensity can be grouped into a "link volume". The rationale for the formulation is that a link in the weakest link calculation should have a minimum volume to represent the macroscopic rheological response of the material. Ideally, the links should be sorted by location; however, sorting the equivalent stress intensities in order of magnitude allows for a simpler computation of the PoF. This simplification is motivated by the fact that during irradiated analysis, usually only one point of high

stress occurs. If more than one location of high stress exists, the locations would be sorted in the same group resulting in a conservative failure prediction.

7.3.4.2 Sliding threshold

The three-parameter Weibull distribution is founded on the basis that any load applied below the threshold value S_0 does not influence the failure. Although this is true when a significant volume of material is stressed above the threshold value, it is not valid when a significant volume of material is stressed below the threshold value. The volume of material used for failure calculation will hereafter be referred to as the PoF calculation volume. Subsequently, the sliding threshold is applied to:

- ensure a sufficient PoF calculation volume of material is always used to make multiple links in the weakest link calculation even at very low loads; and
- allow for the likelihood of failure at very low loads that are not sufficiently captured by the standard three-parameter Weibull distribution fit (possibly as a result of bimodal strength distributions as seen in Hindley *et al.* [77], Kennedy and Eatherly [26], and Burchell and Strizak [45]).

The following conditions are applied to the threshold value:

- If the maximum stress intensity $\sigma_{v,max}$ is greater or equal to S_c , then S_0 remains unchanged, as shown in Equation 7-4.

$$S_0' = S_0 \quad (7-4)$$

- If the maximum stress intensity $\sigma_{v,max}$ is less than the value of S_c , then S_0 is recalculated, as shown in Equation 7-5.

$$S_0' = \frac{\sigma_{v,max}}{S_c} S_0 \quad (7-5)$$

7.3.4.3 Sub-element calculation

An arbitrary value of X_i is calculated as follows for each sub-element, as shown in Equation 7-6.

$$X_i = \left\{ \begin{array}{ll} \left[\frac{\sigma_i - S_0'}{S_c - S_0'} \right]^m & \sigma_i > S_0' \\ 0 & \sigma_i < S_0' \end{array} \right\} \quad (7-6)$$

where

i = the number of the sub-elements in the whole part

Equation 7-6 is now a numerically varied version of the exponential part of Equation 7-2.

7.3.4.4 Grouping

The grouping criteria of the link volume are summarised as follows:

- Any link volume should have a total volume greater than $(10 \cdot \text{Mgs})^3$ as discussed by Hindley *et al.* [78]. If this criterion is not satisfied, the group is expanded by one sub-element and the criterion is re-checked. This process is repeated as necessary until the first criterion is satisfied.
- Once the first criterion is satisfied, the difference between the maximum X_i and minimum X_i of all sub-elements in a group is compared. If the difference is larger than 7% (discussed by Hindley *et al.* [78]), the current group is considered complete and the next group is begun. Otherwise the group is expanded until this limit is exceeded. Denninghoff proposed a value reported by Schmidt [29] based on the maximum stress in the whole component, but this has been found to cause discontinuities at low PoF due to the number of links used in the failure calculation changing suddenly.

The total number of groups created is problem-dependent. If all the sub-elements have been assigned to a link volume, the probability calculation can proceed.

7.3.4.5 Weakest link calculation

The probability of survival (PoS) of each group is then calculated in accordance with Equation 7-7:

$$L_I = e^{-\left[\sum_{i=1}^{n_I} X_i \cdot \frac{V_i}{V_I} \right]}, L_{II} = e^{-\left[\sum_{i=1}^{n_{II}} X_i \cdot \frac{V_i}{V_{II}} \right]}, \dots \quad (7-7)$$

where:

subscripts I , II , etc. denote group one, group two, etc.

L_I , L_{II} , etc. = PoS of group one, group two, etc.

V_i = volume associated with one sub-element

V_I , V_{II} , etc. = total volume of group one, group two, etc.

X_i = as defined in Equation 7-6

n_I , n_{II} , etc. = sub-element number at the end of group one, group two, etc. when sorted in order of decreasing stress intensity

The PoS of the part as a whole, L_{part} , is hence calculated using the chain rule Equation 7-8.

$$L_{part} = L_I \cdot L_{II} \cdot L_{III} \cdot \dots \quad (7-8)$$

The PoF is then calculated by $1-L_{part}$.

7.4 Verification

A total of 26 geometry configurations are used to test the failure methodology. These cover a range of geometries, load applications and stress states, as shown in Table 7-2.

7.4.1 Geometry

The tests are divided into seven unique groups, differing in geometry and load type. Table 7-2 describes the seven test set groups, each labelled with a “VP” number, for verification problems (VPs). A different number of tests were performed on each VP, also shown in Table 7-2, and a total of 1 087 tests were performed altogether.

7.4.2 Mesh convergence

The accuracy of the failure predictions depend upon the validity of the FE results. The FE results are dependent on the refinement of the mesh used. Thus a sensitivity of failure probability on FE mesh convergence is also undertaken. These results are presented in Figure 7-2.

7.4.3 Acceptance criteria

The failure methodology should predict the 50% PoF when the average experimental failure load is applied to the FE model. In reality, a certain degree of error is expected between test data and the analysis. There are several sources of the difference between theoretical and experimental results. These include experimental error, error in the failure prediction methodology and variability in the material.

To formulate an acceptance criterion for determining the accuracy of the methodology, the systematic billet-to-billet variation in material strength is considered. Typically, the test specimens for each test case are extracted from a single billet. However, failure predictions are based on the full set of specimen test cases for all of the material. This implies that predictions that fall within the range of the experimental averages defined by the billet-to-billet variation are accurate.

The experimental tensile test data [77] of a set of 24 NBG-18 billet experiments [94] have shown the following:

- The TS of 50% of billets falls within $\pm 6\%$ of the material strength average.
- The TS of 95% of billets falls within $\pm 18\%$ of the material strength average.

Therefore, analyses that calculated failure load within 6% of the experimental data are considered accurate. Analyses calculated between 6% and 18% are acceptable. Deviations of more than 18% suggest deviation that is not properly captured by the model. These two limits are shown on Figure 7-2 as horizontal bands.

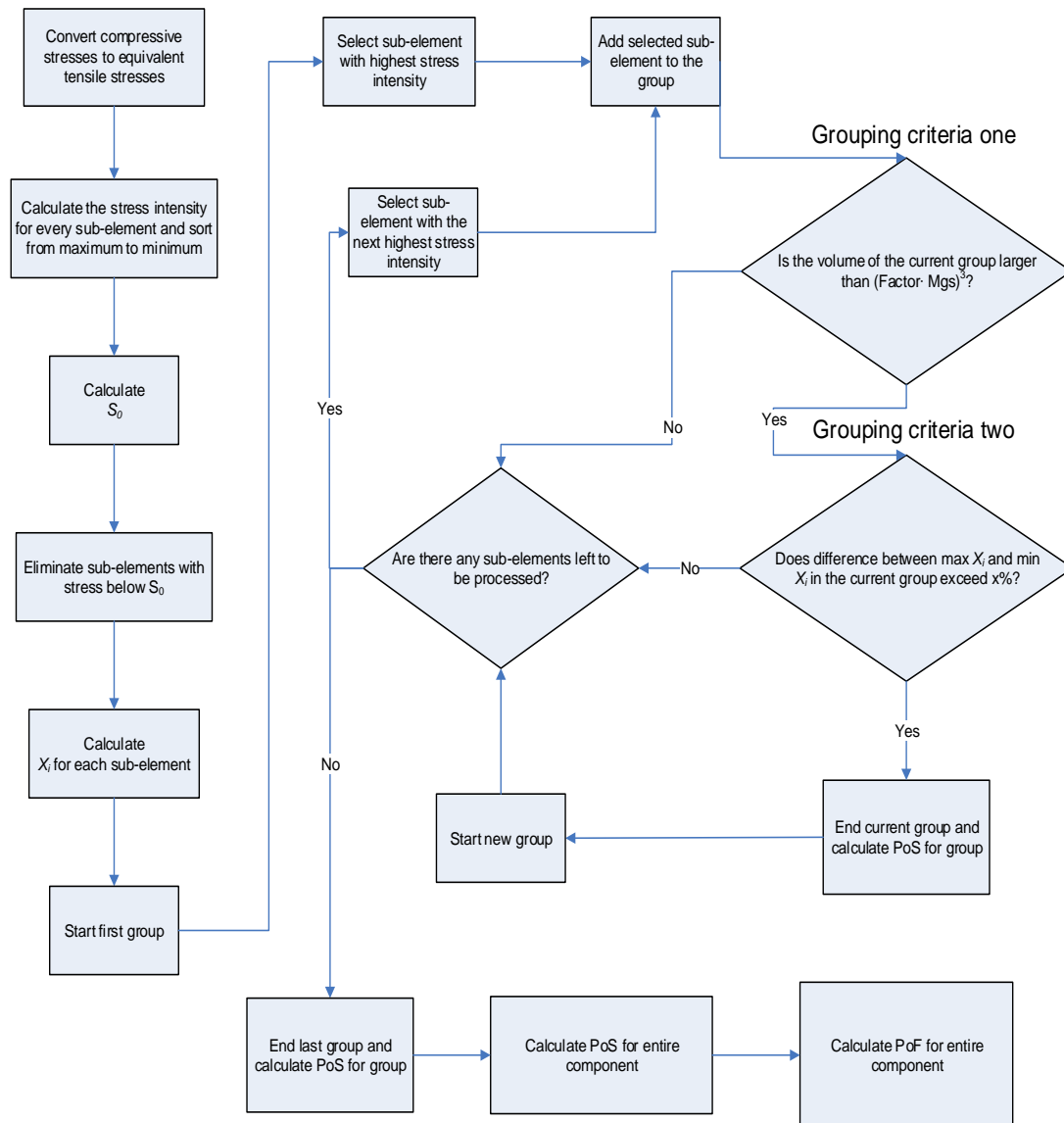
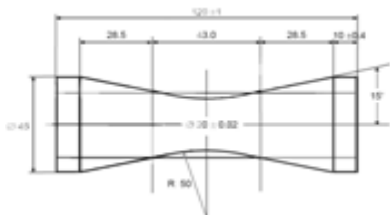
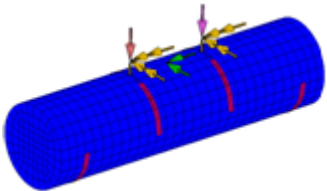
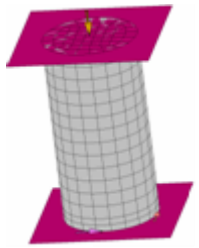
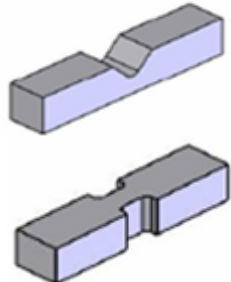
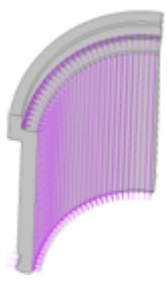

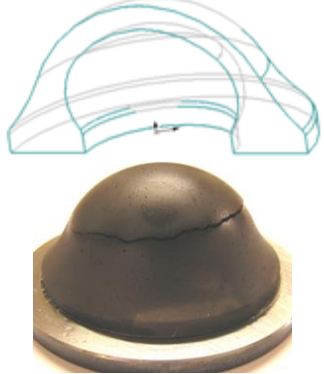


Figure 7-1: Flow chart of algorithm

Table 7-2: Breakdown of the experimental VP

Geometry	Description	Variations	Data Points	Geometry Illustration
VP-00	Tensile test specimens [96]	1	370 [97]	
VP-01	Cylinders undergoing four-point bend tests [93]	2	260 [97]	
VP-19	CS tests [98]	2	262 [97]	
VP-12	Beams with stress-concentrating geometric features undergoing four-point bend tests [99]	16	160 [100]	
VP-15	Sleeve burst tests [101]	1	6 [102]	
VP-17	Specimens from Roberts [20] undergoing tensile & compressive strength tests	2	Only mean reported in Roberts [20]	

Geometry	Description	Variations	Data Points	Geometry Illustration
VP-18	Multi-axial fatigue test specimens from Roberts [20] undergoing static tensile & compressive strength tests	2	Only mean reported in Roberts [20]	

7.5 Results

From Hindley *et al.* [77], it is seen that the highest population density (highest number of failures) is at the average experimental failure load. This load corresponds to a 50% PoF load predicted by the model. For this reason, the 50% PoF load is a good basis for comparison. Figure 7-2 shows the predicted 50% PoF load for each analysis compared to the measured 50% PoF load for each test case.

In order to calculate the predicted failure load, an iterative process is followed. Since the FEA uses a linear elastic material model, the principal stresses are directly proportional to the load applied. The FEA model is modelled with the 50% PoF load from experimental results for each test case. The results from the FEA are used to calculate the PoF. The difference between the calculated PoF and the required 50% PoF is used to scale the principal stresses and the PoF is recalculated until the predicted PoF reaches a 50% PoF.

To understand the results in Figure 7-2, the principle of a relative plot is introduced. In this relative plot, each test case is normalised to its own 50% PoF experimental failure load. This allows for comparison between test cases with different failure loads. For the 50% PoF model predictions, a value of 1.0 would indicate exact agreement between prediction and experiment. Data points lying below 1.0 indicate that failure is predicted to occur at a lower load than experimentally observed and these are therefore considered conservative predictions. Similarly, data points lying above 1.0 are not conservative.

Vertical grid lines, text and graphical labels are provided in Figure 7-2 to distinguish between the different tests and analyses. Solid vertical lines separate the different VPs, dash-dot lines separate the different model types and dot-dot lines separate the models with different fillet radii for the VP-12 beams with notches.

7.5.1 Mesh refinement

In Figure 7-2, data points not separated by a vertical grid line represent the same model for various mesh refinement solutions. This serves to show the failure criteria convergence of the FE mesh. The degree of mesh refinement increases from left to right. Only the last mesh represents a fully-converged mesh. In most cases, failure criteria convergence is reached before mesh convergence.

7.5.2 Observations at a failure load of 50% probability of failure

In Figure 7-2, the most accurate 50% PoF load predictions are made for specimens experiencing a uni-axial, or approximately uni-axial, stress state (VP-00, VP-01, VP-17 and VP-19). The least accurate predictions are made for the multi-axial specimens (VP-18) and notched beams with a 1 mm fillet radii (VP-12). All analytical failure load predictions fell on the conservative side of the experimental average failure loads. Six out of the 26 analyses did not comply with the acceptable material variation.

Table 7-3 summarises the 26 converged FE meshes used in analysis on the 26 test cases. In Table 7-3 the specimen volume for each test case as well as the PoF calculation volume of each test case are shown. This PoF calculation volume is determined by the three-parameter Weibull distribution obtained from Table 7-1 and the modification to the threshold value S_0 suggested by Equation 7-5. The range of test sample volumes covers three orders of magnitude, from 8×10^{-6} to $6.14 \times 10^{-3} \text{ m}^3$. This is sufficient to indicate any volume effect errors from the failure methodology. Since the loading conditions are different for each problem, the stress fields are different for each problem. Subsequently, the PoF calculation volume is different for each test case even if the geometric problem is exactly the same. The ratio of the PoF calculation volume to the actual problem volume used for failure calculation ranges from 0.03% to 100% across the 26 test cases presented in Table 7-3. In addition, the experimental 50% PoF load and the predicted 50% PoF load are also given in Table 7-3.

7.5.3 Full range failure probability predictions

The previous section compared the predicted 50% PoF load to experimental data. The 50% PoF likelihood of failure (as opposed to lower probabilities of failure) is convenient to use in an assessment of the accuracy of the failure prediction methodology as fewer experimental data points are required. However, when designing structural parts for nuclear engineering applications, the allowable failure probability to be considered would be 10^{-2} and lower [76]. A useful failure methodology must therefore provide acceptable failure estimations for the full range of failure probabilities relevant to the particular part. In addition, an acceptable failure methodology would show no discontinuities in PoF as the load on the component is changed.

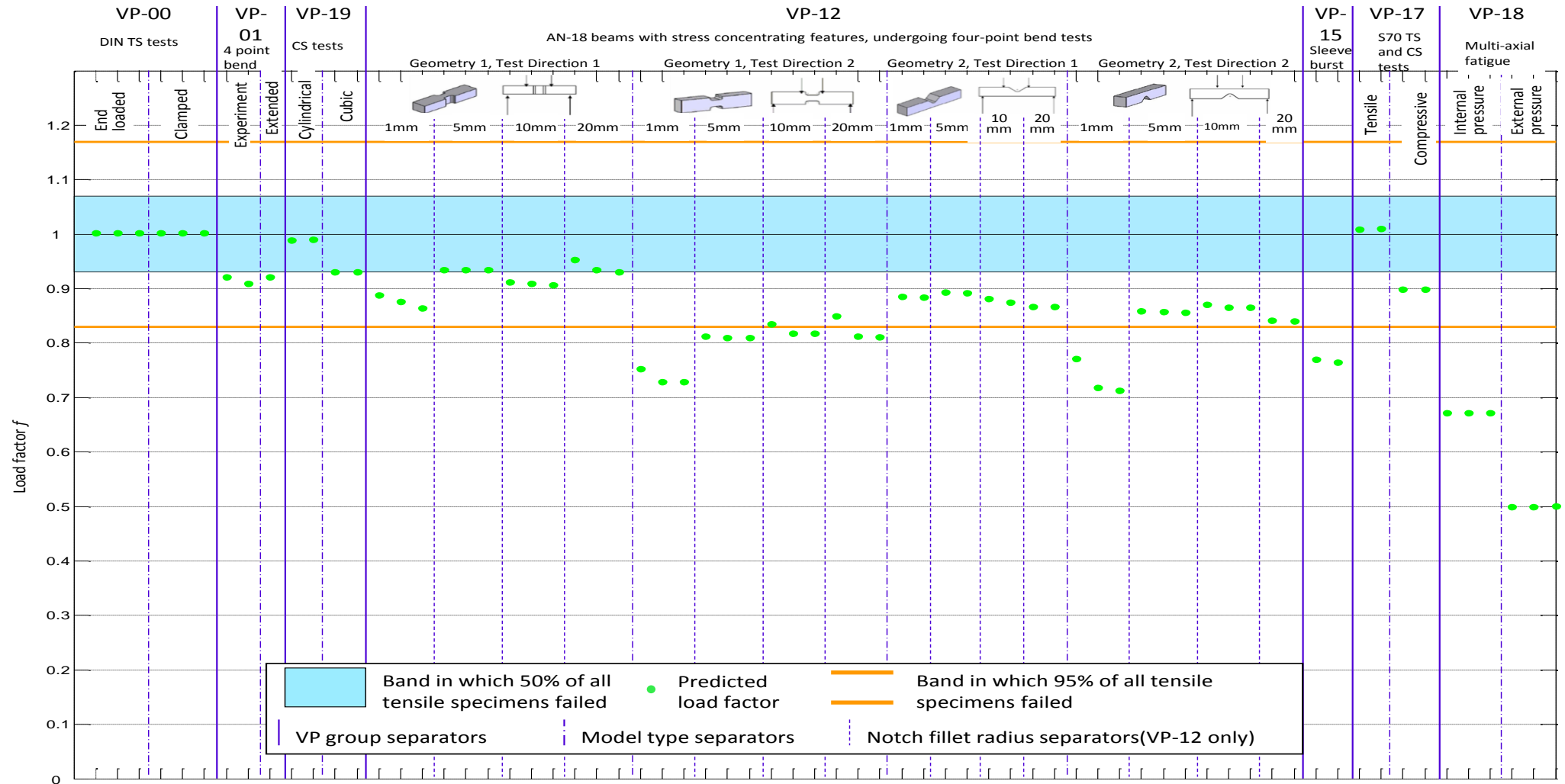


Figure 7-2: Prediction for 50% PoF

This section compares the numerically estimated failure loads across the full range of failure probability. Only three data sets with sufficient readings for low probability comparison exist, namely VP-00, VP-01 and VP-02. A detailed statistical evaluation of these three data sets can be found in Hindley *et al.* [77].

Table 7-3: Test case geometry descriptions

<i>VP ID</i>	<i>Problem Description</i>	<i>Problem Volume [m³]</i>	<i>PoF Calculation Volume [m³]</i>	<i>Ratio of PoF Calculation Volume /Problem Volume [%]</i>	<i>Experimental 50% PoF Load [kN]</i>	<i>Model Prediction 50% PoF Load [kN]</i>
VP-00.02	Tensile sample, ends loaded	9.09E-04	2.56E-04	28.2	6.50	6.52
VP-00.05	Tensile sample, clamped	9.09E-04	3.70E-04	40.8	6.50	6.52
VP-01.02	Four-point bend	1.56E-04	1.54E-05	1.0	2.69	2.44
VP-19.01	Compressive cylinder	1.26E-05	1.26E-05	100	24.91	24.66
VP-19.03	Compressive cube	8.00E-06	8.00E-06	100	33.74	31.39
VP-12.02	Geometry 1 ¹ Test direction 1 ² 1 mm radius	6.14E-03	2.82E-04	0.46	9.66	8.58
VP-12.05	Geometry 1 ¹ Test direction 1 ² 5 mm radius	6.14E-03	3.43E-04	0.56	10.25	9.58
VP-12.08	Geometry 1 ¹ Test direction 1 ² 10 mm radius	6.14E-03	3.64E-04	0.59	10.99	9.97
VP-12.11	Geometry 1 ¹ Test direction 2 ³ 20 mm radius	6.14E-03	4.17E-04	0.67	11.26	10.49
VP-12.14	Geometry 1 ¹ Test direction 2 ³ 1 mm radius	6.14E-03	1.63E-04	0.27	7.10	5.17
VP-12.17	Geometry 1 ¹ Test direction 2 ³ 5 mm radius	6.14E-03	1.94E-04	0.32	7.65	6.20

VP ID	Problem Description	Problem Volume [m³]	PoF Calculation Volume [m³]	Ratio of PoF Calculation Volume /Problem Volume [%]	Experimental 50% PoF Load [kN]	Model Prediction 50% PoF Load [kN]
VP-12.20	Geometry 1 ¹ Test direction 2 ³ 10 mm radius	6.14E-03	1.93E-04	0.31	8.01	6.55
VP-12.23	Geometry 1 ¹ Test direction 2 ³ 20 mm radius	6.14E-03	1.69E-04	0.27	8.57	6.95
VP-12.26	Geometry 2 ⁴ Test direction 1 ⁵ 1 mm radius	2.00E-03	1.12E-04	0.55	4.43	3.91
VP-12.29	Geometry 2 ⁴ Test direction 1 ⁵ 5 mm radius	2.00E-03	1.09E-04	0.55	4.17	3.73
VP-12.32	Geometry 2 ⁴ Test direction 1 ⁵ 10 mm radius	2.00E-03	1.08E-04	0.55	4.08	3.57
VP-12.35	Geometry 2 ⁴ Test direction 1 ⁵ 20 mm radius	2.00E-03	1.10E-04	0.57	3.91	3.39
VP-12.38	Geometry 2 ⁴ Test direction 2 ⁶ 1 mm radius	2.00E-03	6.85E-06	0.03	2.36	1.68
VP-12.41	Geometry 2 ⁴ Test direction 2 ⁶ 5 mm radius	2.00E-03	2.75E-05	0.14	2.86	2.45
VP-12.44	Geometry 2 ⁴ Test direction 2 ⁶ 10 mm radius	2.00E-03	4.13E-05	0.21	3.09	2.68
VP-12.47	Geometry 2 ⁴ Test direction 2 ⁶ 20 mm radius	2.00E-03	5.99E-05	0.31	3.37	2.83

VP ID	Problem Description	Problem Volume [m ³]	PoF Calculation Volume [m ³]	Ratio of PoF Calculation Volume /Problem Volume [%]	Experimental 50% PoF Load [kN]	Model Prediction 50% PoF Load [kN]
VP-15.01	Sleeve burst test	4.49E-03	4.27E-03	9.52	2.69 [MPa]	2.05 [MPa]
VP-17.01	S70 tensile test	3.89E-04	1.69E-04	4.35	2.64	2.67
VP-17.03	S70 compressive test	3.89E-04	1.28E-04	3.28	11.23	10.10
VP-18.02	Disc internal pressure	8.52E-04	6.63E-04	7.78	10.14 [MPa]	2.03 [MPa]
VP-18.05	Disc external Pressure	8.52E-04	8.52E-04	100	34.82 [MPa]	5.09 [MPa]

¹dogbone shape ²across thickness ³across width ⁴notched bar ⁵notch up ⁶notch down

7.5.3.1 Tensile specimen

Figure 7-3 shows the model prediction, the experimental data and the three-parameter Weibull fit for VP-00. With 370 experimental measurements, this data set is the biggest of the three. A good agreement between the numerical simulation and experimental data is achieved. By definition, the failure methodology is based upon the idealised case of uni-axial tensile fracture and, therefore, good agreement in this VP is expected. A small discrepancy is observed between predictions and test data at a low probability (four data points are not conservatively predicted). In Hindley *et al.* [77], it is shown that this data set does not contain a bimodal distribution. The plot also shows the three parameter and two parameter Weibull distribution for comparison.

7.5.3.2 Bending specimen

Similarly, Figure 7-4 shows the conservative PoF estimates over the full range of four-point bending specimen geometry test data. The data set includes 292 data points. The model prediction shows a very similar slope to the test data. This is expected from the Weibull fit parameters for this data, which is similar to the tensile data shown in Hindley *et al.* [77]. In Hindley *et al.* [77], it is shown that this data set does not contain a bimodal distribution. The plot also shows the three parameter and two parameter Weibull distribution scaled to the mean value of the dataset for comparison.

7.5.3.3 Compressive specimen prediction

The compressive test data are shown in Figure 7-5. A reasonable agreement can be observed between the simulation and the experimental data; however, the slope of the simulation is not as steep as that of the experimental data. This was expected according to the different parameters obtained for the Weibull fit for this data set presented by Hindley *et al.* [77]. Due to the uniform stress states in the uni-axial compressive specimens, the stress magnitude range dictates that only

one group is ever used in the PoF calculation. These 228 data point sets clearly show high numbers of abnormally low strength failures at low PoF. In Hindley *et al.* [77], it is shown that this data set contains a bimodal distribution, although this data set has a far lower variance than the other data sets. However, the failure methodology manages to capture this disparate flaw behaviour conservatively at low probability data points. The plot also shows the three parameter and two parameter Weibull distribution scaled to the mean value of the dataset for comparison.

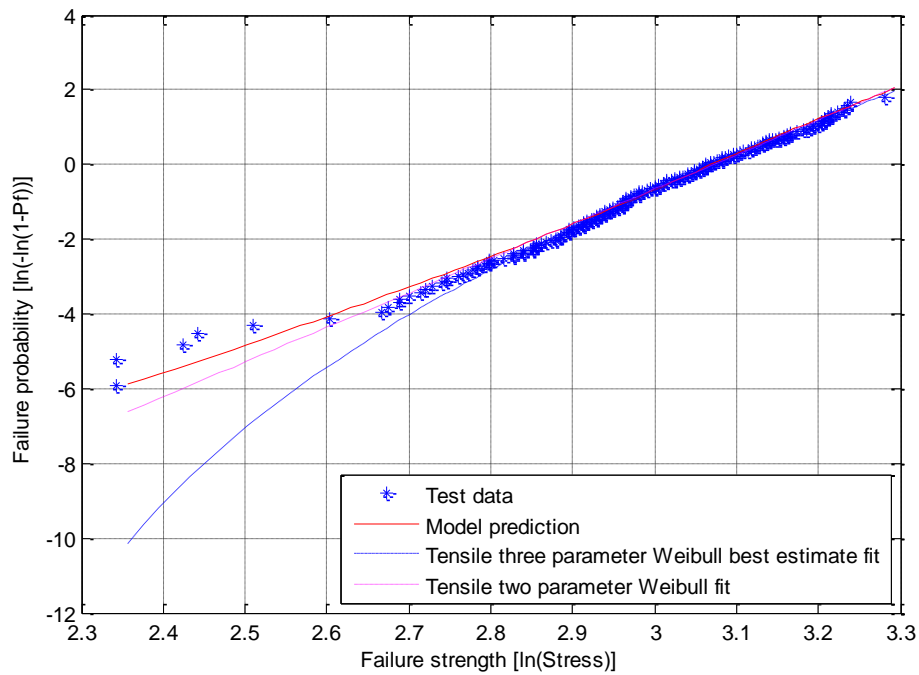


Figure 7-3: VP-00 (tensile specimen) Weibull probability failure prediction plot

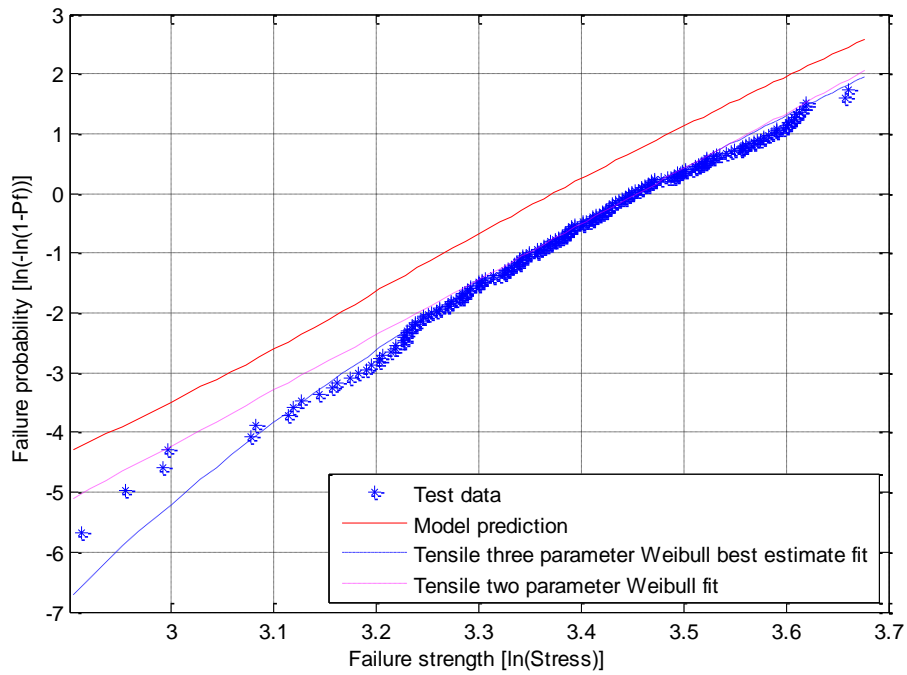


Figure 7-4: VP-01 (four-point bending test) Weibull probability failure prediction plot

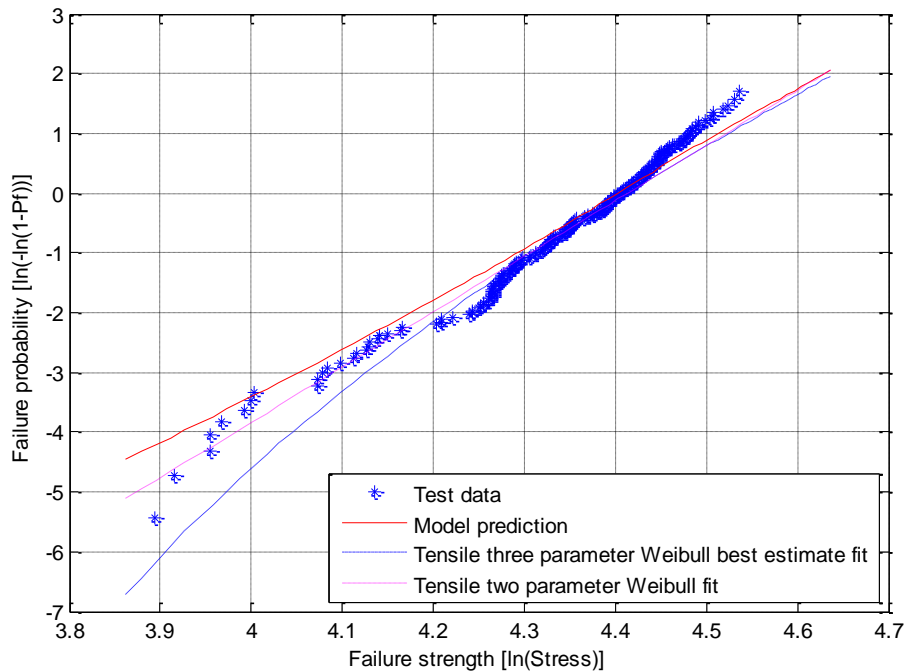


Figure 7-5: VP-02 (compression specimen) Weibull probability failure prediction plot

7.6 Conclusion

Failure probabilities of NBG-18 graphite parts were estimated using a numerically implemented statistical failure methodology. This paper has compared the simulated PoF to those determined from experimental data. To obtain a broad basis for comparison, the test set was chosen to contain specimens of different geometry and sizes, with and without stress-concentrating features, in uni-axial and multi-axial stress states, and in tensile, compressive and flexural test configurations:

- The majority of the 50% PoF load predictions are within the acceptable range (accounting for the variation in billet-to-billet failure strengths). The most accurate PoFs were made for specimens experiencing a uni-axial, or approximately uni-axial, stress state (within 1% of the experimental mean failure load). The PoF for problems with stress-concentrating features and multi-axial stress states were less accurate (within 50% of the experimental mean failure load). The simulations were shown to be either acceptable or conservative.
- PoF simulations were compared with experimental data across a range of failure probabilities and showed reasonable comparison.
- The method showed little mesh sensitivity in the PoF and in some cases reached a converged PoF before a converged FEA mesh solution was used.
- The method showed consistent usability throughout all test cases. Real reactor components are generally designed to exclude stress-concentrating features and, subsequently, the method is expected to deliver acceptable or conservative results for such components across the full range of probabilities.
- The method presented allows for the design of multiple geometries subjected to complex loading conditions. Subsequently, geometric optimisation of components can be performed to ensure conservative life extension as shown by Erasmus and Hindley [103].

Although only a linear elastic FE analysis was used in this paper, the methodology only uses the resultant principal stresses and corresponding volumes in the failure calculation. Therefore, the method has been extended to complex irradiated, non-linear material models as shown in Erasmus and Hindley [103], Erasmus *et al.* [104], and Hindley and Erasmus [105].

8. OPTIMISATION OF THE LINK VOLUME FOR WEAKEST LINK FAILURE PREDICTION IN NBG-18 NUCLEAR GRAPHITE [79]

Michael P Hindley*, Albert A Groenwold**, Deborah C Blaine** and Thorsten H Becker**

*Formerly Pebble Bed Modular Reactor (Pty) Ltd., P.O. Box 9396, Centurion, South Africa 0046

**Department of Mechanical and Mechatronic Engineering, Stellenbosch University, Private Bag X1, Matieland 7602

Keywords

Nuclear graphite, NBG-18, failure prediction

Abstract

This paper describes the process for approximating the optimal size of a link volume required for weakest link failure calculation in nuclear graphite, with NBG-18 used as an example. As part of the failure methodology, the link volume is defined in terms of two grouping criteria. The first criterion is a factor of the maximum grain size and the second criterion is a function of an equivalent stress limit. A methodology for approximating these grouping criteria is presented. The failure methodology employs finite element analysis in order to predict the failure load, at 50% probability of failure. The average experimental failure load, as determined for 26 test geometries, is used to evaluate the accuracy of the weakest link failure calculations. The influence of the two grouping criteria on the failure load prediction is evaluated by defining an error in prediction across all test cases. Mathematical optimisation is used to find the minimum error across a range of test case failure predictions. This minimum error is shown to deliver the most accurate failure prediction across a whole range of components, although some test cases in the range predict conservative failure load. The mathematical optimisation objective function is penalised to account for non-conservative prediction of the failure load for any test case. The optimisation is repeated and a link volume found for conservative failure prediction. The failure prediction for each test case is evaluated, in detail, for the proposed link volumes. Based on the analysis, link design volumes for NBG-18 are recommended for either accurate or conservative failure prediction.

8.1 Introduction

High-temperature gas reactor (HTGR) internals are constructed from ceramic materials capable of withstanding extremely high temperatures. This capability is

an essential property for the passive heat removal feature of modular HTGR designs [106]. Graphite is the predominant ceramic material that serves as an effective neutron moderator and reflector with low neutron absorption properties. The graphite moderator is a major structural component of the reactor while also serving as the conduit for the fuel and the coolant gas. It further provides access for control and safety shut-off devices, and provides thermal and neutron shielding [10].

Nuclear graphite has inherent defects, such as crystal irregularities, pores, inclusions and cracks. These defects can reduce the material strength and act as stress-concentrating features, thus initiating fracture under a low load [15, 26, 30, 42]. The variability of defect size, orientation and random distribution through the material has been shown to lead to a large scatter in experimental material strength test measurements [27, 28, 31, 32, 41, 77, 107]. Graphite behaviour ranges from brittle to quasi-brittle, depending on how the material is processed [15]. Regardless of the processing, the strength of graphite is always stochastic; nominally identical specimens will display a significant deviation in strength from the population mean [15]. The strength of most grades of graphite tends to be transversely isotropic [77]. Due to this material variability, it is difficult, if not impossible, to define an accurate load resulting in failure of the component [78]. One approach for assessing failure is the use of fracture mechanics [23, 44, 46, 49, 52]. The application of the Weibull theory on nuclear graphite has also been studied [22, 26, 28, 35]. All these researchers conclude that the Weibull model is inconsistent with the material behaviour of nuclear graphite. However, Hindley *et al.* [77] find that a Weibull distribution is valid for NBG-18 nuclear grade graphite, and Nemeth *et al.* [27] also show that the Weibull modulus of H-451 graphite is consistent between different tensile specimen sizes and orientations. Strizak [30] investigated the size and volume of nuclear graphite and also concluded that trends are inconsistent with the Weibull theory for small test specimens. Ho [24] finds that the strength of a specimen decreases as the gauge diameter of the specimen decreases below 10 times the maximum grain size (Mgs). Modification of the Weibull theory for the material is proposed to account for this behaviour [24, 36].

Hindley *et al.* [78] present a failure methodology that is capable of predicting failure loads, which are either acceptable or conservative, for various geometries and loading conditions. The implementation of this method has been incorporated into the 2010 American Society of Mechanical Engineers' (ASME's) codes and standards for high-temperature reactors [76]. The methodology is based on the hypothesis that once the volume of the material being analysed reaches a certain size, the dissipation of energy between the microstructural elements is sufficient for the material to show a homogeneous macroscopic failure response. The macroscopic failure response is measured during mechanical testing of components (tensile test, bending test and compressive test). This macroscopic failure response is approximated by a weakest link failure formulation. The approximation is achieved by a volume grouping method, which defines the physical size of a link in the weakest link calculation. The term "link volume" is used to describe the volume of material considered to be necessary for NBG-18 nuclear graphite to exhibit homogeneous macroscopic failure response [78].

In Hindley *et al.* [78] the grouping criteria for defining the size of this link volume are given, without further explanation, as:

- Criterion 1: The minimum link size has a volume greater than $(10 \cdot Mgs)^3$.
- Criterion 2: The maximum difference in equivalent stress Weibull probability is 7%.

The purpose of this paper is to examine the definition of these grouping criteria that control the link volume size and to determine the influence of the link volume size on the accuracy of the failure load prediction. Thereafter, a methodology that approximates the optimal link volume size for accurate or conservative failure prediction in NBG-18 nuclear graphite is presented. It is proposed that this methodology can be applied to other grades of graphite.

8.2 Methodology

8.2.1 Test cases

In Hindley *et al.* [78], 26 test cases are used to illustrate the presented failure prediction methodology. These test cases are summarised in Table 8-1. To assist with understanding the results presented, the verification problem (VP) numbers are presented in accordance with Hindley *et al.* [78]; however, for simplification, the problems are renumbered 1 to 26 throughout the rest of this paper. Table 8-1 shows the average failure load as measured from experimental results as well as the total component volume. This illustrates the range of component sizes that was tested as well as the different geometries tested as per the problem description. This paper handles predictions at 50% probability of failure (PoF), equivalent to the average experimentally determined failure load. For most test cases, the maximum applied force at failure is reported; for the test cases that were tested using pressure, the maximum failure pressure reported is indicated in Table 8-1.

Table 8-1: Test case geometry descriptions [78]

Test Case No.	VP ID	Problem Description	Average Experimental Failure Load [kN]	Component Volume [m³]
1	VP-00.02	Tensile sample, ends loaded	6.50	9.09E-04
2	VP-00.05	Tensile sample, clamped	6.50	9.09E-04
3	VP-01.02	Four-point bend	2.69	1.56E-04
4	VP-19.01	Compressive cylinder	24.91	1.26E-05
5	VP-19.03	Compressive cube	33.74	8.00E-06
6	VP-12.02	Geometry 1 ¹ Test direction 1 ² 1 mm radius	9.66	6.14E-03

Test Case No.	VP ID	Problem Description	Average Experimental Failure Load [kN]	Component Volume [m³]
7	VP-12.05	Geometry 1 ¹ Test direction 1 ² 5 mm radius	10.25	6.15E-03
8	VP-12.08	Geometry 1 ¹ Test direction 1 ² 10 mm radius	10.99	6.16E-03
9	VP-12.11	Geometry 1 ¹ Test direction 2 ³ 20 mm radius	11.26	6.23E-03
10	VP-12.14	Geometry 1 ¹ Test direction 2 ³ 1 mm radius	7.10	6.14E-03
11	VP-12.17	Geometry 1 ¹ Test direction 2 ³ 5 mm radius	7.65	6.15E-03
12	VP-12.20	Geometry 1 ¹ Test direction 2 ³ 10 mm radius	8.01	6.16E-03
13	VP-12.23	Geometry 1 ¹ Test direction 2 ³ 20 mm radius	8.57	6.23E-03
14	VP-12.26	Geometry 2 ⁴ Test direction 1 ⁵ 1 mm radius	4.43	2.01E-03
15	VP-12.29	Geometry 2 ⁴ Test direction 1 ⁵ 5 mm radius	4.17	2.00E-03
16	VP-12.32	Geometry 2 ⁴ Test direction 1 ⁵ 10 mm radius	4.08	1.98E-03
17	VP-12.35	Geometry 2 ⁴ Test direction 1 ⁵ 20 mm radius	3.91	1.94E-03
18	VP-12.38	Geometry 2 ⁴ Test direction 2 ⁶ 1 mm radius	2.36	2.01E-03
19	VP-12.41	Geometry 2 ⁴ Test direction 2 ⁶ 5 mm radius	2.86	2.00E-03
20	VP-12.44	Geometry 2 ⁴ Test direction 2 ⁶ 10 mm radius	3.09	1.98E-03
21	VP-12.47	Geometry 2 ⁴ Test direction 2 ⁶ 20 mm radius	3.37	1.94E-03
22	VP-15.01	Sleeve burst test	2.69 (MPa)	4.48E-03
23	VP-17.01	S70 tensile test	2.64	3.89E-04
24	VP-17.03	S70 compressive test	11.23	3.89E-04
25	VP-18.02	Disc internal pressure	10.14 (MPa)	8.52E-04
26	VP-18.05	Disc external pressure	34.82 (MPa)	8.52E-04

¹dogbone shape ²across thickness ³across width ⁴notched bar ⁵notch up ⁶notch down

8.2.2 Failure methodology

Hindley *et al.* [78] provide a detailed numerical procedure for calculating the PoF for a graphite component under a specific load. Figure 8-1 summarises the procedure by means of a flow diagram. The procedure follows a grouped

weakest link calculation. The grouping is performed by summing finite element analysis (FEA) element volumes until a specific link volume, defined by two grouping criteria as highlighted in Figure 8-1, is reached. This is conducted for each link in the weakest link calculation. The two grouping criteria are defined as follows:

The first criterion is volume-based, defined as a factor (F) of the Mgs for the material under observation,

$$V_{mgs} = F \bullet Mgs \quad (8-1)$$

The second criterion is defined by a stress limit in a group; when this limit is exceeded, a new group is started. The limit is defined as the difference between the maximum and minimum equivalent stress intensity in Weibull probability in a group [78].

$$\Delta X_i = \max(X_i) - \min(X_i) \quad (8-2)$$

Where

$$X_i = \left\{ \begin{array}{ll} \left[\frac{\sigma_i - S_0'}{S_c - S_0'} \right]^m & \sigma_i > S_0' \\ 0 & \sigma_i < S_0' \end{array} \right\} \quad (8-3)$$

where the equivalent stress intensity, σ_i , is defined as the maximum deformation energy (MDE) stress [57]. The weibull parameters in Equation 8-3 are the characteristic strength S_c , the shape parameter m and the threshold value S_0 .

In Hindley *et al.* [78] the two grouping criteria are defined by $F = 10$ in Equation 8-1 and $\Delta X_i = 0.07$ (7%) in Equation 8-2. For NBG-18 nuclear graphite evaluated in this paper, the Mgs is specified, as per the material data sheet from the supplier, as 1.6 mm (supplier: SGL Carbon). The validity of these definitions for the two grouping criteria is the subject of investigation throughout the rest of this paper. Furthermore, the influence of using only one grouping criteria is also investigated.

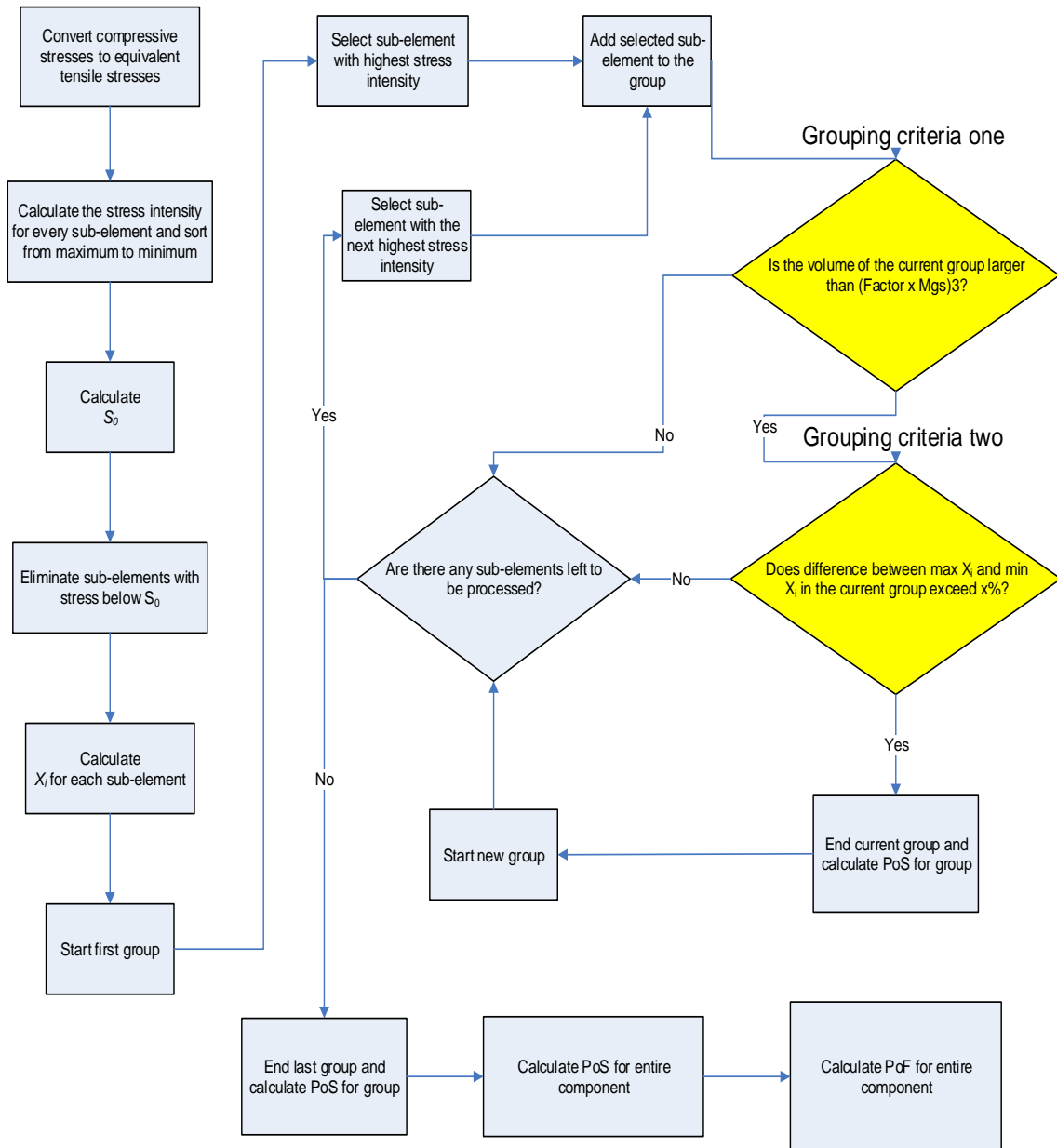


Figure 8-1: Flow diagram of failure methodology highlighting grouping criteria

While the link volume size is defined by these variable grouping criteria, the weakest link failure calculation methodology requires input from an FEA of the test case and statistical parameters. An FEA analysis of the test case is conducted with the applied load equivalent to the experimentally measured 50% PoF (average) load. The resultant principal stresses are used to calculate the MDE stress for the second grouping criterion, and Gauss integration volume of the material associated to the principal stresses is used to determine the link volume for the first grouping criterion. The links are used in combination with statistical parameters [77] to predict a PoF for the test case.

As the applied load is chosen as the experimentally measured average load, the calculation will only yield a predicted 50% PoF if the failure methodology is accurate. As such, the predicted PoF is not necessarily 50%. The predicted PoF changes by changing the grouping criteria limits. The optimal grouping criteria limits are those that produce the most accurate failure load prediction, as determined by producing a predicted PoF of 50% when the experimentally measured average failure load is applied to the FEA of the test case.

Alternatively, for a given set of grouping criteria, the load applied in the FEA can be scaled by a load factor, f , to achieve a predicted PoF of 50%. An iterative process is followed until the predicted PoF reaches 50% within accuracy of $\pm 0.01\%$. It should be noted that the link volume grouping is recalculated for each iteration. While convergence to 50.00% PoF has been found over all the test cases defined in Table 8-1 for all grouping combinations evaluated throughout this paper, no claims to proof of convergence are necessarily implied.

Consequently, an error between the predicted failure load that gives a 50% PoF and the experimentally measured average failure load exists for each test case. This error is defined by the deviation of the load factor, f from 1.0, and so carries the same weight for all test cases.

The root mean square (RMS) error is used as the measure of error for the calculation as it is especially useful when the error is either positive or negative, and it severely penalises poor predictions. Thus, the RMS error for each test case and specific grouping criteria is calculated:

$$RMS_i = (1 - f_i)^2 \quad (8-4)$$

Where

f_i = the predicted load factor for each test case i .

In order to determine the optimal grouping criteria limits for the specific material studied, NBG-18, all the test cases are taken into account and an average error is calculated as:

$$RMS_{average} = \frac{\sum_{i=1}^N RMS_i}{N} \quad (8-5)$$

Where

N = the total number of test cases.

Using the average error allows for new experimental test cases to be added to the data set and compared.

8.2.3 Optimisation methodology

Mathematical optimisation is used to obtain the point at which the minimum error, defined by the RMS average in Equation 8-5, occurs. Formally, mathematical optimisation is the process of minimising an objective function, possibly subject to a set of limitations or constraints, see for example Nocedal and Wright [108, 109] and many others. Indeed, mathematical optimisation allows for the penalisation of undesired results. In our case, the objective function is penalised to prevent non-conservative prediction of the failure load in any test case. To achieve this, a penalty function is added to the RMS error definition, Equation 8-4, for any test case where the failure load is non-conservative. For any problem that has a predicted load factor larger than a prescribed limit, C , a (positive) penalty value, P , is added to the RMS error:

$$RMS_i = \begin{cases} (1 - f_i)^2 & \text{if } f_i \leq C \\ ((1 - f_i)^2 + P) & \text{if } f_i > C \end{cases} \quad (8-6)$$

Subsequently, if the failure load for the test case is under-predicted, the penalty, P , is added and the error is recalculated accordingly.

The limits of acceptability for the material strength for NBG-18 are defined by Mitchell [94] and revisited by Hindley *et al.* [77]. The analysis of a set of 24 NBG-18 billet experiments reveals the following [94]:

- The tensile strength (TS) of 50% of billets falls within $\pm 6\%$ of the material strength average.
- The TS of 95% of billets falls within $\pm 18\%$ of the material strength average.

The prescribed limit C activates the penalty function for test cases where the load factor f exceeds 1.00; in other words, where the applied load must be scaled up from the experimentally measured average failure load to achieve a PoF of 50%. The limits considered are 0% (1.00), 6% (1.06) and 18% (1.18) that align with the material strength ranges given above. Furthermore, to ascertain the influence of the second grouping criterion (equivalent stress range limit), this criterion is removed and the optimum value is determined for the first grouping criterion only (V_{Mgs}).

To evaluate the influence of the two grouping criteria on a global scale, an error response surface is developed by evaluating Equation 8-5 at discrete points. The same process for a prescribed limit C of 1.00 is used in Equation 8-6. These response surfaces help with a general understanding of the influence of the grouping criterion on all problems. However, evaluation at discrete points may miss points of local minima or maxima; thus a search for the minimum error is done using mathematical optimisation.

The true objective function may be “noisy”, thereby requiring a more robust optimisation method. A suitable method is the so-called leap-frog optimisation (LFOP) algorithm of Snyman [110-112], which is used in this paper. There are a myriad of other routines that are capable of delivering the same results shown in this paper although non-gradient based methods are recommended. However, the results obtained during optimisation are the focus of the contents to follow, and not the optimisation method or speed at which the optimisation method reaches the optimum. The optimisation is performed for the unpenalised objective function given in Equation 8-5 and the penalised objective function given in Equation 8-6, with the aforementioned prescribed limits.

8.3 Results

8.3.1 Response surface

8.3.1.1 Unpenalised response surface

The contours formed in the response surface allow for the computation of a minimum error. The response surface in Figure 8-2 was created by plotting the RMS average at increments of grouping criterion one by 0.5 and grouping criterion two by 0.05. The response surface is a good indication of the global response of the defined error function.

In Figure 8-2 the response surface shows a maximum (large error) in close proximity to the point where both criteria approach zero. This is because very small link volumes are formed. The PoF for the components is the product of PoFs for every link volume and all test case predictions become very conservative (the average RMS error becomes large). On the ends, where both grouping criteria become large, the failure prediction trends to one link volume per test case, which is essentially a standard Weibull weakest link failure model with three parameters.

An interesting part of this response surface is the minima valley that occurs when the first grouping criterion is between 10•Mgs and 18•Mgs. This indicates a grouping combination that produces an error far lower than a classic Weibull weakest link failure model, which would only form one group, over a whole range of test cases. The grouping range in which the minima occurs correlates with the gauge diameter and grain size effect experimentally reported by Ho [24] (between 10•Mgs and 15•Mgs).

The RMS average in this minima valley is less dependent on grouping criterion two (smaller variations in RMS average error). With the second grouping criterion set to zero, the problem reduces to a line on the Y axis of Figure 8-2. The initial values used by Hindley *et al.* [78] plotted in Figure 8-2 produce an error larger than that of the optimum point. This implies that the grouping criteria values at the optimum point of the surface predict failure more accurately than the values proposed in Hindley *et al.* [78].

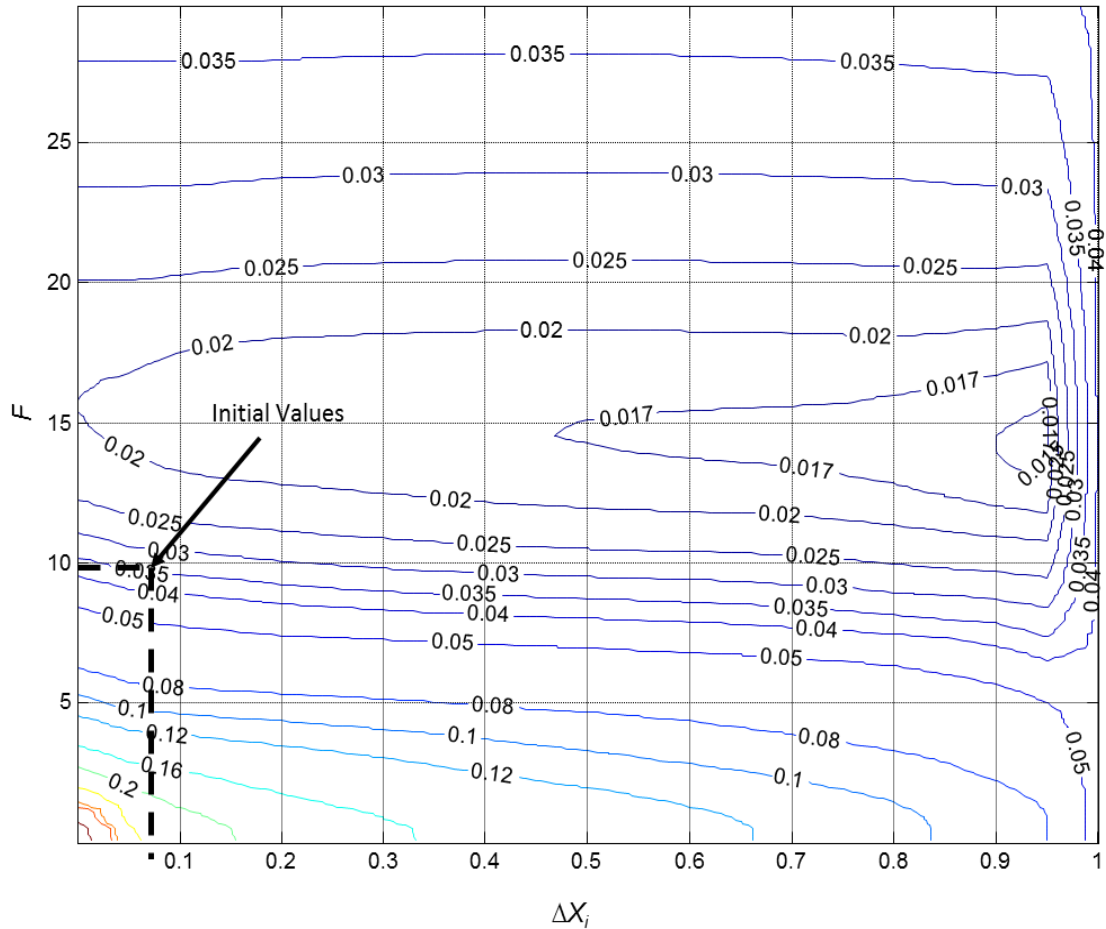


Figure 8-2: Unpenalised error (RMS average) function

8.3.1.2 Penalised response surface

The response surface in Figure 8-3 was created using a prescribed limit of 1.00 and plotting the RMS average at increments of 0.5 for grouping criterion one and 0.05 for grouping criterion two. A penalty value of 1 would constitute a 100% error in failure prediction. Therefore, a penalty value of 0.5 is applied for any test case where the load factor exceeds 1.00. This penalty value is larger than any real error produced during failure calculation yet small enough to allow for visual comparison in Figure 8-3. In Figure 8-3, the minima valley moved closer to 10•Mgs and the value of the error rapidly grew larger, as the first criteria approached 12•Mgs to 30•Mgs. This shows that when grouping criterion one is larger than 10•Mgs the failure load for some test cases is non-conservative. For grouping criterion two, the minima moves from a high stress limit value 0.95, as seen in Figure 8-2, to a low stress limit value 0.2, as seen in Figure 8-3. This indicates that a high stress limit also results in a non-conservative prediction of the failure load for some test cases. The initial values used by Hindley *et al.* [78] are plotted in Figure 8-3 and show correlation to the optimum point for the penalised problem.

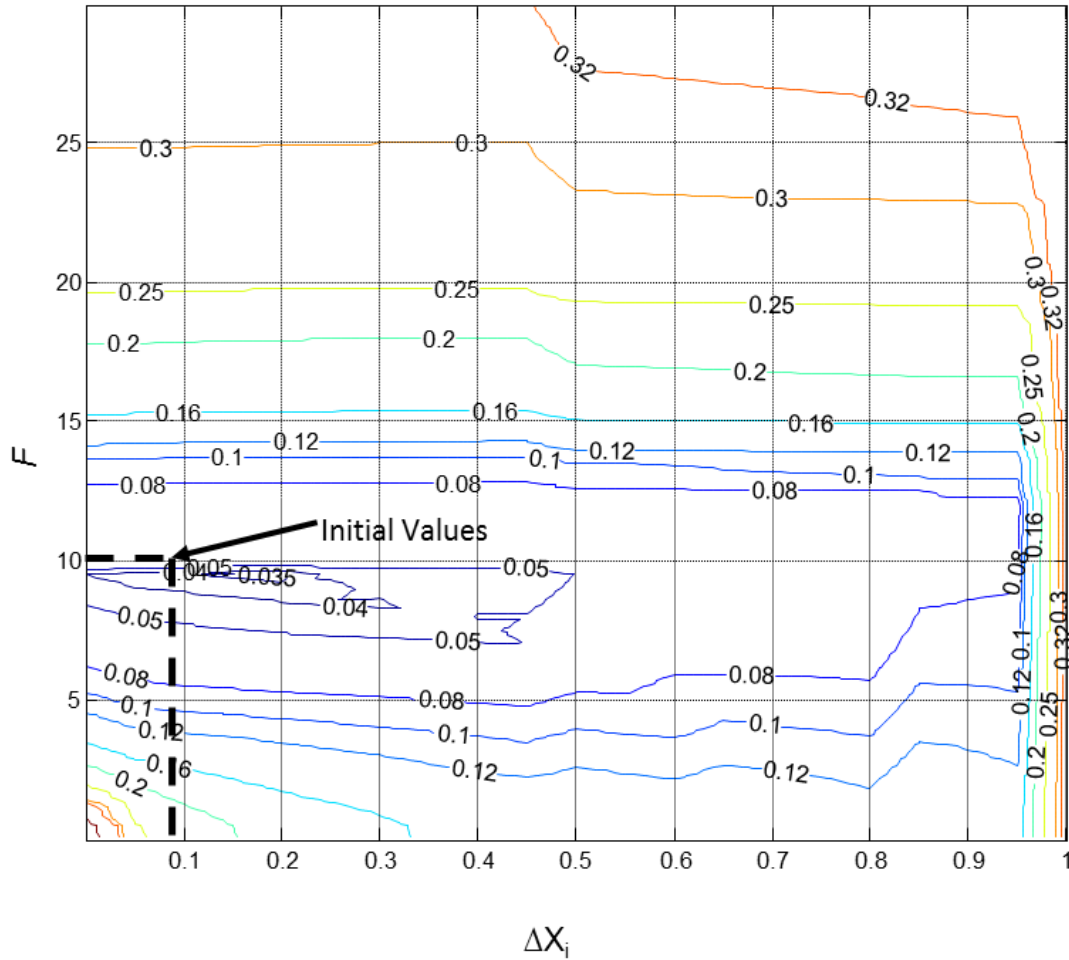


Figure 8-3: Penalised error (RMS average) function penalised by 0.5 for error larger than 1.00

8.3.2 Optimisation volume results

The results obtained through the mathematical optimisation using the corresponding RMS average for various scenarios are provided in Table 8-2. The classic Weibull weakest link method, using three parameters (i.e. one link volume), yields an RMS average error of 0.129. All the respective optimum values, shown in Table 8-2, yield RMS average errors that are smaller than the classic three-parameter Weibull weakest link method.

In Table 8-2, the initial values used in Hindley *et al.* [78] provide an RMS average error similar to that obtained when using a prescribed limit of 1.00. The unpenalised results reduce the RMS average error by more than half as compared to when a prescribed limit of 1.00 is used. The error systematically reduces as the prescribed limit is lifted from 1.00 to 1.06 and 1.18, respectively. The penalised results with a prescribed limit of 1.18 and the unpenalised results

have the same optimum values, implying that at the minimum average RMS error, no single test case under-predicts the failure load by more than 18%.

Table 8-2: Optimisation results

<i>Optimisation</i>	<i>Criterion One (Factor of Mgs)</i>	<i>Criterion Two (Stress Limit)</i>	<i>RMS Error Average</i>	<i>Prescribed Limit</i>
Initial values [78]	10.00	0.0700	0.0328	N/A
Unpenalised	14.45	0.9975	0.0126	N/A
Single criterion unpenalised	15.53	N/A	0.0200	N/A
Penalised 1.00	9.73	0.2055	0.0318	1.00
Penalised 1.06	11.59	0.6596	0.0204	1.06
Penalised 1.18	14.45	0.9975	0.0126	1.18
Three-parameter Weibull	N/A	N/A	0.1290	N/A

The influence of significant digits required in the grouping is now investigated. The significant digits are varied for the unpenalised problem and the influence on the RMS error is given in Table 8-3. From Table 8-3, it can be seen that grouping criterion one is sensitive up to a resolution of 0.1•Mgs and grouping criterion two up to 0.01 (or 1%) of the stress limit.

Table 8-3: Significant digits affecting grouping criteria for unpenalised grouping

<i>Criterion One</i>	<i>Criterion Two</i>	<i>RMS Error Average</i>
14.45	0.9975	0.0126
14.45	0.9970	0.0126
14.45	0.9900	0.0133
14.45	0.9000	0.0150
14.40	0.9975	0.0126
14.00	0.9975	0.0127
14.50	0.9900	0.0127

8.4 Discussion: Individual test case error prediction

To understand the implications of the optimum values obtained, the failure prediction of each test case needs to be examined individually. For each of the optimum grouping criterion values obtained through the numerical optimisation, the individual test case failure predictions are investigated.

8.4.1 Unpenalised individual test case predictions

Table 8-4 presents the failure prediction for each of the optimum link volumes for each test case in Table 8-1. Table 8-4 shows results for both the unpenalised results and the single criterion unpenalised results. Figure 8-4 shows a plot of the load factor f for the unpenalised results, similar to the representation in Hindley *et al.* [78], for the 26 test cases. The relative plot shows the 6% (lines at 0.94 and 1.06) and 18% (lines at 0.82 and 1.18) limits, which allow for visualisation of prediction relative to the acceptable limits of strength variation in the material. In Figure 8-4 and in Table 8-4, the failure predictions are mostly within the acceptable limits [78, 94] over a wide range of test cases. Two of the predicted values fall outside the accepted variance in the material strength [78, 94] and both of these are conservative. Eleven of the 26 test cases fall outside of the 6% limit and only two test cases fall outside of the 18% limit. Table 8-4 also presents the single criterion unpenalised failure prediction results for each test case. In most of the test cases, the results are the same except for test case 22, which is the sleeve burst test. This test case changes the predicted load factor from 1.177 for unpenalised results to 0.732 for single criterion unpenalised results. Table 8-4 also gives the PoF calculation volume as calculated by the grouping. The different grouping criteria do yield different PoF calculation volumes.

Although the second grouping criterion does not seem to have a large influence on the RMS average, it has a dramatic effect on individual test cases. The second grouping criterion also increases the accuracy of the overall failure prediction. For all the other test cases, the single criterion method is less accurate than when both criteria are considered. However, if only a small amount of test data is available, it may be necessary to determine the link volume with the use of only one criterion. For instance, consider the first four test cases: two tensile, one bending and one compressive loading scenario. If this was the only data available, an optimum in terms of two criteria may not have been obtainable.

Table 8-4: Failure prediction for unpenalised results

Test Case	<i>Unpenalised</i>			<i>Single Criterion Unpenalised</i>			Difference Load Scale Prediction
	Predicted Load Factor	No. of Links	PoF Calculation Volume [m3]	Predicted Load Factor	No. of Links	PoF Calculation Volume [m3]	
1	1.133	3	2.56E-04	1.15	3	2.65E-04	-0.017
2	1.132	4	3.70E-04	1.15	4	3.82E-04	-0.018
3	1.041	2	1.54E-05	1.068	2	1.59E-05	-0.027
4	0.99	1	1.26E-05	0.99	1	1.26E-05	0
5	0.931	1	8.00E-06	0.931	1	8.00E-06	0
6	0.991	4	2.82E-04	1.018	5	2.95E-04	-0.027
7	1.056	5	3.43E-04	1.076	6	3.53E-04	-0.02
8	1.028	5	3.63E-04	1.039	7	3.71E-04	-0.011
9	1.09	5	4.16E-04	1.066	7	4.00E-04	0.024

	<i>Unpenalised</i>			<i>Single Criterion Unpenalised</i>			
10	0.839	4	1.63E-04	0.864	3	1.70E-04	-0.025
11	0.915	4	1.94E-04	0.937	4	1.99E-04	-0.022
12	0.937	4	1.93E-04	0.94	4	1.94E-04	-0.003
13	0.925	4	1.69E-04	0.932	3	1.70E-04	-0.007
14	0.996	3	1.12E-04	1.022	2	1.17E-04	-0.026
15	1.006	3	1.09E-04	1.032	2	1.14E-04	-0.026
16	0.987	3	1.08E-04	1.012	2	1.12E-04	-0.025
17	0.976	3	1.10E-04	1.001	2	1.15E-04	-0.025
18	0.713	1	6.85E-06	0.713	1	6.85E-06	0
19	0.912	1	2.75E-05	0.912	1	2.75E-05	0
20	0.965	1	4.13E-05	0.965	1	4.13E-05	0
21	0.952	2	6.00E-05	0.977	2	6.26E-05	-0.025
22	1.177	4	4.27E-03	0.732	70	4.24E-03	0.445
23	1.135	2	1.69E-04	1.163	2	1.81E-04	-0.028
24	1.012	2	1.28E-04	1.036	2	1.30E-04	-0.024
25	0.896	5	6.63E-04	0.771	10	5.76E-04	0.125
26	0.722	2	8.52E-04	0.58	14	8.52E-04	0.142

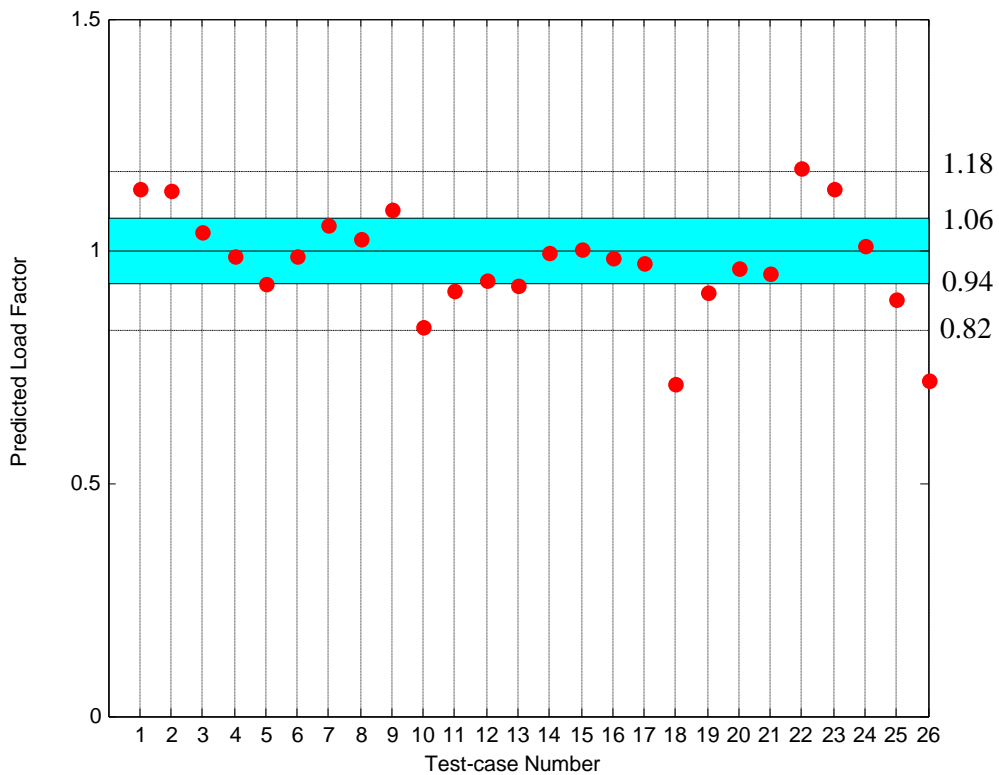


Figure 8-4: Unpenalised failure prediction results

8.4.2 Penalised individual test case predictions

Table 8-5 presents the failure prediction parameters for each test case for all the penalised results. For a prescribed limit of 1.00, most of the test cases only show a small improvement in prediction when compared to the original criteria. However, Test case 22 (sleeve burst test) shows a significant improvement of 10%, placing the test case in the acceptable region when compared to the original criteria. Figure 8-5 shows the plot of the load factor f for the results where test cases with load factors exceeding 1.00 are penalised. In Figure 8-5, seven test cases are predicted outside the acceptable range. In Figure 8-6, the failure prediction is plotted for the scenario where the prescribed limit is lifted to 1.06. The outcome is that four of the test cases fall beyond the accepted limits. The relative plot when the prescribed limit is lifted to 1.18 is not shown, since the values are identical to the unpenalised results. Similarly, the load factor and number of links used for the scenario where the prescribed limit is set to 1.18 is not given in Table 8-5 since the value is the same as in Table 8-4. However, all the penalised results and original results are presented in Table 8-5. The unpenalised results in Table 8-4 predict failure of fewer links than the penalised results in Table 8-5.

8.5 Summary

A volume grouping method, based on a defined link volume, is used to predict failure for NBG-18 nuclear graphite material. The link volume is defined in terms of two grouping criteria. The first a factor (F) of the Mgs and the second a stress limit (ΔX_i). In order to assess the influence that each of these criteria have on the failure prediction, an error is defined in terms of a predicted load factor for each test case. The errors for all test cases are combined into an average error across all test cases. This error function is used to assess the influence of these grouping criteria on failure predictions.

Firstly, the two criteria are varied discretely to form an error response surface in Figure 8-2. In Figure 8-2 a minima valley validates the assumption that a link volume does exist in NBG-18 nuclear graphite. From the response surface in Figure 8-2 the error in prediction is more dependent on grouping criterion one than on criterion two. Subsequently, when minimal test data is available, it may be sufficient to use only one grouping criterion to approximate the link volume.

A penalty function is used to limit the load factor to a value below 1.00, forcing the failure load prediction to be conservative. It is apparent from Figure 8-3 that the grouping criterion needs to be smaller than the unpenalised scenario to ensure conservative failure prediction (i.e. more groups result in more conservative failure prediction).

Thereafter, mathematical optimisation is used to locate the point at which the minimum error occurs. This is done for the unpenalised scenario first. The individual prediction for each test case is discussed at this point. Two of the 26 test cases are not within the acceptable limits of the material. These two test cases are predicted conservatively at approximately 70% of the 50% PoF.

Table 8-5: Failure prediction for penalised results

Test Case	<i>Original Values</i>			<i>Penalised 1.00</i>			<i>Penalised 1.06</i>		
	Load Factor	No. of Links	PoF Calculation Volume [m3]	Load Factor	No. of Links	PoF Calculation Volume [m3]	Load Factor	No. of Links	PoF Calculation Volume [m3]
1	1.002	7	2.01E-04	0.994	7	1.99E-04	1.048	5	2.18E-04
2	1.002	9	2.74E-04	0.994	9	2.67E-04	1.048	7	3.09E-04
3	0.921	4	1.32E-05	0.913	4	1.30E-05	0.967	3	1.42E-05
4	0.990	1	1.26E-05	0.990	1	1.26E-05	0.990	1	1.26E-05
5	0.931	1	8.00E-06	0.931	1	8.00E-06	0.931	1	8.00E-06
6	0.864	14	2.22E-04	0.855	15	2.18E-04	0.912	10	2.45E-04
7	0.935	18	2.79E-04	0.927	19	2.76E-04	0.979	12	3.03E-04
8	0.907	18	2.93E-04	0.899	20	2.89E-04	0.948	13	3.17E-04
9	0.931	19	3.06E-04	0.923	20	3.02E-04	0.973	14	3.34E-04
10	0.729	8	1.31E-04	0.721	9	1.28E-04	0.771	6	1.44E-04
11	0.810	10	1.61E-04	0.803	11	1.60E-04	0.850	7	1.70E-04
12	0.818	10	1.55E-04	0.811	11	1.54E-04	0.856	7	1.71E-04
13	0.811	9	1.35E-04	0.805	9	1.33E-04	0.849	6	1.47E-04
14	0.884	6	9.04E-05	0.876	6	8.91E-05	0.927	4	9.83E-05
15	0.892	6	8.85E-05	0.885	6	8.72E-05	0.936	4	9.63E-05
16	0.875	6	8.81E-05	0.868	6	8.70E-05	0.918	4	9.64E-05
17	0.867	6	9.09E-05	0.859	6	8.91E-05	0.909	4	9.76E-05
18	0.713	1	6.85E-06	0.713	1	6.85E-06	0.713	1	6.85E-06
19	0.856	2	2.39E-05	0.847	2	2.34E-05	0.903	2	2.68E-05
20	0.866	3	3.36E-05	0.858	3	3.30E-05	0.912	2	3.79E-05
21	0.840	3	4.77E-05	0.833	4	4.72E-05	0.883	3	5.29E-05
22	0.765	96	4.24E-03	0.879	51	4.24E-03	1.056	15	4.24E-03
23	1.010	5	1.42E-04	1.00	5	1.42E-04	1.059	3	1.42E-04
24	0.899	4	1.20E-04	0.891	4	1.20E-04	0.944	3	1.20E-04
25	0.672	34	5.41E-04	0.682	35	5.41E-04	0.748	17	5.58E-04
26	0.501	53	8.52E-04	0.516	49	8.52E-04	0.575	15	8.52E-04

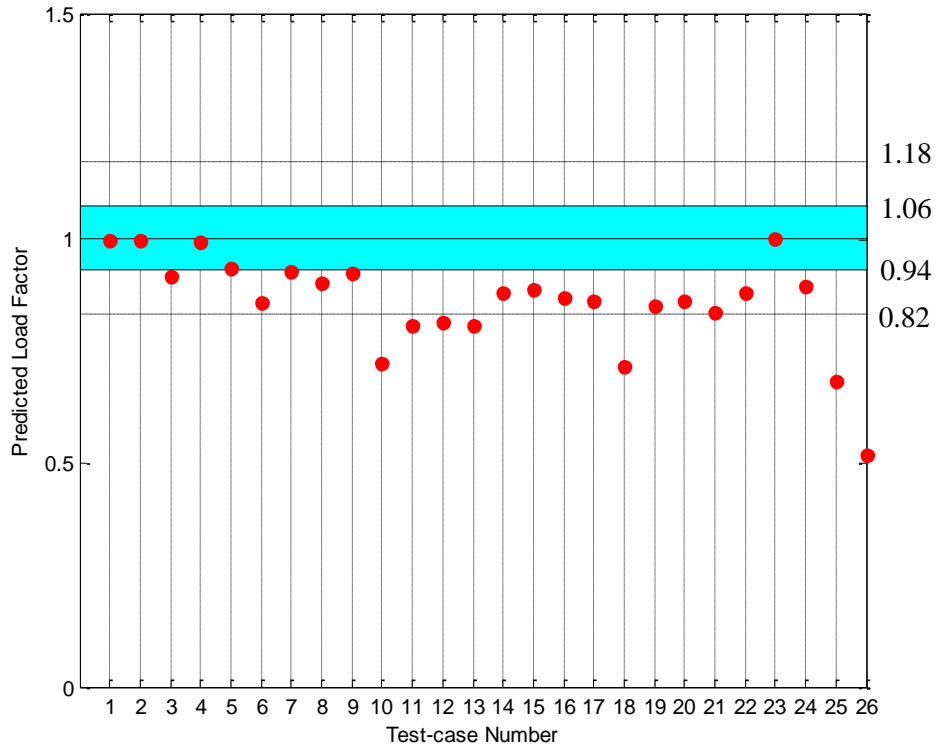


Figure 8-5: Penalised failure prediction results for load factors exceeding 1.00

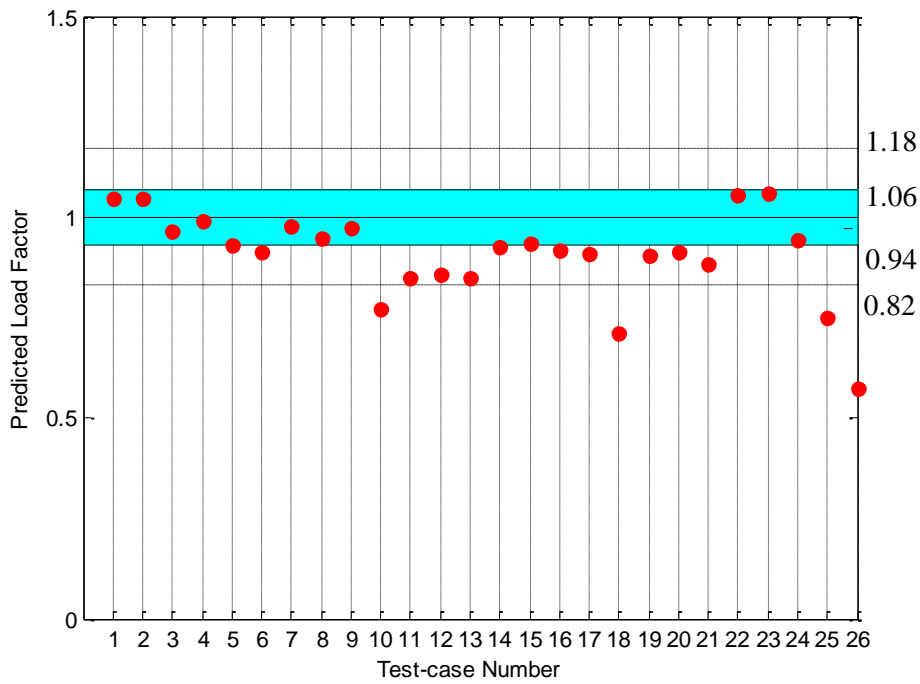


Figure 8-6: Penalised failure prediction results for load factors exceeding 1.06

The optimisation is repeated with a penalty function active for test cases where the load factor is above the prescribed limit. The process is repeated for different limits. A minimum error, indicating an optimum point, is obtained for each scenario. The failure prediction for each scenario is evaluated. The obtained link volume criteria, for an unpenalised optimum (best accuracy values) and the optimum for penalised results with a prescribed limit of 1.00 (the most conservative prediction) for the NBG-18 nuclear graphite are presented in Table 8-6.

Table 8-6: Obtained link volume values for NBG-18 failure prediction

<i>Use</i>	<i>Criterion One</i>	<i>Criterion Two</i>
Unpenalised optimum (best accuracy values)	14.45	0.99
Penalised optimum with limit set to 1.00 (conservative reactor design values)	9.73	0.20

8.6 Conclusion

When designing test setups, experimental test equipment has load limitations. To ensure that the load limitations are met during test setup design it is recommended to use the most accurate grouping criteria. For NBG-18, the most accurate grouping criteria is $F = 14.45$ and $\Delta X_i = 0.99$

The most conservative failure predictions are found when penalising the results using a prescribed load factor limit of 1.00. For NBG-18 the most conservative grouping criteria is $F = 9.73$ and $\Delta X_i = 0.20$. Using these penalised results is recommended for the design of reactor components, since it ensures conservatism in predictions. Although the values presented here are applicable to NBG-18, the same methodology can be used to approximate link volumes for other grades of graphite.

The failure methodology is capable of handling various geometries and complex loading conditions. This allows for geometric topology optimisation, as shown in Erasmus and Hindley [103]. The possibility of changing the geometry allows the designer to achieve substantially longer lifetimes while ensuring conservatism as demonstrated by Erasmus and Hindley [103].

9. FAILURE PREDICTION OF FULL-SIZE REACTOR COMPONENTS FROM TENSILE SPECIMEN DATA ON NBG-18 NUCLEAR GRAPHITE [80]

Michael P Hindley*, Deborah C Blaine**, Albert A Groenwold** and Thorsten H Becker**

*Formerly Pebble Bed Modular Reactor (Pty) Ltd., P.O. Box 9396, Centurion, South Africa 0046

**Department of Mechanical and Mechatronic Engineering, Stellenbosch University, Private Bag X1, Matieland 7602

Keywords

Nuclear graphite, NBG-18, failure prediction

Abstract

This paper concerns itself with predicting the failure of a full-size NBG-18 nuclear graphite reactor component based only on test data obtained from standard tensile test specimens. A full-size specimen structural test was developed to simulate the same failure conditions expected during a normal operation of the reactor in order to validate the failure prediction. The full-size specimen designed for this test is almost a hundred times larger than the tensile test specimen, has a completely different geometry and experiences a different loading condition to the standard tensile test specimen. Failure of the full-size component is predicted realistically, but conservatively.

9.1 Introduction

The core of a high-temperature gas reactor (HTGR) makes use of nuclear graphite as a moderator, reflector and as structural material. The reflectors of the core structures of a typical reactor consist of nuclear graphite blocks that, when assembled, perform both reflection and structural functions [11]. These parts are subject to both the high temperatures at which the core operates, as well as high levels of fast neutron flux [11].

Fast neutron irradiation alters graphite properties. These alterations take the form of irradiation induced dimensional change, as well as changes of the thermal and mechanical properties of the material.

These irradiation induced effects lead to the build-up of internal stress within a part. At some stage, the internal stresses may reach a level which results in the failure of the part.

Nuclear graphite is a quasi-brittle material and has the presence of inherent defects, such as crystal irregularities, pores, inclusions and cracks. These defects can reduce the material strength and act as stress-concentrating features and can thus initiate material failure under sufficient applied stress. The variability of defect size and orientation and their random distribution through the material volume leads to a large scatter in experimental material strength test measurements. This makes it difficult to define the load at which the material will fail [78].

Fracture of brittle materials usually initiates from flaws which are randomly distributed in the material [59]. The strength of the specimen depends on the size and the shape of the major flaw, which vary between specimens, and on the load orientation. Therefore, the strength of brittle materials is typically described by probability functions [60-63]. Experiments show that the probability of failure (PoF) increases with the load and also with the size of the specimens [60, 61, 64]. This is due to the fact that it is more likely to find a major flaw in a large specimen than finding it in a small specimen. This occurrence is especially true for brittle and porous materials, such as ceramics [113-115]. Therefore, the mean strength of larger specimens is lower than the mean strength of smaller specimens. This size effect on strength is the most prominent and relevant consequence of the statistical behaviour of strength in brittle materials [65].

Traditionally, the size effect in the failure of brittle material has been explained using Weibull's statistical theory [66, 71]. The Weibull theory, in which the strength of a brittle solid is assumed to be controlled by flaws, has potential uses in the engineering design of load bearing structures made from brittle materials, because it relates the PoF to the volume of material under load, the stress gradient and multi-axial stress states [15, 28]. Nuclear graphite, however, does not show this size effect [24, 27, 30, 74, 79, 107]. Furthermore, Brocklehurst and Darby [22], Mitchell *et al.* [35] and Price [28] all concluded that the Weibull model is inconsistent with the material behaviour of nuclear graphite.

A failure methodology based on the Weibull theory, which is capable of predicting either accurate or conservative failure loads for components of various geometries that experience varying loading conditions, has been presented by Hindley *et al.* [78]. The implementation of this method has been incorporated into the latest 2010 American Society of Mechanical Engineers' (ASME's) code and standards for high-temperature gas reactors (HTGRs) [76].

The purpose of the work presented here is the application of this new failure prediction methodology [78] to actual components designed for a pebble bed modular reactor [116]. The literature covering the development of the failure prediction methodology, includes validation of the methodology based a variety of mechanical tests that were performed on laboratory scale specimens [78]. Here, the validity and accuracy of the methodology is verified through testing full scale nuclear graphite components.

9.2 Numerical framework

The failure prediction methodology that is implemented in this study is based on the hypothesis that once the material reaches a certain volume or size, the dissipation of energy between the microstructural elements is sufficient enough that the material shows homogeneous mechanical properties. This is achieved by a volume grouping method which defines the physical size of a link in a weakest link calculation [78]. The grouping is performed by summing volumes until a specific link volume is reached for each link in the weakest link calculation. Figure 9-1 shows the flow diagram of procedure for calculating the PoF and highlights the two grouping criteria used to determine the size of each link.

The procedure follows a grouped weakest link calculation. Stresses are calculated using a finite element (FE) model of the specimen or component under investigation. From the FE model, the stresses and associated volume are sorted from highest to lowest. The links, that are later used in a weakest link calculation, are created by summing finite element analysis (FEA) element volumes until a specific link volume, defined by two grouping criteria as highlighted in Figure 9-1, is reached. This is conducted for each link in the weakest link calculation. The two grouping criteria are defined as follows:

The first criterion is volume-based, defined as a factor (F) of the maximum grain size (Mgs) for the material under observation,

$$V_{mgs} = F.Mgs \quad (9-1)$$

The second criterion is defined by a stress limit in a group; when this limit is exceeded, a new group is started. The limit is defined as the difference between the maximum and minimum equivalent stress intensity in Weibull probability in a group [78].

$$\Delta X_i = \max(X_i) - \min(X_i) \quad (9-2)$$

Where

$$X_i = \left\{ \begin{array}{ll} \left[\frac{\sigma_i - S_0'}{S_c - S_0'} \right]^m & \sigma_i > S_0' \\ 0 & \sigma_i < S_0' \end{array} \right\} \quad (3)$$

where the equivalent stress intensity, σ_i , is defined as the maximum deformation energy (MDE) stress [57]. The Weibull parameters in equation 3 are the characteristic strength S_c , the shape parameter m and the threshold value S_0' . The weakest link volume normalised Weibull modification proposed by Schmidt [36, 37, 48, 56, 117] is then applied to each link calculated by the grouping. The

PoF of the entire component is then calculated as a product of the PoF of each link.

In Hindley *et al.* [79] the grouping criteria for the size of the link of NBG-18 are given for an accurate and conservative failure prediction and are shown in Table 9-1.

Table 9-1: Obtained link volume grouping values for NBG-18 failure prediction

<i>Use</i>	<i>Criterion One</i>	<i>Criterion Two</i>
Best accuracy values	14.45	0.99
Conservative reactor design values	9.73	0.20

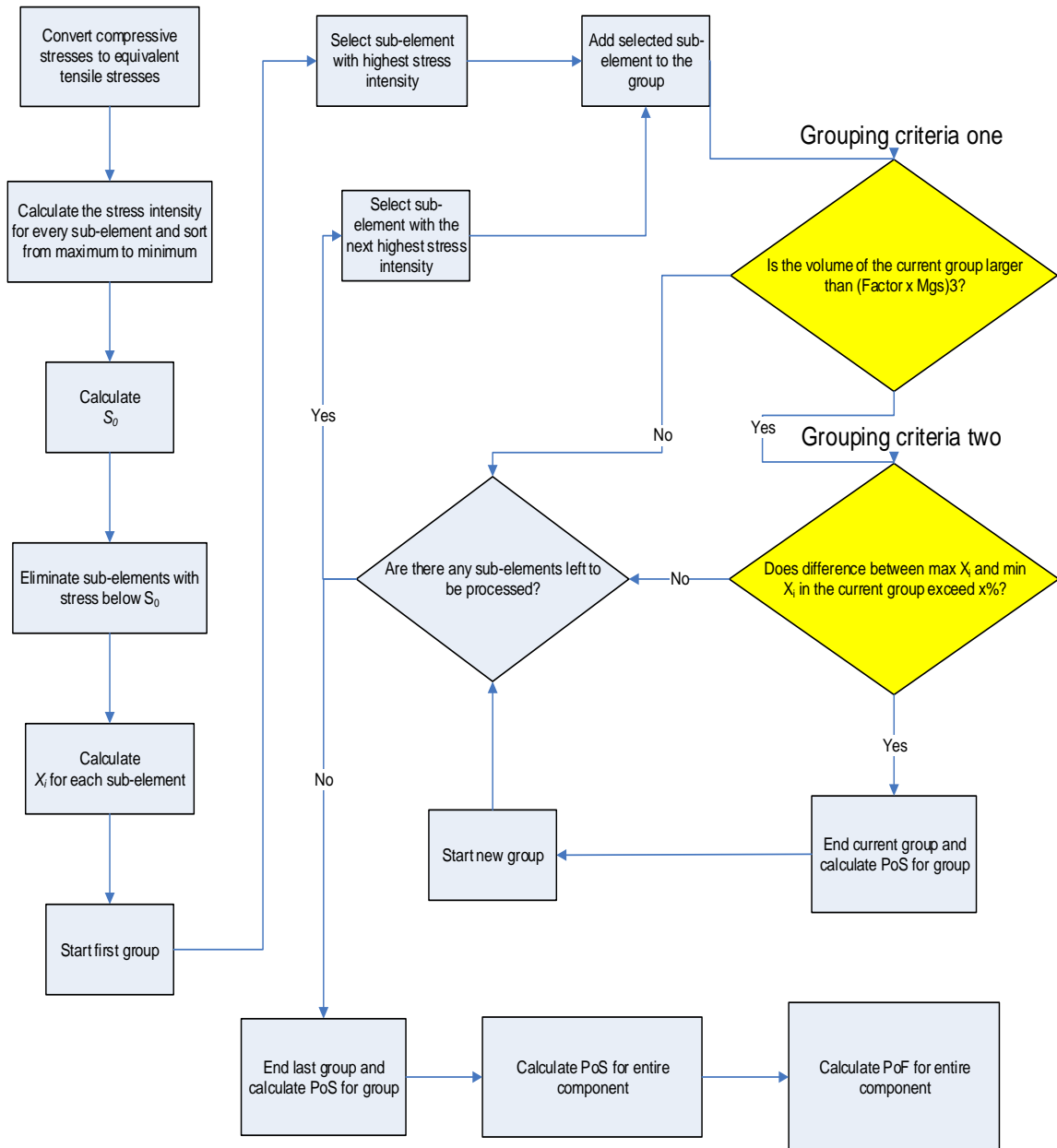


Figure 9-1: Flow diagram of failure methodology highlighting grouping criteria

The grouping criteria in Table 9-1 are obtained from 26 test cases discussed in Hindley *et al.* [78, 79]. For a methodology to be applicable to any design, it has to be able to predict failure on an independent test case as verification. For the design of reactor components, the methodology also needs to be able to predict failure on components with a far larger volume. A summary of the size of the components and the predicted error of the test cases in Hindley *et al.* [78, 79], using the best accuracy values, is given in Table 9-2.

Table 9-2: Statistical information of test cases

	<i>Maximum</i>	<i>Minimum</i>	<i>Mean</i>	<i>Std dev</i>
Volume [m ³]	6.226E-03	8.000E-06	2.853E-03	2.433E-03
Error in failure prediction %	28.70%	0.40%	8.32%	7.71%

Although the grouping criteria is optimised for 26 test cases, the statistical materials variability is calculated on only three [77]. This paper shows how the failure of a full-scale reactor component with a volume of 0.0435 m³, roughly ten times that of the test case specimens, is investigated. The test is designed to fail under similar loading condition as what is expected in a reactor during operation for this component. The investigation provides independent verification of the failure methodology while simultaneously investigating the volume dependency of the failure methodology.

It should be noted that these tests differed not only in the sizes of the specimens, but also in the manner in which the load was applied and the resultant stress distribution in the component. To aid the verification of the methodology, the structural model is implemented using the commercial software package ANSYS. In [77-79] the model was implemented using MSC Marc.

9.3 Verification experiments

9.3.1 Tensile testing

Details on the tensile tests are given in Hindley *et al.* [77, 78] and Lindeboom *et al.* [82]. The tests were performed in accordance with the international test standard (DIN 51914) on a standard tensile test sample size of Ø45•120 mm [118]. The test is designed so that the sample fails at a specific location. In the case of the tensile test specimens, the failure location is at the minimum cross-sectional area and away from the test rig clamps. The ends of the sample, where the test rig clamps the sample, do not experience stress magnitudes comparable to the material failure stress. In total, 370 tests were performed. The reliability and variance of the tests are explained in Hindley *et al.* [77].

9.3.2 Full-size specimen testing

The integrated Pebble Bed Modular Reactor (PBMR) plant design is described by Koster *et al.* [116, 119, 120] and the design of the PBMR core structures is described by Mitchell [121]. The details of thermodynamics of the PBMR core is described by Janse van Rensburg [122-125]. An irradiated analysis was performed on the various components in the central reflector and on the side reflector of the PBMR demonstration power plant 400 MW (DPP 400) core. The complexity of irradiated analysis and expected modes of failure are shown by Hindley and Erasmus [105], Erasmus *et al.* [104], and Mitchell [11]. The central reflector was found to be the life-limiting section in the reactor.

The central reflector layout of the PBMR DPP 400 design comprises various blocks, as shown in Figure 9-2. The corner block, depicted in Figure 9-3, was found to be the life-limiting block in the central reflector and thus chosen as the component for testing. During irradiated analysis, expected failure occurs when a high-tensile stress occurs in the reserve shutdown system (RSS) channel. The location of the highest stress in the RSS channel is approximately 60° off the symmetric centreline. To approximate the stress field as predicted during the irradiation, a compression force is applied inwards from the multi-purpose channels. The test rig setup for this test is shown in Figure 9-4. The test mainly creates compressive stresses throughout the structure. The surface of the RSS channel experiences a tensile stress at an angle from the middle line at the front of the block, as indicated in Figure 9-4.

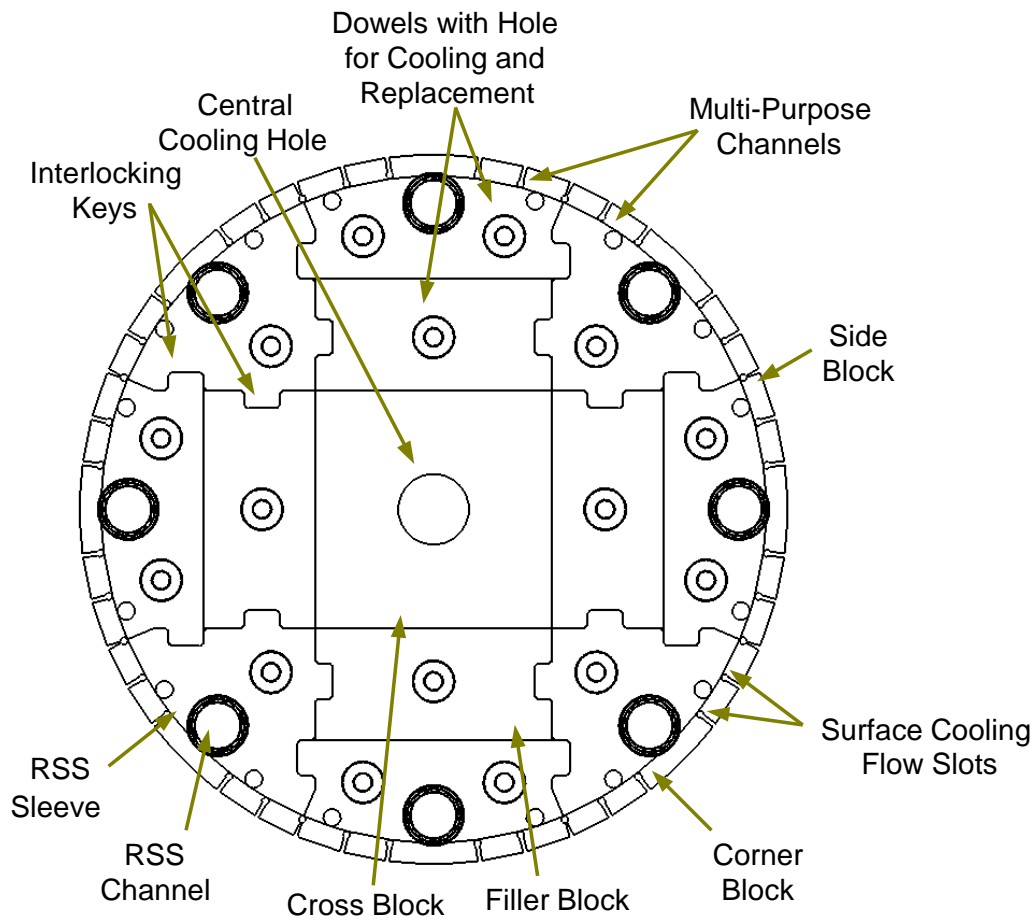


Figure 9-2: Vertical section through the upper central reflector [126]

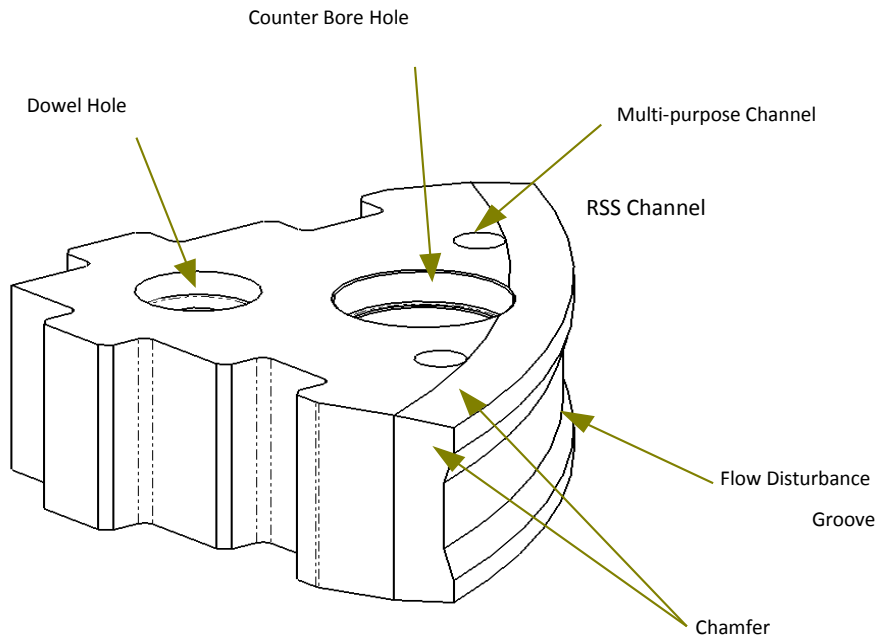


Figure 9-3: Central reflector corner block [126]

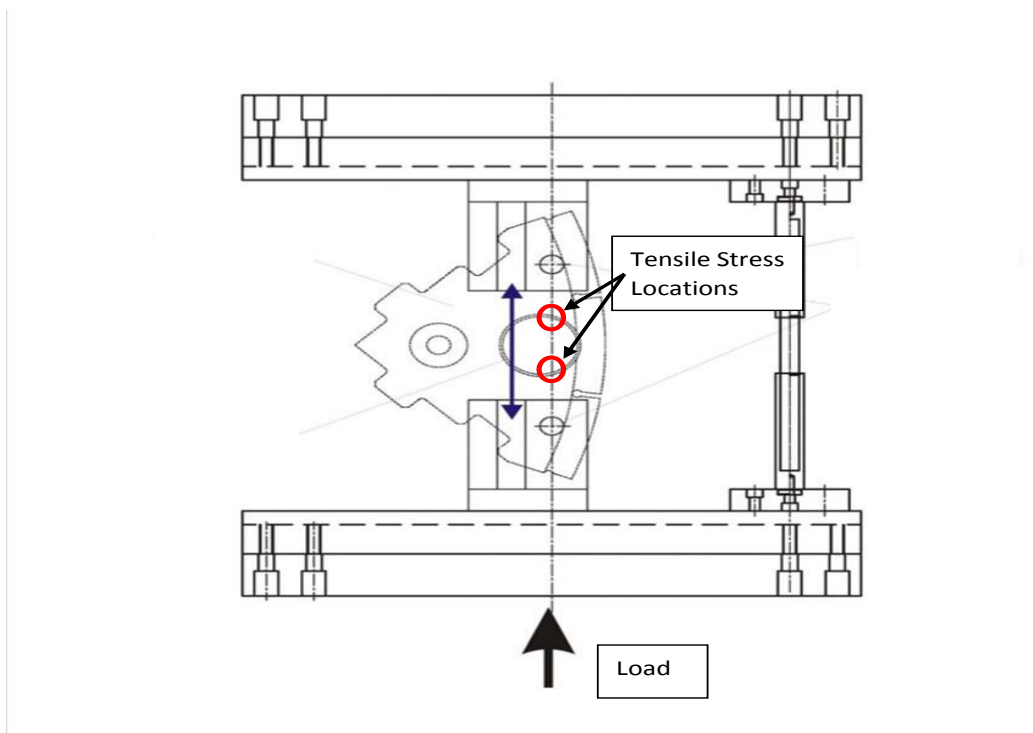


Figure 9-4: Full-size reactor component test rig setup [127]

9.3.3 Failure methodology implementation

In Hindley *et al.* [77] the statistical material strength parameters are obtained for NBG-18 nuclear graphite and used in the failure calculation which is presented here. The values are similar for tensile, bending and compressive load tests. The failure methodology presented in Hindley *et al.* [78] is used for the failure calculation. The grouping is performed using an equivalent maximum deformation energy (MDE) stress per volume of material. In Hindley *et al.* [78, 79] this is done by grouping over the integration volumes. The methodology does not take the location of each volume into consideration, but only creates links based on the stress each volume experiences. Each link contains volume with similar stress and hence a similar PoF. Subsequently, a group can consist of volumes that are not part of the same finite element (FE). However, the methodology does not stipulate which volume has to be used for a failure calculation. For the validation, the calculation presented here uses volumes with an associated stress, whereas previous papers used integration volumes of the elements in calculations. In Hindley *et al.* [79] two sets of grouping criteria are calculated for the failure methodology: one set for the reactor component design and one set for the test rig design. Both sets are used in the failure calculation presented.

9.3.4 Material properties and assumptions

FE modelling, using a linear elastic material model, is used to calculate the predicted stress distribution for both test specimens. For simplicity, an isotropic material formulation was used. This simplification is justified by the following assumptions:

- In Hindley *et al.* [77] it is shown that the statistical distribution of failure for NBG-18 is independent of the grain direction.
- There is a lack of directionally-dependent Poisson's ratio data; however, the with- and against-grain values of static Young's modulus for non-irradiated NBG-18 are very similar (less than 2% difference) [128].

The material properties used for modelling are given in Table 9-3.

Table 9-3: NBG-18 material properties used in the FE model [128]

<i>Property</i>	<i>Value</i>
Static Young's modulus (non-irradiated)	7.1×10^9 Pa
Poisson's ratio	0.2
Density	$1\ 866$ kg m ⁻³

A best estimate, namely a three-parameter Weibull data fit, from Hindley *et al.* [77] is used as input for the failure methodology. The parameters obtained and used in the failure calculations [78] are the characteristic strength (S_c), the shape parameter (m) and the threshold value (S_0). In addition to these parameters, it is also necessary to determine the ratio of compressive strength (CS) to tensile

strength (TS). The material parameters used in the failure calculation are given in Table 9-4.

Table 9-4: Material parameters used in the failure calculation

S_c (Pa)	Shape Parameter M	Compressive/Tensile Strength Ratio R	S_0 [Pa]
2.156E+07	5.780	0.264	8.250E+06

Three tests were performed on the corner blocks. The test data for the corner block are normalised to their own mean as done in Hindley *et al.* [77] and the values obtained in the statistical fit are shown in Table 9-5.

Table 9-5: Normalised statistical fit

Data Set	Normal Distribution		Weibull Distribution	
	Mean	Standard Deviation	Scale Parameter	Shape Parameter
Corner block	1.000	0.0576	1.0236	21.6740

The values obtained in Table 9-5 have a smaller standard deviation than the larger data sets used in Hindley *et al.* [77].

9.4 Results

9.4.1 Stress results

A geometric half section of the component is modelled and symmetry boundary conditions applied. The maximum principal stress distribution expected under the applied load, as predicted for the symmetric half, is shown in Figure 9-5. A geometric half section of the component is modelled and symmetry boundary conditions applied. The stress field is tensile throughout the geometry with the highest stress occurring at the surface of the RSS channel at an angle of about 60° from the middle line at the front of the block, as shown in Figure 9-5. The stress field forms a path of constant stress from close to the surface of the RSS channel to the surfaces of the cooling slots and multi-purpose channels. Additionally, the stress field forms a path of constant stress from the surface of the RSS channel towards the outer key of the block. A peak maximum principal stress also occurs on the outside reactor side of the block right in front of the RSS channel.

The minimum principal stress distribution expected under the applied load is shown in Figure 9-6. The stress field is compressive throughout the geometry, with the lowest stress (highest CS) occurring at the outer front edge of the RSS channel. A path of constant stress runs from the front of the RSS channel past the cooling channel and ends at the multi-purpose channel. Additionally, an area of high CS occurs at the back of the RSS channel.

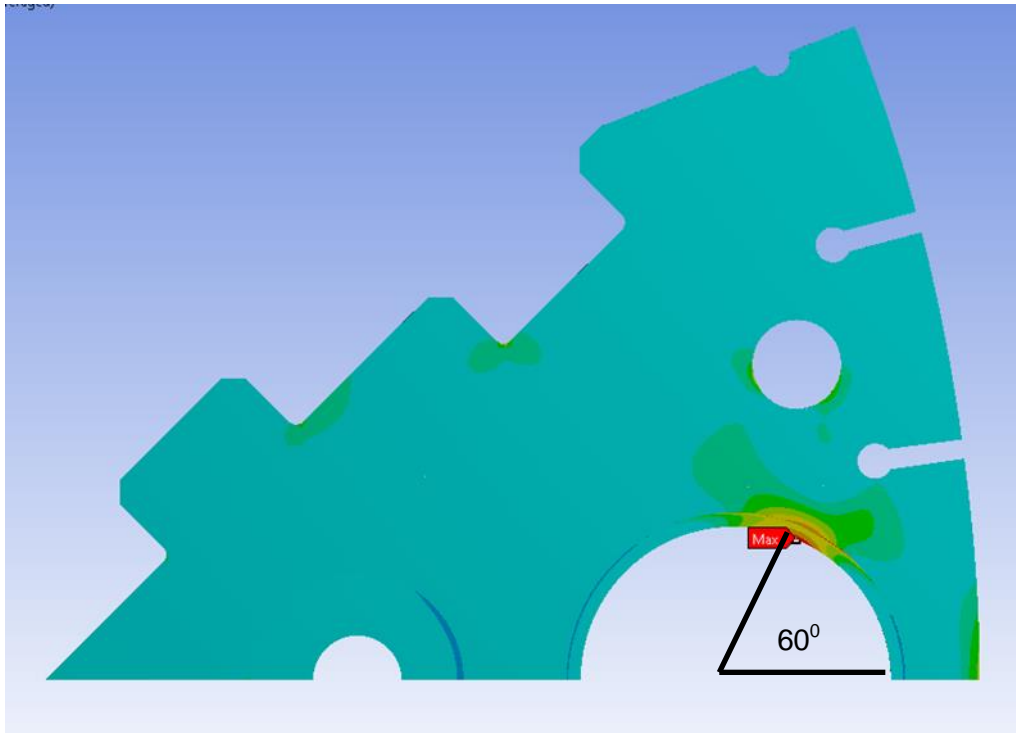


Figure 9-5: Symmetry model maximum principal stresses (TS)

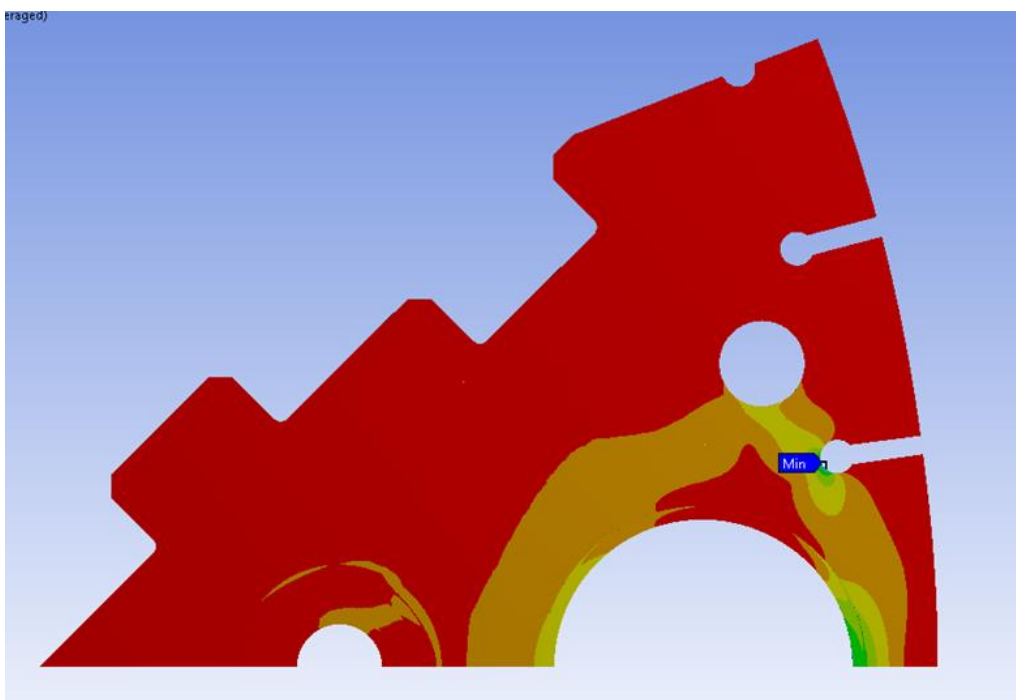


Figure 9-6: Minimum principal stresses (CS)

The two stress fields are combined into a single plot by plotting the MDE stress (equivalent stress) as described in Hindley *et al.* [78] and this is plotted in Figure 9-7. The plot in Figure 9-7 cuts off stress values below the threshold value S_0 and this is greyed out on the plot. Therefore, only the volume of material used in

the failure calculation (integration volume) is plotted with stress contours. Since the CSs are multiplied by a ratio of CS to TS, the contribution of the CS is less than the TSs. Six disconnected locations (on the symmetry model) of MDE stress that is used in failure calculation can be seen in Figure 9-7.

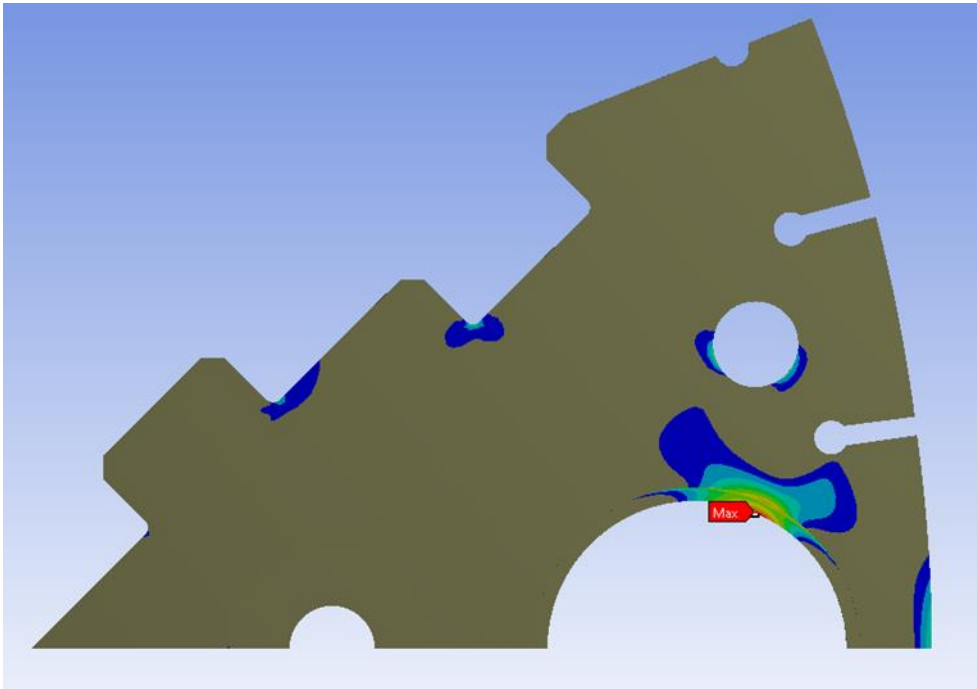


Figure 9-7: MDE stress using compression to tensile ratio

9.4.2 Failure prediction results

In previous work of Hindley *et al.* [78, 79] integration volume and the associated MDE stress were used in failure calculations. The failure methodology [81, 82] does not prescribe which volume needs to be used. Subsequently, failure calculations presented here are done using element volumes and average stress across the element. The failure calculation is done for three different mesh sizes given in Table 9-6. Only the last two meshes will be considered converged, due to stress change from initial coarse mesh. To account for the symmetry of the model in which only half the component is modelled, the volume of each element is multiplied by two. The coarse mesh delivers the most accurate prediction by forming eight groups across 271 elements. The most conservative answer is predicting a failure of 70.3% of the test failure load.

The locations of the actual failure are shown in Figure 9-8. It should be noted that the failure methodology does not take the location of stress into consideration only the stress and the volume of material at that stress (simple sorting of stresses from high to low). So for a given load, the failure methodology uses a stress distribution in the component which results in a given probability of failure for the specimen, but it does not predict the location of failure. Nevertheless, the actual failure locations do correspond to the high stress areas, as shown by comparing Figure 9-7 to Figure 9-8. The crack paths of the actual failures, shown

in Figure 9-8, correspond well with the locations of the stress field paths shown in Figure 9-5, Figure 9-6 and Figure 9-7.



Figure 9-8: Actual failure locations [127]

Since the failure methodology predicts six separate, symmetric locations of high stress in Figure 9-7, the full component is predicted to have twice the locations of high stress. Failure can be caused by crack initiation at any of these locations, even if the stress is experienced in a single location and is lower than other locations. Consequently, a failure methodology should predict a higher PoF for a component with multiple locations of high stress. By summing across all volumes to achieve the grouping for the PoF calculation, without taking the location of the volumes into account, the failure methodology automatically reduces the predicted failure load if multiple locations of high stress exist. Since the real failure initiated from a single location on the block, the predicted PoF will be conservative compared to actual failure loads. This is a conservatism which is a requirement for a design methodology to ensure a safe design in reactor components with complex stress conditions.

Table 9-7 shows the results for predicting failure for the tensile specimens and the PBMR DPP 400 corner block [77-79]. When using the conservative reactor design values, the number of links formed in the failure methodology is far larger than that for the tensile test (see Table 9-7). However, when using the test rig design values, the number of links formed is similar to the tensile test. When using the reactor design values, the failure methodology predicts a conservative mean failure load of 49.3% (load factor 0.493) of the actual test load for the corner block. When using the test rig design values, the failure methodology predicts a conservative mean failure load of 70.3% (load factor 0.703) of the actual test load for the corner block.

Table 9-6: Predicted failure loads for various meshes

<i>Maximum MDE Stress [MPa]</i>	<i>Predicted Load Scale</i>	<i>No. of Groups Formed</i>	<i>Total No. of Volumes in FEA</i>	<i>No. of Volumes Used for Failure Calculation</i>	<i>Integration Volume [m³]</i>	<i>Total Volume [m³]</i>	<i>MDE Stress Convergence</i>
25.37	78.5%	8	12 197	271	9.95E-04	4.35E-02	N/A
27.02	72.9%	7	33 408	2 142	7.61E-04	4.35E-02	6.08%
27.66	70.3%	7	314 232	27 557	7.02E-04	4.35E-02	2.31%

Table 9-7: Results for failure prediction

<i>Problem Description</i>	<i>No. of Test Specimens</i>	<i>Total Volume of Specimen [m³]</i>	<i>Integration Volume [m³]</i>	<i>Predicted Load Factor</i>	<i>No. of Links Formed</i>	<i>PoF</i>	<i>Peak MDE Stress [MPa]</i>	<i>Peak MDE Stress PoF</i>
Tensile	370	9.086e-04	2.021e-04	100	3	50%	22.24	74%
Corner block	3	4.35E-02	1.68E-03	100	7	100%	39.33	100%
Actual test (Test rig design values [79])								
Corner block (Test rig design values [79])	3	4.35E-02	7.02E-04	70.34	7	50%	27.66	100%
Corner block (Reactor design values [79])	3	4.35E-02	3.387E-04	49.3	82	50%	19.38	22%

The maximum MDE stress predicted by the FEA is also given in Table 9-7. The peak stress for each problem should be compared to the values in Table 9-4. The peak stress reported the PoF can be calculated according the three-parameter Weibull equation depicted in Equation 9-4

$$PoF = 1 - e^{-\left[\frac{\sigma - S_0}{S_c - S_0}\right]^m} \quad (9-4)$$

Where σ is the peak stress and S_c and S_0 are used as defined in Table 9-4. The peak MDE stress PoF is also given in Table 9-7. The peak MDE stress PoF is far larger than the PoF produced by the grouping methodology, except for in the case of the reactor design grouping criteria. This is part of the intent of the failure methodology which will allow a peak MDE stress above the S_c value in a small volume without penalising the total PoF by the link volume approach. However, the peak MDE stress of 39.33 MPa calculated for the actual failure load is high, even when compared to four-point bending tests [77]. Subsequently, it should be expected that the experimental mean load will reduce as more specimens are tested as experienced by large data sets in Hindley *et al.* [77].

For the reactor design grouping criteria, the peak stress is lower than the characteristic strength S_c and the threshold value S_0 is therefore adjusted according to the procedure set out in Figure 9-1.

The total volume and integration volumes of the different test specimens are reported in Table 9-7. The integration volume is the volume of material used for the failure calculation. The total volume of the corner block is two orders of magnitude larger than the volume of the tensile test specimen. The integration volume reduces as the predicted load factor decreases for the corner block form test failure load. When the load factor drops below 54.84%, the peak MDE stress becomes the same as the characteristic strength S_c value and any predicted load factors below this threshold value S_0 will scale proportionally to the characteristic strength. Subsequently, once this point is reached, the integration volume will remain the same and the maximum and minimum MDE stress in that volume will scale according to the load factor. The MDE stress for this integration volume is plotted in Figure 9-9 where only two locations (on the symmetric half model) of peak remain (at the front of the block and at the RSS channel). In Table 9-7, the integration volume for the reactor design values is a similar size as the integration volume of the tensile test. This is the constant volume of material used for failure calculation below 54% PoF. Since the grouping is based on the maximum and minimum MDE stress inside a group, the grouping in this volume will still change as the stress range changes.

9.4.3 Full range predictions

The full range prediction of failure for all points is shown in Figure 9-10. The entire range is conservative. Due to the high strength of this component it is therefore expected that the failure load that needs to be predicted will be lower than the experimental value. The predicted failure values have a constant slope

across the full range of predictions, even though the amount of locations with high stress is reduced. Figure 9-10 also shows the three parameter and two parameter Weibull distribution scaled to the mean value of the dataset for comparison.

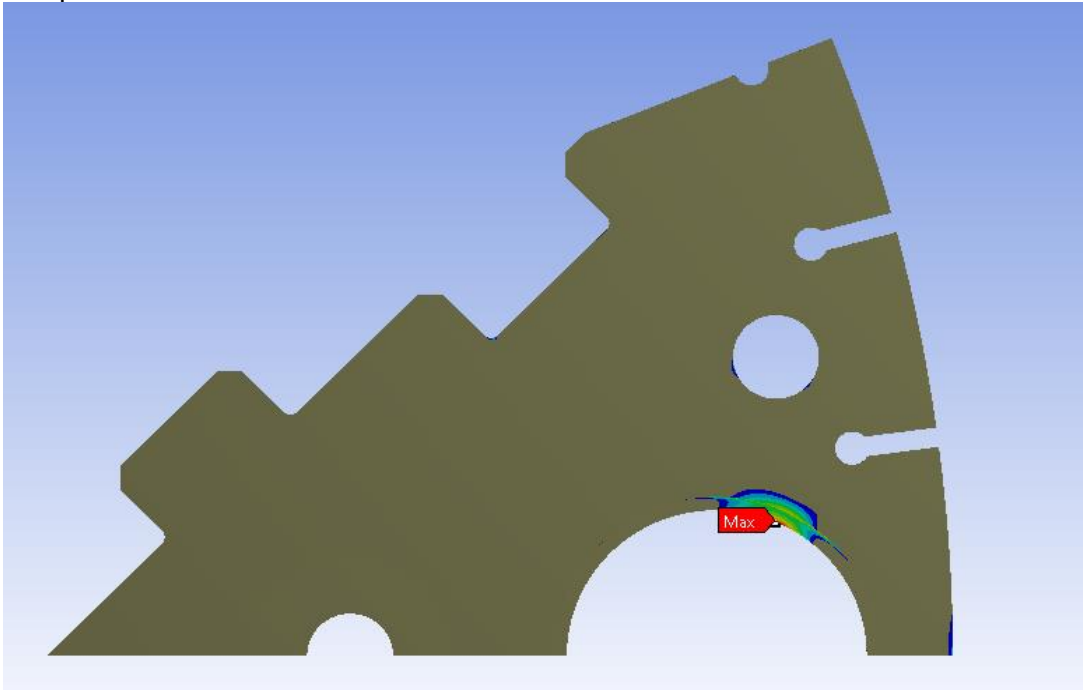


Figure 9-9: MDE stress distribution for integration volume used for failure calculation below 60.3% load factor

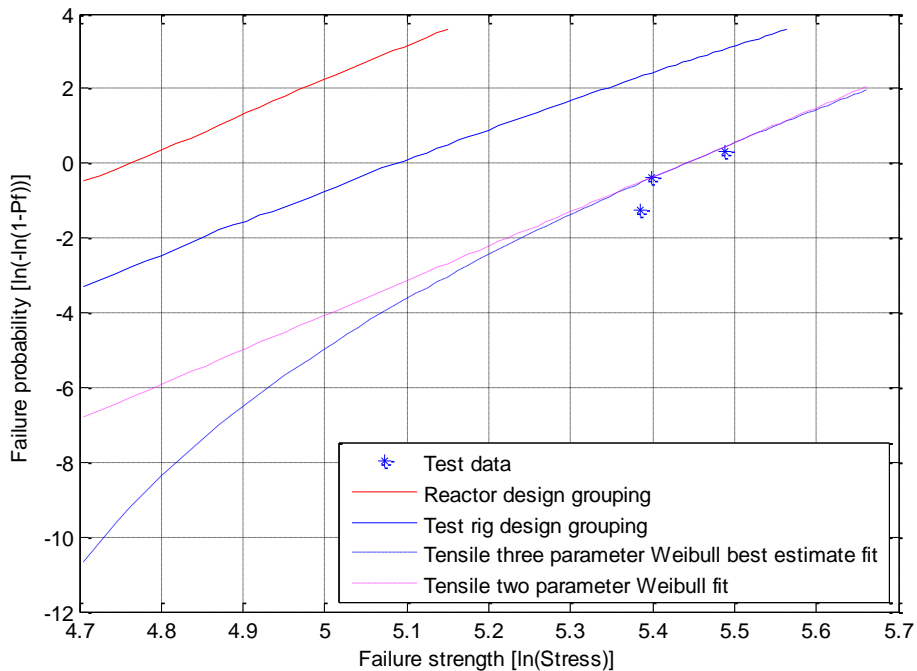


Figure 9-10: Full range prediction

9.5 Conclusion

The parameters used for failure calculation of the full-size component are obtained independently of the test being evaluated. The method presented in Hindley *et al.* [78] conservatively predicts failure for a real reactor component with a far larger volume.

Since only three tests were performed, the high strength of the full-sized component has to be questioned. Even though the actual failure was asymmetric in Figure 9-8, the failure methodology used still succeeds, i.e. is the symmetry assumption valid, introducing negligible inaccuracy.

When multiple locations of high stress exist, the PoF of the component should be higher than the PoF of any of those locations independently. Subsequently, the PoF for a component with multiple locations of stress should be higher than a component with only a single location of the same stress. The full-size corner block has multiple locations of high stress and the failure methodology forms links across all these locations independent of their physical locations. Therefore, the failure prediction methods inherently penalises the design with a conservative failure prediction due to the multiple locations of high stress. This may be a cause of over-conservatism in the failure prediction. However, the failure prediction is still done realistically within the same order of magnitude of the load applied. This serves as verification of the failure methodology.

It can be argued that predicting failure at almost half of the real load is overly conservative. However, the failure methodology allows for scaling of the size of the traditional Weibull weakest link failures [21, 70, 129], and for changes in geometry and complex loading conditions. By optimising the geometry, the life of the component can be extended conservatively by almost three times the conventional designs, as shown in Erasmus and Hindley [103]. The failure methodology enables reactor designers to conservatively predict the life of graphite core components in the reactor while allowing the geometric optimisation for life extension.

10. CONCLUDING REMARKS

This thesis is presented as a collection of four separate published papers. All the papers were drafted by the author, then reviewed and edited by the other authors, with the final version written and submitted for publication by the first author. As such, Michael Hindley, the PhD candidate, is listed as first author as he developed and managed the implementation and validation of the failure methodology. His work is presented as the hypothesis for this dissertation in Chapter 3, with the methodology, implementation and verification of the model being presented through the four published papers in Chapters 6 [77], 7 [78], 8 [79] and 9 [80]. The roles of the co-authors of the papers were as follows:

- Mark Mitchell provided technical insight and suggestions into the development of the programming framework used in the calculations [77, 78].
- Christiaan Erasmus and Ross McMurtry provided independent verification and validation to each of the FEA models used [78].
- Deborah Blaine and Albert Groenwold were the academic supervisors for the PhD candidate; as such, they provided guidance on how to present and structure the work in an academically rigorous manner, critically reviewed the drafts of the papers, and gave recommendations as to what areas needed further explanation or detail [77-80].
- Thorsten Becker is a senior lecturer in the home faculty of the PhD candidate with expert knowledge on fatigue behaviour of nuclear graphite. He was included on the academic guidance and review team after joining Stellenbosch University in 2012 and gave similar inputs to Deborah Blaine and Albert Groenwold [78-80].

In this study, failure probabilities of NBG-18 graphite parts are estimated using a numerically implemented statistical probabilistic failure methodology, as presented in Sections 6 through 9. The failure methodology is based on the assumption of a link volume (a volume of material large enough to display a homogeneous rheological response), as defined in Section 7. This is the key hypothesis for the study. The verification of the failure methodology, along with the proposed grouping criteria for the link volume, is presented in Section 7 using non-irradiated NBG-18 graphite tests.

The statistical variation of the NBG-18 graphite material properties is analysed in Section 6 [77]. The three data sets, collected from a variety of mechanical tests, demonstrate that the material fails at different mean strengths, as shown in Table 6-2. From a graphical inspection of Figure 6-1 through Figure 6-6, the existence of a bimodal distribution in the CS data is confirmed through a goodness of fit (GOF) test in section 6.4. The data sets are combined into one large data set which passes the GOF test for a Weibull distribution and this indicates that the mechanisms of failure between the three data sets are similar. Since the

standard deviation in the CS data set is less than other data sets, it does not have an influence on the combined data fit and the bi-modal distribution can be neglected. The success at fitting the Weibull distribution through the combined normalised data sets allows us to improve the basis for the estimates of the variability. This could imply that the variability on the graphite strength for the different strengths is based on the same flaw distribution and is thus a property of the material. This observation is attributed to the use of a large and representative data set.

The values obtained in the statistical analysis are used in the failure methodology. The mathematical implementation of the methodology is given in Section 7 [78], and the source code in Appendix D. The experimental tests contain specimens of a different geometry, loading conditions and sizes, and with and without stress-concentrating features. The most accurate predictions were made for specimens experiencing a uni-axial, or approximately uni-axial, stress state. Predictions for problems with stress-concentrating features and multi-axial stress states were less accurate. The majority of median failure load predictions fell within the acceptable range (determined by the variation of billet-to-billet failure strengths). Predictions were also compared with experiments across the range of failure probabilities for which experimental data were available (Appendix C). Generally, predictions were either accurate or conservative over the range of failure probabilities for all the data points available. The method showed little mesh sensitivity when dealing with a converged finite element analysis (FEA) mesh solution. The method showed consistent usability throughout all test cases.

Section 8 [79] evaluates the grouping criteria, proposed in Section 7 [78] to form the numerical link volume. A methodology for calculating a more appropriate link volume, using mathematical optimisation, is shown. As a result, two sets of criteria are identified for NBG-18 nuclear grade graphite: The first, the less conservative method proposed by the optimisation presented in Section 8, is appropriate when implemented in the design of an experimental set-up for NBG-18. This grouping criterion allows for over prediction of failure loads and is the most accurate. The second set of grouping criteria, as presented by the theoretical assumptions proposed in Section 7, ensures conservatism for the design of full-size reactor components.

The failure methodology presented in this study is developed with specific application to the NBG-18 grade of nuclear graphite, in the non-irradiated state. Applicable to other grades of graphite, or to the irradiated NBG-18 graphite, has not been evaluated and any extension of the parameters would be highly speculative. A full study would be required to confirm the applicability of this methodology to other materials. It is recommended that tests, designed to validate the applicability of this methodology to other materials, should focus on stress concentrating features and uniform stress fields. It would be useful to compare the link volume size found for different grades of graphite to the values found for NBG-18 graphite in this study.

In Section 9, Hindley *et al.* [80], validates the failure methodology by evaluating a full-size specimen, special, structural test which was developed to simulate the same failure condition expected during the normal operation of the reactor.

Failure of the full-size component is predicted realistically, but conservatively. Thus, real reactor components can be designed safely using data obtained from standard tensile testing data. The stress results in this section are obtained using an alternate FEA package than that used in previous sections.

The failure methodology presented conservatively predicts failure for a real reactor component with a far larger volume than a tensile test specimen. It may be argued that predicting failure at almost half of the real load is overly conservative. However, the failure methodology presented allows for scaling of the size and allows for changes in geometry with complex loading conditions. By optimising the geometry, the life of the component can be extended conservatively by almost three times the conventional designs, as shown in Appendix A [103, 130]. The failure methodology enables reactor designers to conservatively predict the life of graphite core components in the reactor while allowing the geometric optimisation for life extension. Furthermore, the methodology allows designers to assess the influence of geometric changes without the need to perform tests on each proposed geometry. This approach is conservative, accounting for the existence of disparate flaws in the material.

NBG-18 is very near to an isotropic material. To expand the methodology for transversely isotropic graphite, the maximum deformation energy (MDE) stress formulation in Section 2.6 needs to be reevaluated.

The method presented here has a simple implementation, due to only sorting the FEA stresses and associated volume. This does not take the physical location of each sub-element into consideration when forming groups for link volumes. This will penalise the design of reactor components with multiple stress-concentrating features by being more conservative. However, if a higher accuracy in the prediction is required, a formulation with a direct linking method is expected to deliver better predictions. This will require further work on the method presented.

11. DISCUSSION OF PUBLISHED WORK

Following the publication of Sections 7 and 8, the validity of the initial grouping criteria proposed in Section 7, as compared to the optimised grouping criteria found in Section 8, has been questioned. A short discussion of the applicability and validity of these two grouping criteria follows.

Initially, the failure methodology was developed with the grouping criteria as given in Section 7.3.4.4. for nuclear graphite in general. These criteria were based on expert recommendations as indicated in [78]. Thereafter, the grouping criteria were validated, and then optimised specifically for non-irradiated NBG-18 nuclear graphite, as presented in Section 8. The first grouping criterion, limitation of the link volume to a minimum size of 10 Mgs, is shown to be applicable to both the initial and optimised versions of the failure methodology. The second criteria, however, finds a different value for allowable difference in equivalent stress between the initial and optimised versions. For reactor design values, the more conservative criterion of 7% difference proposed in Section 7, is appropriate, while the optimised value, presented in Section 8, is 20%. To illustrate the difference the second grouping criterion has on failure prediction, the predicted load factor results are compared in Table 11-1. Since this is an approximate solution, the results shown in Table 11-1 are similar for most of the test cases evaluated. Test case 22 is the only one that shows significant difference between the two proposed values for grouping criterion 2. The reason for this difference is that Test case 22 contains a large volume of material at a high stress; this results in a larger value for criterion 2 when implementing the optimised, penalty solution and far fewer “links” are formed in this formulation.

Table 11-1: Comparison between Initial grouping criteria and optimal reactor design values

Test case number	<i>Initial grouping</i>		<i>Oprimisation penalised grouping</i>	
	Predicted load factor [%]	Number of groups formed	Predicted load factor	Number of groups formed
1	100.2	7	99.4	7
2	100.2	9	99.4	9
3	92.1	4	91.3	4
4	99	1	99	1
5	93.1	1	93.1	1
6	86.4	14	85.5	15
7	93.5	18	92.7	19
8	90.7	18	89.9	20
9	93.1	19	92.3	20
10	72.9	8	72.1	9
11	81	10	80.3	11
12	81.8	10	81.1	11

13	81.1	9	80.5	9
14	88.4	6	87.6	6
15	89.2	6	88.5	6
16	87.5	6	86.8	6
17	86.7	6	85.9	6
18	71.3	1	71.3	1
19	85.6	2	84.7	2
20	86.6	3	85.8	3
21	84	3	83.3	4
22	76.5	96	87.9	51
23	101	5	100	5
24	89.9	4	89.1	4
25	67.2	34	68.2	35
26	50.1	53	51.6	49

A more detailed explanation of the method employed in obtaining the three parameter Weibull fit is presented here for further clarity in implementation of the model. MATLAB does not provide a function to calculate a three parameter Weibull fit, as given in Table 7-1. To calculate the third parameter, S_0 , the Matlab two parameter Weibull fitting algorithm is used to fit the data for a specific S_0 value. S_0 is then varied between the zero and the minimum failure point observed, with appropriate determination of the two parameter Weibull fit for each S_0 value. The RMS error is calculated between each fit and the actual test data. The S_0 value, which results in the smallest RMS error, is subsequently assigned as the best three parameter Weibull fit.

12. REFERENCES

1. Lovelock, J. *Nuclear Power is the Only Green Solution*. The Independent 2004 [cited 2011 4 June]; Available from: <http://www.independent.co.uk/voices/commentators/james-lovelock-nuclear-power-is-the-only-green-solution-6169341.html>.
2. Reutler, H. and Lohnert, G.H., *Advantages of Going Modular in HTRs*. Nuclear Engineering and Design, 1984: p. 129.
3. Nabilek, H., *et al.*, *Fuel for Pebble-Bed HTRs*. Nuclear Engineering and Design, 1984. 78(2): p. 155-166.
4. Walmsley, J., *High-Temperature Gas Cooled Reactor Historical Aspects*. Nuclear Safety Division, 1995 (NSD R95/07).
5. Ide, A., *et al.*, *Study of a High-Temperature Gas Cooled Reactor Heat Utilisation Plant*, in *HTR Heat Utilisation Core Group*. Japan.
6. Zuying, G. and Lei, S., *Thermal Hydraulic Transient Analysis of the HTR-10*. China, Nuclear Engineering and Design 2002. 218: p. 65-80.
7. Slabber, J., *Technical Description of the PBMR Demonstration Power Plant*, in *PBMR (Pty) Ltd. Proprietary Document*. 2006.
8. IAEA. *HTGR Knowledge Base Topical Article 5: Graphite Material Technology*. 2003-2004 [cited 2010 24 February]; Available from: http://www.iaea.org/inis/nkm/nkm/aws/htgr/topics/article_05.html.
9. Davies, M.A., *Graphite Moderator Lifecycle Behaviour*, in *Proceedings of Graphite Specialist's Meeting on Graphite Moderator*. 1996, IAEA-Techdoc-901: Bath (United Kingdom).
10. Marsden, B.J., *Nuclear Graphite for High-Temperature Reactors*, in *Gas Turbine Power Conversion Systems for Modular HTGRs*. 2000, IAEA Technical Committee Meeting: Palo Alto, California. p. 174-189.
11. Mitchell, M.N., *Identification of the Key Parameters Defining the Life of Graphite Core Component*, in *18th International Conference on Structural Mechanics in Reactor Technology (SMiRT 18)*. 2005: Beijing, China.
12. Smith, M.C., *Deformation and Fracture Mechanisms in Polycrystalline Graphites*. 1972, Los Alamos Scientific Lab., N. Mex.
13. Burchell, T.D., *Carbon Materials for Advanced Technologies*. 1999: Elsevier Science Ltd.
14. Pierson, H.O., *Handbook of Carbon, Graphite, Diamond and Fullerenes: Properties, Processing and Applications*. 1993: William Andrew Publishing.
15. Nemeth, N.N. and Bratton, R.L., *Statistical Models of Fracture Relevant to Nuclear-Grade Graphite: Review and Recommendations*. Nuclear Engineering and Design, 2011. 140(1): p. 1-29.
16. Nightingale, R.E., *Nuclear Graphite*. 1969, Battelle-Northwest, Richland, Wash. Pacific Northwest Lab.
17. Wen, K.Y., Marrow, T.J., and Marsden, B.J., *The Microstructure of Nuclear Graphite Binders*. Carbon, 2008. 46(1): p. 62-71.
18. Tucker, M.O., Rose, A.P.G., and Burchell, T.D., *The Fracture of Polygranular Graphites*. Carbon, 1986. 24(5): p. 581-602.
19. Price, R.J. and Beavan, L.A., *Strength of Nonuniformly Oxidised PGX Graphite*. 1981. p. 39.

20. Roberts, J.G., *NBG-18 Graphite Fatigue Characteristics*, in *Mechanical Engineering*. 2008, North West University: Potchefstroom. p. 102.
21. Bazant, Z.P. and Xi, Y., *Statistical Size Effect in Quasi-Brittle Structures: II. Nonlocal Theory*. *Journal of Engineering Mechanics*, 1991. 117(11): p. 2 623-2 640.
22. Brocklehurst, J.E. and Darby, M.I., *Concerning the Fracture of Graphite Under Different Test Conditions*. *Materials Science and Engineering*, 1974. 16(1-2): p. 91-106.
23. Ho, F.H., Vollman, R.E., and Cull, A.D., *Fracture Mechanics of PGX Graphite*. 1981, General Atomic Co., San Diego, CA (USA); Southern Research Inst., Birmingham, AL (USA). p. 40.
24. Ho, F.H., *Modified Weibull Theory for the Strength of Granular Brittle Material*, G.A. Co., Editor. 1979: San Diego, CA (USA). p. 27.
25. Judge, R.C.B., *A Method for Assessing the Effects of Graphite Property Variability on Core Structural Integrity Criteria*, in *Specialist's Meeting on the Status of Graphite Development for Gas Cooled Reactors*. 1991, International Atomic Energy Agency, Vienna (Austria): Tokai, Ibaraki (Japan). p. 78-84.
26. Kennedy, C.R. and Eatherly, W.P., *Statistical Characterisation of Tensile Strengths for a Nuclear-Type Core Graphite*, in *IWGGCR*. 1986. p. 63-68.
27. Nemeth, N., et al., *Large-Scale Weibull Analysis of H-451 Nuclear-Grade Graphite Rupture Strength*. *Carbon*, 2013. 58: p. 208-225.
28. Price, R.J., *Statistical Study of the Strength of Near-Isotropic Graphite*. 1976, General Atomic Co., San Diego, CA, USA. p. 161.
29. Schmidt, A., *Problems Connected to the Application of the Weibull Theory to the Results of a Finite Element Calculation*, M. Hindley, Editor. 2007, Westinghouse Reaktor GmbH: PBMR.
30. Strizak, J.P., *The Effect of Volume on the Tensile Strength of Several Nuclear-Grade Graphites*, in *Specialist's Meeting on The Present Status of Graphite Development for Gas Cooled Reactors*. 1991, IAEA: JAERI Tokai, Japan. p. 16.
31. Cords, H., Kleist, G., and Zimmermann, R., *A Statistical Fracture Criterion for Graphite*, in *Specialist's Meeting on Mechanical Behaviour of Graphite for HTRs. International Working Group on High-Temperature Reactors*. 1979, IAEA: Gif-sur-Yvette, France. p. 110-115.
32. Srinivasan, M., *On Estimating the Fracture Probability of Nuclear Graphite Components*. *Journal of Nuclear Materials* 2008. 381(1-2): p. 185-198.
33. Yu, S., et al., *Probability Assessment of Graphite Brick in the HTR-10*. *Nuclear Engineering and Design*, 2004. 227(2): p. 133-142.
34. Mitchell, B.C., *The Understanding and Development of Nuclear Graphite Technology*. 2003, Univesity of Manchester.
35. Mitchell, B.C., et al., *The Mechanical Testing of Nuclear Graphite*. *Journal of Nuclear Materials*, 2003. 322(2-3): p. 126-137.
36. Schmidt, A., *Reliability Analysis of Graphite Structures. Part II: Theoretical and Experimental Investigations*. 2000, Westinghouse Reactor GmbH.
37. Schmidt, A., *Reliability Analysis of Graphite Structures Part I: Theory*, in *Part I: Theory*. 2000, Westinghouse Reaktor GmbH: Project 910PMRB08.
38. Schmidt, A., *Design of Steel and Graphite Structures - A Comparison*. 2004, PBMR.

39. Batdorf, S.B. and Crose, J.G., *A Statistical Theory for the Fracture of Brittle Structures Subjected to Nonuniform Poly-Axial Stresses*. Journal of Applied Mechanics, 1974. 41: p. 459.
40. Batdorf, S.B. and Heinisch Jr, H.L., *Weakest Link Theory Reformulated for Arbitrary Fracture Criterion*. Journal of the American Ceramic Society, 1978. 61(7-8): p. 355-358.
41. Becker, T.H., *Understanding and Modelling Damage and Fracture in Nuclear Grade Graphite*, in University of Cape Town. 2011.
42. Becker, T.H., Marrow, T.J., and Tait, R.B., *Damage, Crack Growth and Fracture Characteristics of Nuclear Grade Graphite Using the Double Torsion Technique*. Journal of Nuclear Materials, 2011. 414(1): p. 32-43.
43. Becker, T.H., et al., *An Approach to Calculate the J-Integral by Digital Image Correlation Displacement Field Measurement*. Fatigue and Fracture of Engineering Materials and Structures, 2012.
44. Burchell, T.D., *A Microstructurally Based Fracture Model for Polygranular Graphites*. Carbon, 1996. 34(3): p. 297-316.
45. Burchell, T.D. and Strizak, J.P., *Nuclear Graphite Strength, Disparate Flaws and Fracture Modelling*. Submitted Journal of Nuclear Materials, 2010. JNM-D-10-00256.
46. Kennedy, C.R. and Kehne, M.T., *Fracture Toughness of Anisotropic Graphites*, in 17. Biennial Conference on Carbon, Lexington, KY, USA, 16 Jun 1985. 16 Jun 1985, Oak Ridge National Lab., TN (USA): Lexington, KY, USA.
47. Price, R.J., *Strength of Irradiated Graphite: A Review*. 1979. p. 15.
48. Schmidt, A., *Fracture Behaviour of Graphite*. 2000, Westinghouse Reaktor GmbH: Project 910PMRB08.
49. Wang, J.A.J. and Liu, K.C., *An Innovative Technique for Evaluating Fracture Toughness of Graphite Materials*. Journal of Nuclear Materials, 2008. 381(1-2): p. 177-184.
50. Xiong, J.J. and Shenoi, R.A., *Fatigue and Fracture Reliability Engineering*. 2011: Springer Verlag.
51. Becker, T.H., Marrow, T.J., and Tait, R.B., *An Evaluation of the Double Torsion Technique*. Experimental Mechanics, 2011. 51(9): p. 1 511-1 526.
52. Sakai, M., Urashima, K., and Inagaki, M., *Energy Principle of Elastic-Plastic Fracture and Its Application to the Fracture Mechanics of a Polycrystalline Graphite*. Journal of the American Ceramic Society, 1983. 66(12): p. 868-874.
53. Fung, Y., *Foundations of Solid Mechanics*. 1965: Prentice Hall.
54. da Silva, V.D., *Mechanics and Strength of Materials*. 2006: Springer Verlag.
55. Prager, W. and Drucker, D., *Soil Mechanics and Plastic Analysis or Limit design*. Appi. Math, 1952. 10(2): p. 157-165.
56. Schmidt, A., *Multi-Axial Stress States in Graphite*. 2000, Westinghouse Reaktor GmbH: Project 910PMRB08.
57. Schubert, F., Nickel, H., and Breitbach, G., *Structural Design Criteria for HTR*. Nuclear Engineering and Design, 1991. 132(1): p. 75-84.
58. Tucker, M.O. and McLachlan, N., *Fracture and Microstructure of Graphites*. Journal of Physics D: Applied Physics, 1993. 26: p. 893.

59. Evans, A.G., *Structural Reliability: A Processing-Dependent Phenomenon*. Journal of the American Ceramic Society, 1982. 65(3): p. 127-137.
60. Davidge, R.W., *Mechanical Behaviour of Ceramics*. 1979: Cambridge University Press.
61. Munz, D. and Fett, T., *Ceramics: Mechanical Properties, Failure Behaviour, Materials Selection*. 1999: Springer Verlag.
62. Wachtman, J.B., Cannon, W.R., and Matthewson, M.J., *Mechanical Properties of Ceramics*. 2009: John Wiley & Sons Inc.
63. Danzer, R., *Mechanical Performance and Lifetime Prediction*. Concise Encyclopedia of Advanced Ceramic Materials, 1991: p. 286-329.
64. Abernethy, R.B., *The New Weibull Handbook*, in Gulf Publication. 1996.
65. Danzer, R., et al., *Fracture Statistics of Ceramics - Weibull Statistics and Deviations from Weibull Statistics*. Engineering Fracture Mechanics, 2007. 74(18): p. 2 919-2 932.
66. Weibull, W., *A Statistical Distribution Function of Wide Applicability*. ASME Journal of Applied Mechanics, 1951. 18: p. 293-297.
67. Peirce, F.T., *Tensile Tests for Cotton Yarns, Part V: "The Weakest Link" Theorems on the Strength of Long and of Composite Specimens*. J. Textile Inst, 1926. 17: p. T355-368.
68. Tippett, L.H.C., *On the Extreme Individuals and the Range of Samples Taken from a Normal Population*. Biometrika, 1925. 17(3-4): p. 364.
69. Strizak, J.P., *The Effect of Volume on the Tensile Strength of Several Nuclear-Grade Graphites*. IAEA-TECDOC-690, 1991.
70. Xi, Y. and Reid, S.G., *Statistical Size Effect in Quasi-Brittle Structures: I. Is Weibull Theory Applicable?* Journal of Engineering Mechanics, 1991. 117: p. 2 609.
71. Weibull, W., *A Statistical Theory of the Strength of Materials*. Royal Swedish Institute for Engineering Research, 1939. 151(Stockholm).
72. Buch, J.D., *Mechanical Behaviour Model for Graphites Properties Related to Fracture Toughness*. ASTM STP, 1976. 605: p. 124-44.
73. Barnett, R.L., et al., *Fracture of Brittle Materials under Transient Mechanical and Thermal Loading*. Iit Research Inst Chicago, I.L. 1967: Air Force Flight Dynamics Laboratory, Research and Technology Division, Air Force Systems Command.
74. Yoon, J.H., et al., *Characterisation of Tensile Strength and Fracture Toughness of Nuclear Graphite NBG-18 using Subsize Specimens*. Journal of Nuclear Materials, 2011. 412(3): p. 315-320.
75. KTA, *KTA-3232 Keramische Einbauten in HTR-Reactordruckbeh, Iten, Sicherheitstechnische Regel des KTA*. Vol. KTA-3232. 1992.
76. ASME, *ASME Boiler and Pressure Vessel Code in ASME III Division 5 High-Temperature Reactors*. 2010, ASME.
77. Hindley, M.P., et al., *Observations in the Statistical Analysis of NBG-18 Nuclear Graphite Strength Tests* Journal of Nuclear Materials 2012. 420(1-3): p. 110-115.
78. Hindley, M.P., et al., *A Numerical Stress Based Approach for Predicting Failure in NBG-18 Nuclear Graphite Components with Verification Problems*. Journal of Nuclear Materials, 2013. 436(1-3): p. 175-184.

79. Hindley, M.P., *et al.*, *Optimisation of the Link Volume for Weakest Link Failure Prediction in NBG-18 Nuclear Graphite* Nuclear Engineering and Design, 2014. 274: p. 10-19.
80. Hindley, M.P., *et al.*, *Failure Prediction of Full-Size Reactor Components from Tensile Specimen Data on NBG-18 Nuclear Graphite*. Nuclear Engineering and Design, 2014. 284: p. 1-9.
81. Mitchell, M.N., *Requirements for the Design and Manufacture of the Ceramic Internals of the PBMR*. 2009, PBMR Clasified Internal Document.
82. Lindeboom, J., *et al.* *Overview of CSC Testing in Support of DPP Completion*. in *INGSM9*. 2008. Egmond aan Zee.
83. Pal, N., Jin, C., and Lim, W.K., eds. *Handbook of Exponential and Related Distributions for Engineers and Scientists*. 2006, Chapman & Hall/CRC.
84. Anderson, T.W. and Darling, D.A., *Asymptotic Theory of Certain "Goodness Of Fit" Criteria Based on Stochastic Processes*. Annals of Mathematical Statistics, 1952. 23: p. 193-212.
85. Stephens, M.A., *Tests of Fit for the Logistic Distribution Based on the Empirical Distribution Function*. Biometrika, 1979. 66: p. 591-595.
86. Stephens, M.A., *Goodness of Fit for the Extreme Value Distribution*. Biometrika, 1977. 64: p. 583-588.
87. Stephens, M.A., *EDF Statistics for Goodness of Fit and Some Comparisons*. Journal of the American Statistical Association, 1974. 69: p. 730-737.
88. Stephens, M.A., *Asymptotic Results for Goodness-of-Fit Statistics with Unknown Parameters*. Annals of Statistics, 1976. 4: p. 357-369.
89. Stephens, M.A., *Goodness of Fit with Special Reference to Tests for Exponentiality*. 1977, Stanford University.
90. Trujillo-Ortiz, A.R., *et al.* *Anderson-Darling Test for Assessing Weibull Distribution of a Sample Data. A MATLAB file*. 2007 [cited 2010 1 June]; Available from: <http://www.mathworks.com/matlabcentral/fileexchange/loadFile.do?objectId=15745>.
91. Trujillo-Ortiz, A.R., *et al.* *Anderson-Darling Test for Assessing Normality of a Sample Data. A MATLAB file*. 2007 [cited 2010 1 June]; Available from: <http://www.mathworks.com/matlabcentral/fileexchange/loadFile.do?objectId=14807>.
92. Nemeth, N.N., *et al.* *Pooled Weibull Analysis of Legacy H-451 Garphite Specimen Rupture Data*. in *INGSM10*. 2009. West Yellowstone Montana USA.
93. Erasmus, C., *VP01: Graphite Bending Test*, in *PBMR (Pty) Ltd. Proprietary Document*. 2009, PBMR.
94. Mitchell, M.N. *Criteria for Graphite Core Components (GCC) - ASME Nuclear Codes and Standards*. in *9th International Graphite Specialist's Meeting*. 2009. Egmond am Zee.
95. MSC, *Marc Analysis Research Corporation-Europe Advanced Marc Analysys Aplying User Subroutines*. 2002.
96. Mcurtry, R., *VP-00: Tensile Strength*, in *PBMR (Pty) Ltd. Proprietary Document*. 2009, PBMR.
97. Tahon, B., *Material Qualification Report, NBG-18 Graphite*, in *PBMR (Pty) Ltd. Proprietary Document*. 2009, SGL Carbon Group.

98. Mcmurtry, R., *VP-19: Compressive Strength*, in *PBMR (Pty) Ltd. Proprietary Document*. 2009, PBMR.
99. Mcmurtry, R., *VP-12: AN-18 Beams With Stress Concentrating Geometric Features*, in *PBMR (Pty) Ltd. Proprietary Document*. 2009, PBMR.
100. Baumann, S., *Test Report, Fillet Radii Test*, in *PBMR (Pty) Ltd. Proprietary Document*. 2009, SGL Carbon Group.
101. Mcmurtry, R., *VP-15: PBMR AN-48 Sleeve Burst Test*, in *PBMR (Pty) Ltd. Proprietary Document*. 2009, PBMR.
102. Rosen, K., *Test Report: AN-48 Sleeve Burst Test*, in *PBMR (Pty) Ltd. Proprietary Document*. 2009, SGL Carbon Group.
103. Erasmus, C. and Hindley, M.P., *Geometric Layout Optimisation of Graphite Reflector Components*, in *The 5th High-Temperature Reactor Technology Conference*. 2010: Prague, Czech Republic.
104. Erasmus, C., Kok, S., and Hindley, M.P., *Significance of Primary Irradiation Creep in Graphite*. *Journal of Nuclear Materials*, 2013. 436(1): p. 167-174.
105. Hindley, M.P. and Erasmus, C. *PBMR Graphite Reflector Structural Integrity Probabilistic Assessment*. in *Proceedings for the 7th South African Conference on Computational and Applied Mechanics (SACAM10)*. 2010. University of Pretoria.
106. Wu, Z., Lin, D., and Zhong, D., *The Design Features of the HTR-10*. *Nuclear Engineering and Design*, 2002. 218(1): p. 25-32.
107. Shih, C., Katoh, Y., and Takashi, T., *Effects of Size and Geometry on the Equibi-Axial Flexural Test of Fine Grained Nuclear Graphite*. *Ceramic Materials for Energy Applications III*, 2014: p. 141-148.
108. Nocedal, J. and Wright, S.J., *Numerical Optimisation*. 1999: Springer verlag.
109. Snyman, J.A., *Practical Mathematical Optimisation: An Introduction to Basic Optimisation Theory and Classical and New Gradient-Based Algorithms*. Vol. 97. 2005: Springer Verlag.
110. Snyman, J.A., *A New and Dynamic Method for Unconstrained Minimisation*. *Applied Mathematical Modelling*, 1982. 6(6): p. 449-462.
111. Snyman, J.A., *An Improved Version of the Original Leap-Frog Dynamic Method for Unconstrained Minimisation: LFOP1 (b)*. *Applied Mathematical Modelling*, 1983. 7(3): p. 216-218.
112. Snyman, J.A., *The LFOPC Leap-Frog Algorithm for Constrained Optimisation*. *Computers and Mathematics with Applications*, 2000. 40(8-9): p. 1 085-1 096.
113. Bazant, Z.P., *Size Effect in Blunt Fracture: Concrete, Rock, Metal*. *Journal of Engineering Mechanics*, 1984. 110(4): p. 518-535.
114. McMeeking, R.M. and Evans, A.G., *Mechanics of Transformation-Toughening in Brittle Materials*. *Journal of the American Ceramic Society*, 1982. 65(5): p. 242-246.
115. Bazant, Z.P. and Planas, J., *Fracture and Size Effect in Concrete and Other Quasi-Brittle Materials*. Vol. 16. 1997: CRC Press.
116. Koster, A., Matzer, D., and Nicholls, D.N., *PBMR: A Generation IV High-Temperature Gas Cooled Reactor*. Unknown, 2003.
117. Schmidt, A., *Reliability Analysis of Graphite Structures*, in *Part II: Theoretical and Experimental Investigations*. 2000, Westinghouse Reaktor GmbH: Project 910PMRB08.

118. Tahon, B., *CSC Material Qualification Report NBG-18 Graphite*, in *PBMR (Pty) Ltd. Proprietary Document*. 2008, SGL Carbon Group.
119. Koster, A., Matzer, D., and Nicholls, D.N., *PBMR Design for the Future*. Nuclear Engineering and Design, 2003. 2 800: p. 1-15.
120. Venter, P.J., Mitchell, M.N., and Fortier, F., *PBMR Reactor Design and Development*. Proceedings of the 18th International Conference on Structural Mechanics in Reactor Technology (SMiRT-18), 2005.
121. Mitchell, M.N., *A Study into the Key Factors Influencing the Design Life of a PBMR Side Reflector Block*. 2004: Plas Tan-Y-Bwlch, Maentwrog, Gwynedd, United Kingdom.
122. Janse van Rensburg, J.J. and Kleingeld, M., *Investigating Leakage and Bypass Flows in an HTR Using a CFD Methodology*. Nuclear Engineering and Design, 2011. 241(12): p. 4960-4971.
123. Janse van Rensburg, J.J. and Kleingeld, M., *CFD Applications in the Pebble Bed Modular Reactor Project: A Decade of Progress*. Nuclear Engineering and Design, 2011. 241(9): p. 3683-3696.
124. Janse van Rensburg, J.J. and Kleingeld, M., *An Integral CFD Approach for the Thermal Simulation of the PBMR Reactor Unit*. Nuclear Engineering and Design, 2011. 241(8): p. 3130-3141.
125. Janse van Rensburg, J.J. and Kleingeld, M., *A CFD Method to Evaluate the Integrated Influence of Leakage and Bypass Flows on the PBMR Reactor Unit*. Nuclear Engineering and Design, 2010. 240(11): p. 3841-3850.
126. Prinsloo, P., *Core Structure Ceramics Design Description*, in *PBMR (Pty) Ltd. Proprietary Document*. 2006, PBMR.
127. Haecker, R., *AN-98 Pre-Tests for Validation Tests on Upper Centre Reflector Corner Blocks*, in *PBMR (Pty) Ltd. Proprietary Document*. 2009, SGL Carbon Group.
128. Fechter, M. and Fazluddin, S., *NGB-18 Graphite Data Sheet*, in *PBMR (Pty) Ltd. Proprietary Document*. 2009, PBMR.
129. Fischer, H., Rentzsch, W., and Marx, R., *A Modified Size Effect Model for Brittle Nonmetallic Materials*. Engineering Fracture Mechanics, 2002. 69(7): p. 781-791.
130. Hindley, M.P. and Erasmus, C., *Neutron Reflector Block*. 2011, WO Patent WO/2011/151,801.

A. APPENDIX: GEOMETRIC LAYOUT OPTIMISATION OF GRAPHITE REFLECTOR COMPONENTS [103]

Christiaan Erasmus, Michael P Hindley

Pebble Bed Modular Reactor (Pty) Ltd.

P.O. Box 9396, Centurion, South Africa 0046

Phone and email: +27-82-791-3579, christiaan.erasmus@gmail.com

Abstract

The graphite blocks used in a high-temperature gas-cooled nuclear reactor are exposed to high temperatures and fast neutron flux level. This causes the material to shrink and swell which leads to stresses created internally to the blocks. In addition, under these conditions, most other material properties of the graphite change as well. Due to this, the stress analysis of graphite blocks is complicated and the behaviour of the blocks can be counter-intuitive, making it a different discipline from the stress analysis of other structures.

We have implemented an automated analysis system that completes this task in an efficient, accurate and repeatable manner. Using this system, the behaviour of side reflector graphite blocks used in a pebble bed reactor under operational conditions is investigated and this knowledge was used to improve the design and the operational life of the side reflector blocks. The new proposed design doubles the expected life of side reflector blocks in a pebble bed core, allowing the life to approach the theoretical limit of life based on the material turnaround point.

A.1 Introduction

As the pebble bed reactor core contained thousands of graphite components, manual analysis setup, execution and results reporting of a lifetime irradiation analysis of each component individually would be an extremely onerous task. For this reason, the analysis setup has been largely automated by Pebble Bed Modular Reactor (PBMR) (Pty) Ltd. The first level of results extraction and reporting is automated and presented in a standardised report. The report is intended to provide traceability of the type of analysis performed, the input data and software versions used and the location of results. In addition, the standardised report format allows easy comparison of results between similar components, thus providing a useful starting point for compiling higher level structural integrity and design assessment reports. Further reports will also exist

for every graphite component that summarises and interprets the results for individual or groups of blocks, whichever is most appropriate.

The ease of use of the automated system and reports has made it possible to optimise the shape and topology of graphite blocks in a realistic time frame. The analysis required to determine the life of graphite blocks can be very time-consuming; automation of the analysis procedure saves a lot of time which is usually spent on verifying inputs and outputs, thus allowing the analyst to concentrate on improving the design.

The geometric layout presented in this paper allows the life of the annular core, used in the PBMR, to be extended by decades. It is based on the realisation that the blocks which are exposed directly to the core, and therefore to the highest temperature and neutron flux, need to be as small as possible to maximise the life. Unfortunately, simply making blocks narrower and lower makes the complexity of designing the block interfaces very difficult as providing control rod and cooling channels becomes nearly impossible. In addition, it increases the manufacturing cost and it could possibly reduce the heat conduction capacity of the side reflector (SR). The proposed layout decreases the frontal area of the graphite blocks exposed to the core without increasing the overall number of components in the core. This is achieved by stepping away from the conventional approach to make all inner layer blocks the same size and shape and creating two distinct groups of blocks in the front layer. The one block can be described as a control block, somewhat similar to familiar designs of graphite blocks. This block includes several holes to accommodate control and cooling functions in the core. The second block is a key block that locks adjacent control blocks together. This key block has no holes and is therefore no longer limited to a simple rectangular shape, but extends all the way from a keyway in the control block to the core outer perimeter.

By splitting up the blocks, each block has a smaller area exposed to the core that automatically increases the life of the block. In addition, other advantages can be noted for the design, including the reduction of neutron streaming and leak flow through the vertical spaces between blocks.

This paper presents the design with examples of the lifetime improvement achieved over conventional blocks subjected to the same conditions.

A.2 Background

A.2.1 Automated analysis system

An automated system for graphite reflector block analysis was developed. The automated system is based on ISight software that allows for the scripting and tracking of analysis procedures. The actual analysis procedures are completed using a combination of ANSYS Workbench and Marc/Mentat software. ANSYS Workbench is used for the manipulation of geometry and meshing, while the Marc/Mentat software is used for further pre-processing, analysis and post-processing of results. MATLAB is used to further analyse the results produced by

Marc/Mentat, including assessing the life of the graphite component based on the method described in Hindley *et al.* [78]. In addition, the analysis process makes use of Microsoft Excel, the DOS command language, MSC.Patran, Python scripting, MSC Procedure scripting, text file manipulation, data exchange with CCS Cluster and Microsoft Word.

Interaction between these software packages and the flow of information from one package to another are managed by ISight. The software allows the standardisation of workflows required to execute simulation-based design processes, it also facilitates the rapid integration of different programs and automates their execution. Figure A-1 shows the typical ISight workflow used to report on the analyses. The annotations indicate the operation that is performed at each stage of the analysis.

The final product of the analysis procedure is an automated report that includes all relevant input and result information. This standardised report allows the quick and efficient review of results. This facilitates design changes to be implemented based on the results. The automated reports are also used as a starting point for completing more comprehensive analysis reports of individual or groups of graphite blocks.

Benefits of automation:

- Speed (one process executed straight after the completion of the previous task).
- Efficiency and multitasking (ISight will run in the background while the operator works on other tasks).
- Reduces human error (numerous repetitive tasks, copying and transfer of files between control directories, etc.). Table A-1 summarises observations with regards to time taken to complete analysis tasks either manually or using the automated system.

Table A-1: Speed up experienced due to automation of process

	<i>Task Completion Time (Minutes)</i>	
	<i>Manual</i>	<i>ISight Automated</i>
Model set-up	45	10
Analysis submission to CCS Cluster	5	1
Results extraction	90	15
Total	140	26

- Automation gives the completed irradiated analysis of any graphite component in the core within a very short time. This gives the capability to evaluate the concepts of the same component quickly and easily.

- Gives the capability of handling design changes effectively and smoothly.
- Possible problems in design are identified very early in design.
- Automation reduces the risk of human error.
- Automation allows stochastic methods to be employed [63].

A.3 Proposed layout improvements

A.3.1 Baseline design

The baseline block design used is from the SR design of the HTR-Modul created by Interatom during the 1980s [90]. It features an elongated block with a control rod hole at the front and a riser channel at the back. In addition, it has features allowing the alignment of adjacent blocks in the SR. It was found that, based on the temperature and neutron fluence levels expected by PBMR in a 250 MWth core, the blocks exposed to the most damaging conditions will have a lifespan of 9.15 full power years (FPY). This is clearly insufficient when considering a plant lifetime design specification of 40 years. Although the replacement of SR blocks is technically feasible, it would be uneconomical to replace these blocks every nine to 10 years during the life of a plant.

The first option available to improve the block life is to reduce the size of the blocks. This also has an economical impact, but it will be less than that of replacing the SR more often. It was found that, by reducing the height of the blocks by half, the blocks exposed to the most damaging conditions will have a lifespan of 12.9 FPY. Reducing the angular size of the blocks by 12.5% further increases the life to 15.2 FPY. Reducing the angular size of the blocks further is impractical due to space constraints associated with control rod feeding mechanisms.

The introduction of more complicated solutions, like the addition of slots to the front face, has the potential to further increase the theoretical life of the blocks; however, this introduces stress concentrations to the blocks. Coupled with the brittle nature of graphite and the unknowns associated with large stresses applied to small areas, it is an uncomfortable match. It was, however, found that it is possible to increase the theoretically-predicted life of the blocks significantly by adding these features, but it is difficult to assess the additional statistical failure probability introduced by adding the associated stress concentrations. A more extensive testing programme than that already conducted by PBMR [78] will first have to be launched in order to determine the effect of the notches on the graphite failure probability.

Figure A-2 shows the baseline design of an SR block and Figure A-3 shows an assembly of the baseline blocks to form an annulus that, together with an outer annulus, will make up one level of a pebble bed SR.

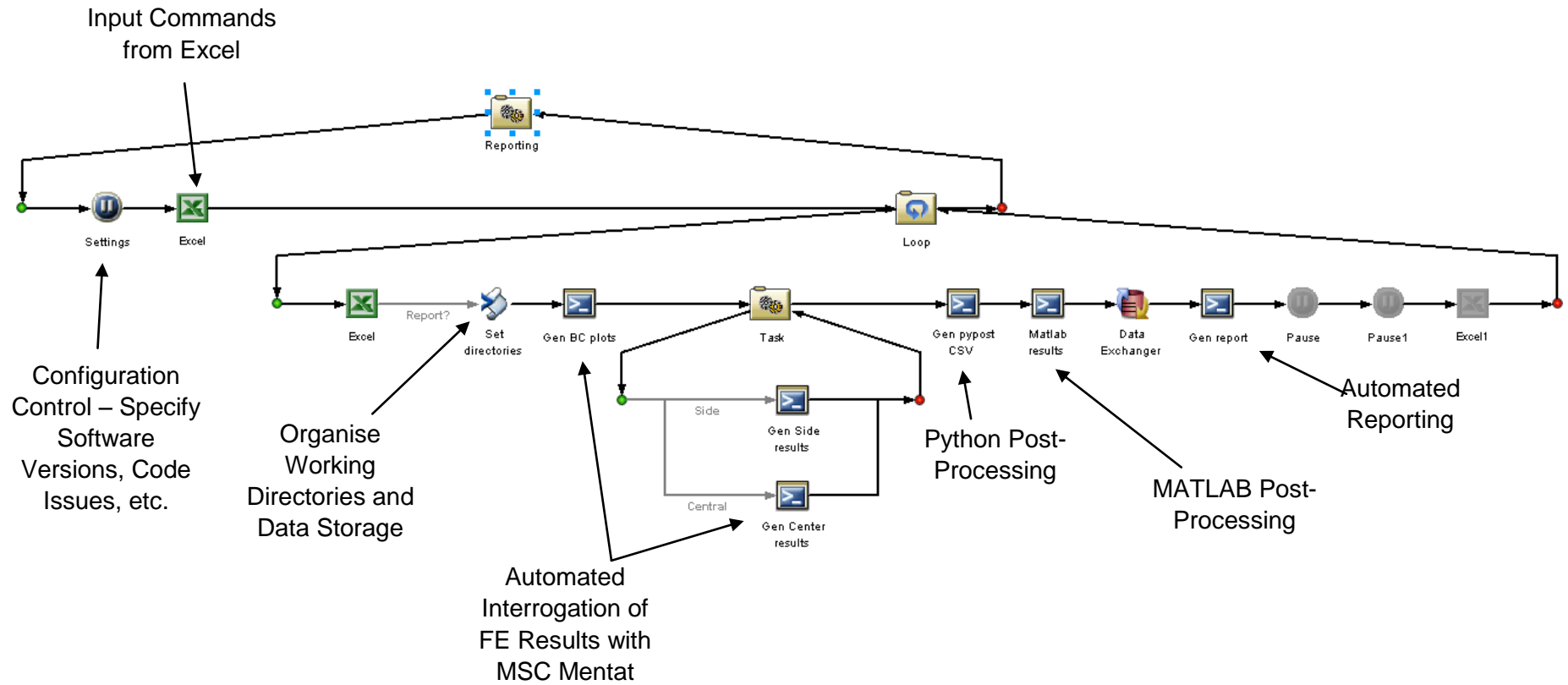


Figure A-1: Example of workflow set up in ISee to create a post-process and report on a completed analysis

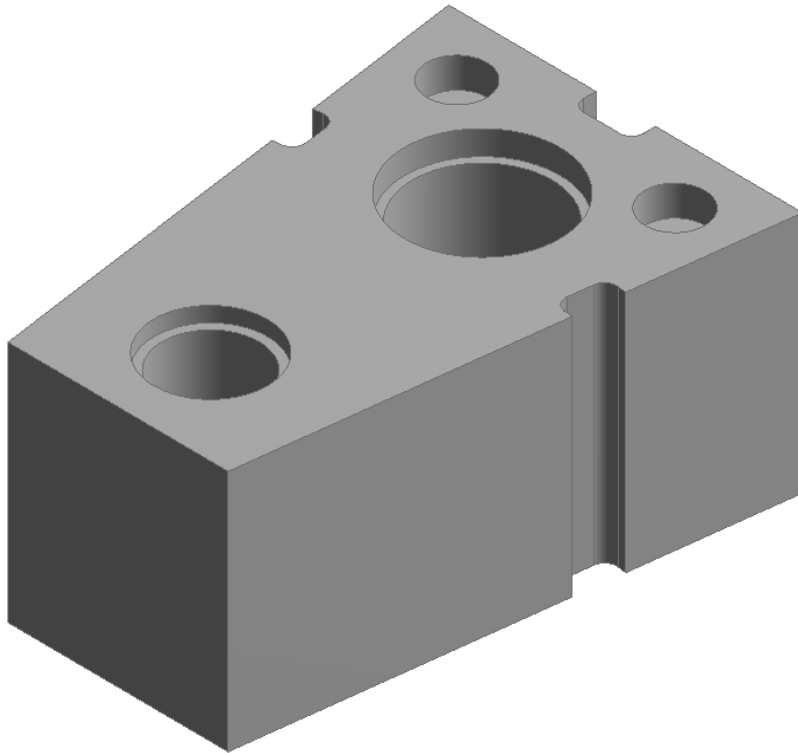


Figure A-2: View of baseline SR design

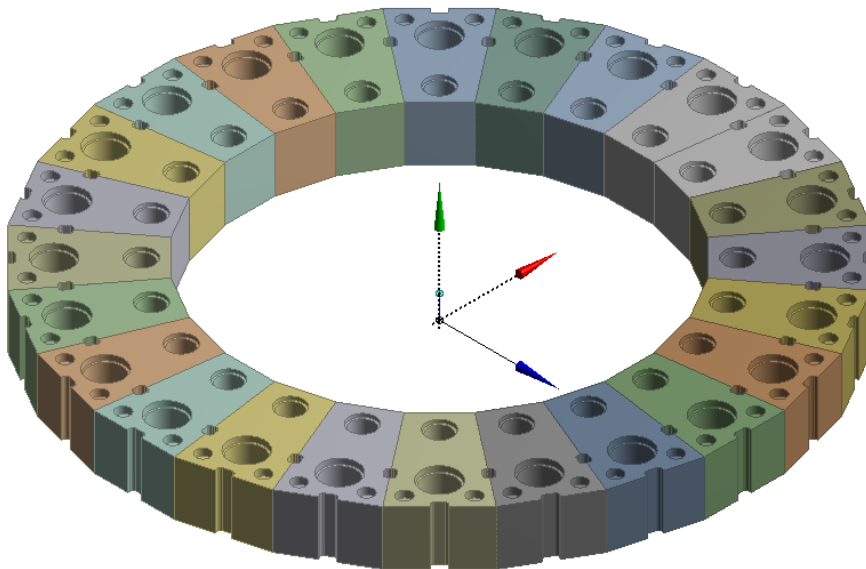


Figure A-3: View of a single layer of the SR made up by the baseline reflector blocks

A.3.2 Proposed design

Reducing the volume of individual blocks exposed to high levels of fast neutron fluence has a large effect on the expected lifetime of the graphite block. This can be seen from the increasing lifetime of blocks as they are reduced in size. Introducing slots to the block acts to subdivide the exposed face of the block into smaller segments, thereby effectively reducing the volume of these segments and spreading out the energy introduced to the block as a whole, thereby lowering stress and increasing block lifetime.

Implemented a design change, is novel by reducing the volume of the block section surrounding the control channel, while keeping the back section, which houses the riser channel, at its original size. Thereby, the volume of material in the block exposed to high, fast neutron fluence is reduced. This, of course, would create gaps between adjacent SR blocks. These gaps are filled with secondary blocks that act as keys as well as neutron reflector blocks. This block thus extends from the normal position of the key in a conventional block to the exposed face of the SR.

The effect of splitting the incident energy between two blocks is dramatic. The predicted life of these proposed blocks are given in Section A.4.4.

Figure A-4 shows the blocks used in the proposed reflector design. It can be seen that the two blocks are fully interlocking and that successive pairs of blocks can be lined up to form an annulus. Figure A-5 shows an assembly of the proposed blocks to form an annulus that, together with an outer annulus, will make up one level of a pebble bed SR.

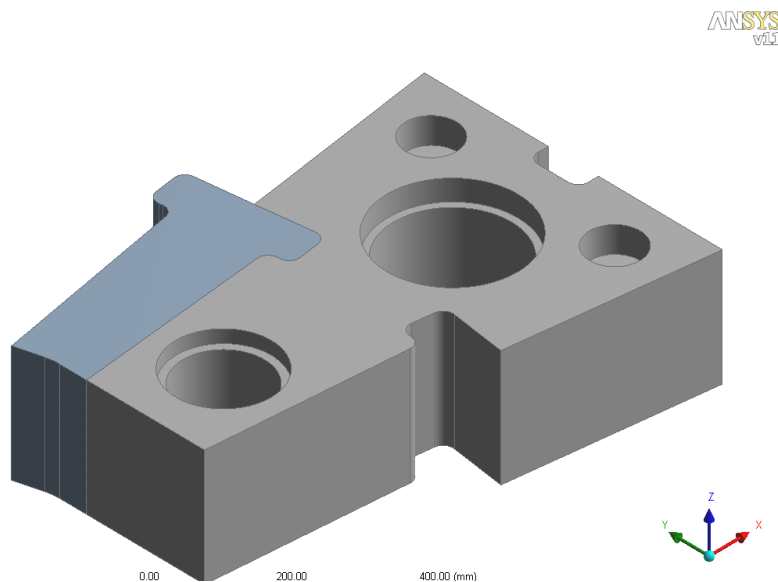


Figure A-4: View of an SR design utilising control rod block and key block

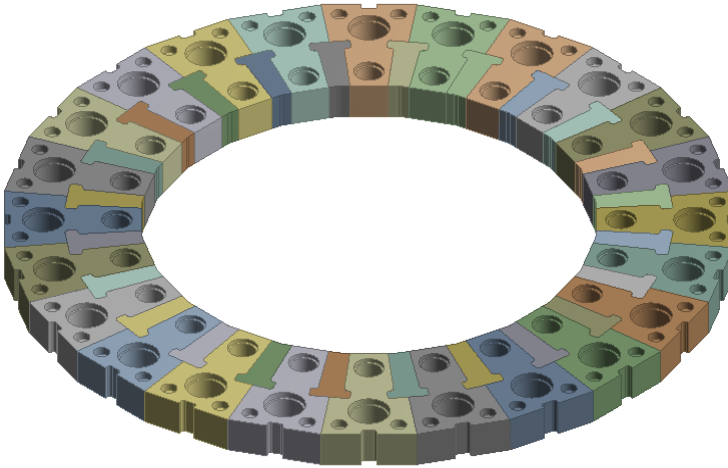


Figure A-5: View of a single layer of the SR made up of the control rod blocks and key blocks

A.4 Results

A.4.1 Stress intensity

The formulation of the physically-based failure criterion, used for graphite block analyses, is based on the maximum deformation energy (MDE) theory [37]. The hypothesis is that the elastic energy density, stored in a given material element at the moment of fracture, is equal to the energy density that is stored in the uniaxially loaded test specimen at fracture [56].

The allowable stress limits denote a probability of failure (PoF) of the graphite material, i.e. 10^{-2} tensile and 10^{-2} bending, and compare this to what is called the stress intensity. If the stress intensity exceeds the allowable stress, then the block is deemed to have failed. Physically, it means that one in every 100 tensile test samples will fail at the specified allowable stress limit, 10^{-2} tensile.

Stress intensity is given in Equation A-1

$$\sigma_v = \sqrt{\bar{\sigma}_1^2 + \bar{\sigma}_2^2 + \bar{\sigma}_3^2 - 2 \cdot \nu \cdot (\bar{\sigma}_1 \cdot \bar{\sigma}_2 + \bar{\sigma}_1 \cdot \bar{\sigma}_3 + \bar{\sigma}_2 \cdot \bar{\sigma}_3)} \quad (\text{A-1})$$

Where

ν = Poisson's ratio

$\bar{\sigma}_i = f \sigma_i$ for $i=1,2,3$

with σ_1 , σ_2 and σ_3 being the three components of principal stress. The factor f distinguishes between tensile and compressive stress states:

$f = 1$ if σ_i is a tensile stress, and

$f = R$ if σ_i is a compressive stress (R is the ratio of mean tensile to mean compressive strength).

The compressive strength of graphite is several times higher than the tensile strength. Thus, to enable direct comparison of tensile and compressive stress components, all compressive principal stress components are converted to their equivalent tensile stress (in terms of likelihood to cause failure) by multiplying by a weighting factor (R) equal to the ratio of mean tensile to mean compressive strength.

In the following sections, stress intensity, as defined above, is used to describe the stress in the blocks.

A.4.2 Full power years

FPY is used as a unit of time to make the results presented more understandable. In reality, the lifetime is predicted in relation to the fast neutron fluence that the front face of the block has been exposed to. An FPY represents the fast neutron fluence accumulated by the block during one year of operation at 100% capacity of the core. Therefore, if the core is run at less than 100% capacity, it will take more than a calendar year of operation to accumulate one FPY.

A.4.3 Baseline design

The stress levels in the baseline block design exposed to the temperatures and fast neutron flux levels in the pebble bed core increases to unacceptable levels within 20 FPY. As can be seen in Figure A-6, the stress intensity exceeds the 10^{-2} tensile allowable stress at 20 years. The blue line (+ symbol) represents the maximum stress present anywhere in the block at any time step under normal operational conditions. The red line (* symbol) represents the stress in the block that occurs if the block is returned to shutdown conditions from the normal operational conditions. This stress may increase or decrease due to the temperature in the block changing from operational conditions to shutdown conditions.

An alternative statistical assessment method is used to evaluate the block PoF as is described in Hindley *et al.* [78]. This result can be seen in Figure A-7. According to this assessment, the block lifespan of 12.9 FPY is predicted.

Figure A-8 shows the stress intensity field present in the block at the predicted end of life. The maximum stress is at the top and bottom edge of the block, in line with the thinnest section of the frontal part of the block. The principal stresses at this location are in tension. The front face of the block is also in tension. The stress is induced by the graphite shrinking in the region of the front face. The

effect of the shrinkage is amplified by the size of the block, thus a larger block has higher stress and a smaller block lower stress. This is, however, only true for the frontal part of the block where large shrinkage is present. The back of the block is protected from the fast neutron flux by the frontal part of the block and therefore, the shrinkage strain at the back of the block is orders of magnitude smaller than that at the front. So small in fact that it becomes insignificant [104].

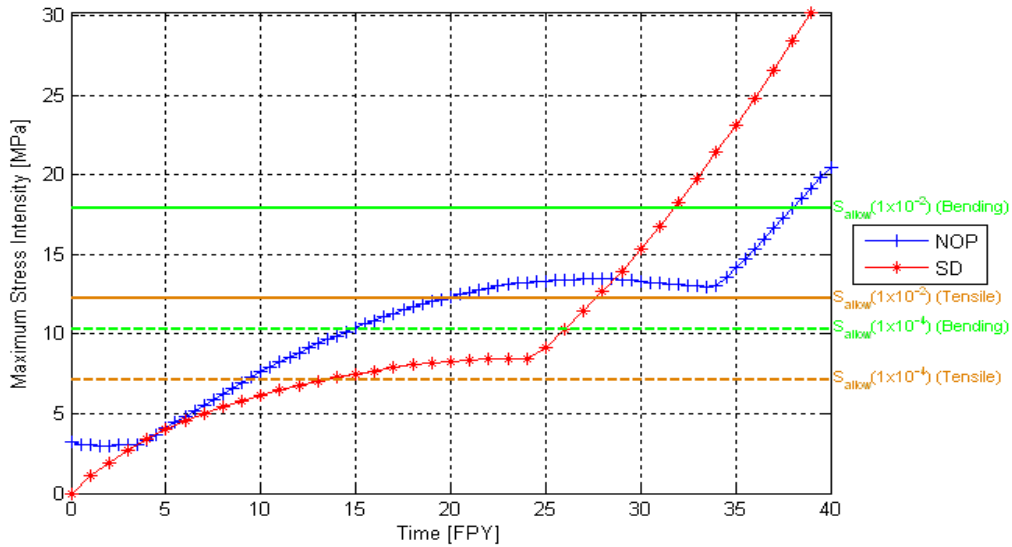


Figure A-6: Maximum stress intensity anywhere in the baseline block at a given time. Blue line (+) for stress under normal operation. Red line (*) for stress at shutdown.

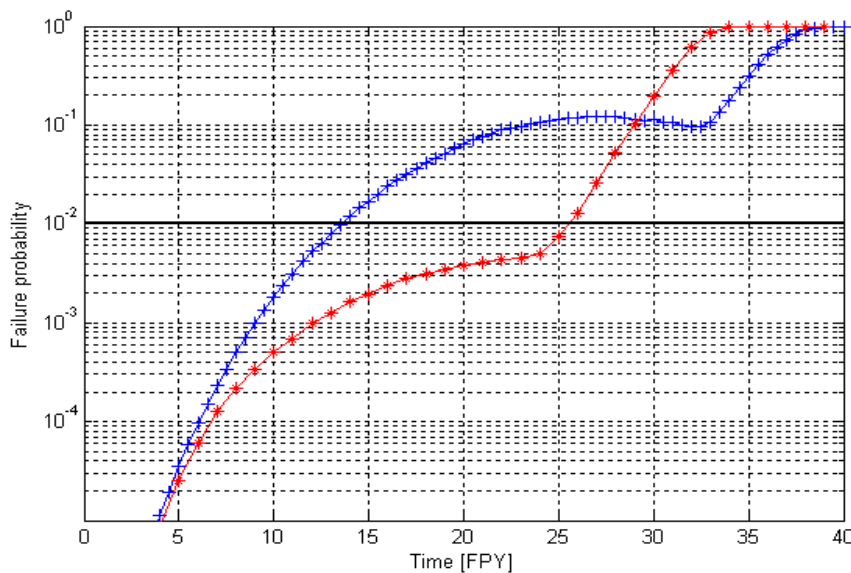


Figure A-7: Predicted failure probability for the baseline block at a given time. Blue line (+) for stress under normal operation. Red line (*) for stress at shutdown.

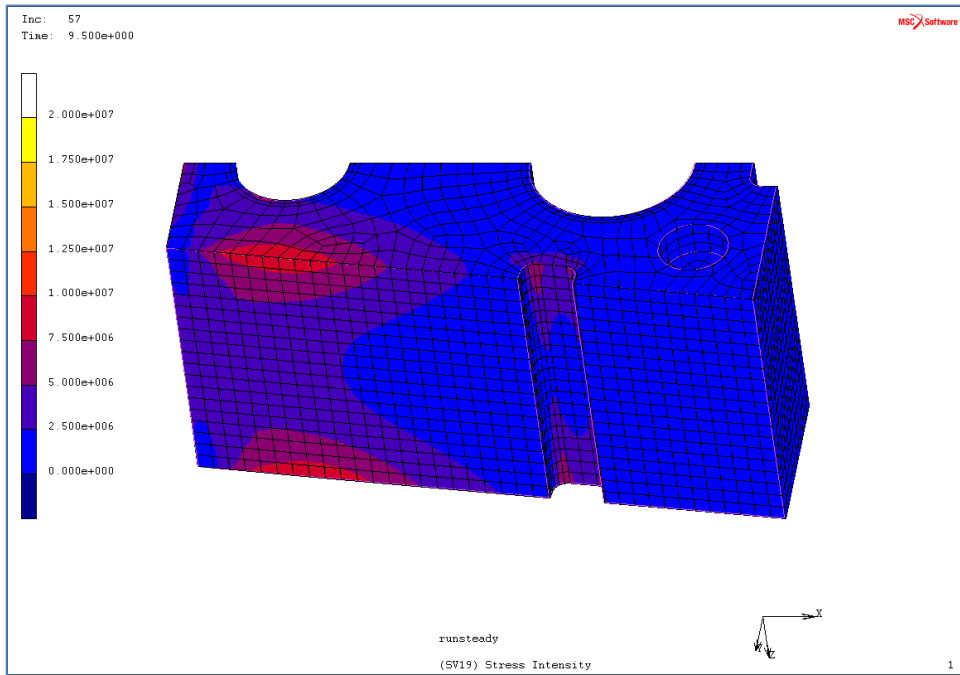


Figure A-8: Stress intensity contour plot of block at predicted end of life

For comparison, the stress in the baseline block at 18 FPY is shown in Figure A-9 and the stress in the proposed control rod block at 18 FPY in Figure A-10. At this stage, the shrinkage strain at the front surface of both blocks are the same, but the stress in the proposed block is around half of that present in the baseline block. The same is true for the key block shown in Figure A-11. The contour bands used in all the stress intensity figures are identical.

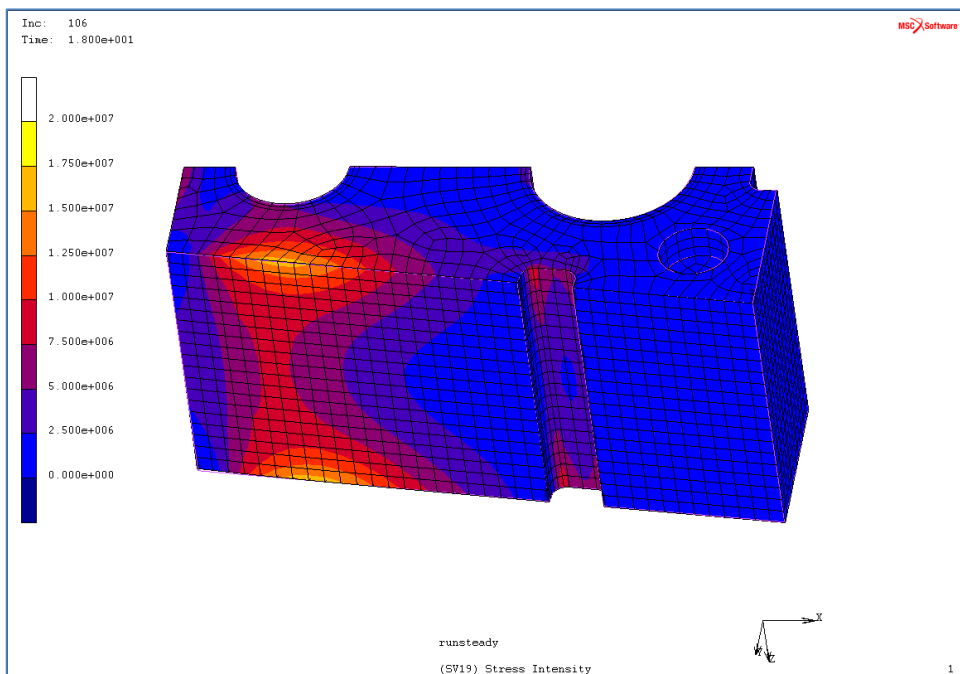


Figure A-9: Stress intensity contour plot of the baseline block at 18 FPY

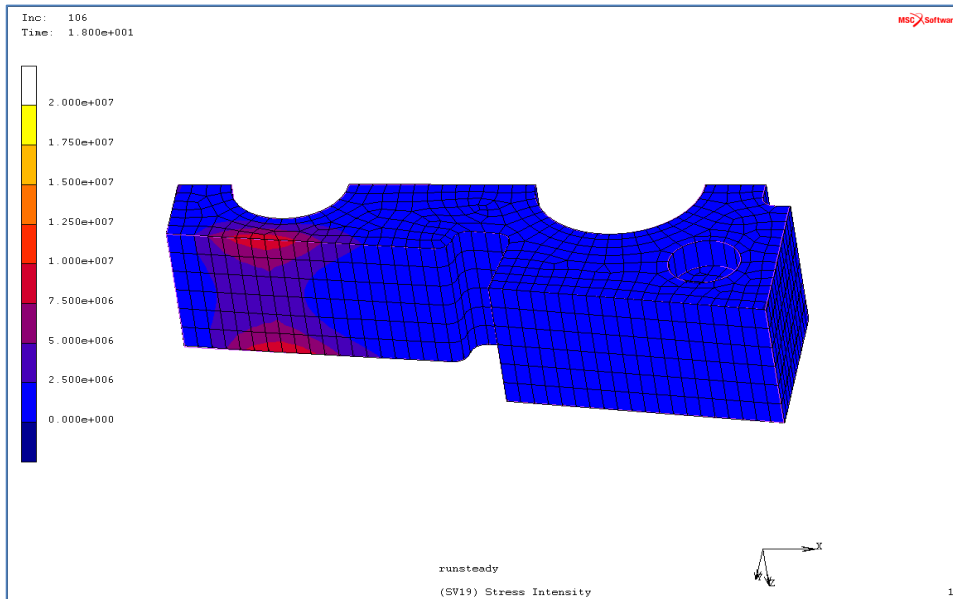


Figure A-10: Stress intensity contour plot of the proposed control rod block at 18 FPY

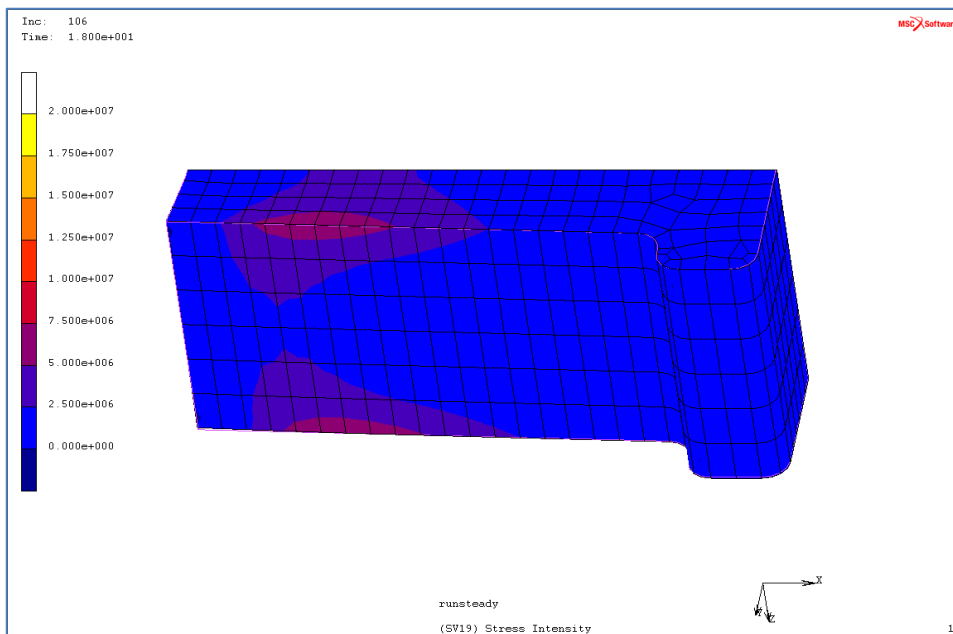


Figure A-11: Stress intensity contour plot of the proposed key block at 18 FPY

A.4.4 Proposed design

The improvement in lifetime for the blocks is achieved by the lowering of the stress in the frontal section of the block observed in the baseline block. This reduces the failure probability sufficiently to delay excessive failure probability until material turnaround (the point where the material stops shrinking and starts swelling). The turnaround point represents a physical limit of graphite material

and is predictable and directly related to the amount of fast neutrons that have penetrated the material. Therefore, a large amount of uncertainty is eliminated and assessing the remaining life of the blocks becomes a matter of monitoring the fast neutron flux. Figure A-12 and Figure A-13 show the maximum stress intensity curves for the two proposed blocks. As opposed to the stress intensity in the baseline block (Figure A-6), the stress remains below the 10^{-2} tensile stress limit to beyond 30 FPY.

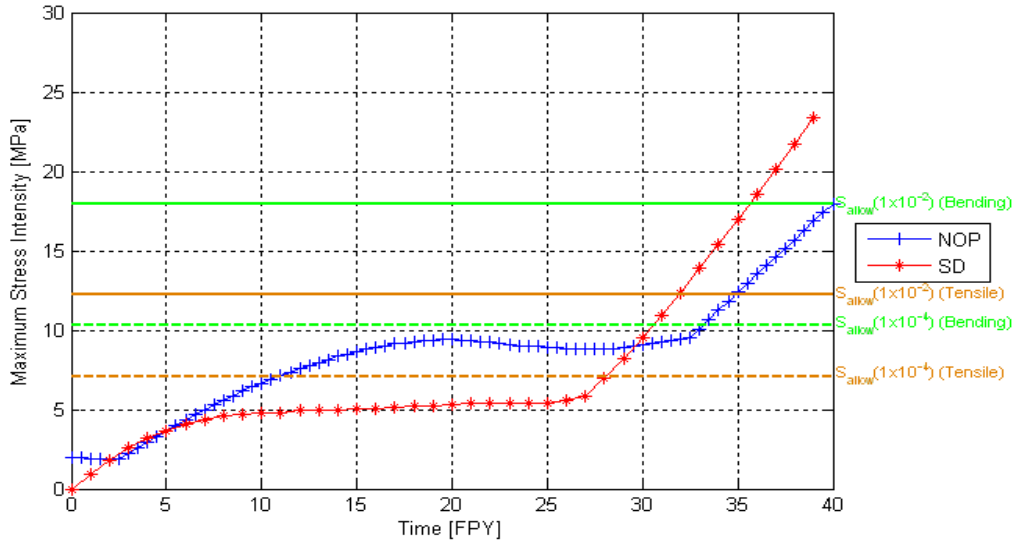


Figure A-12: Maximum stress intensity anywhere in the proposed control rod block at a given time. Blue line (+) for stress under normal operation. Red line (*) for stress at shutdown.

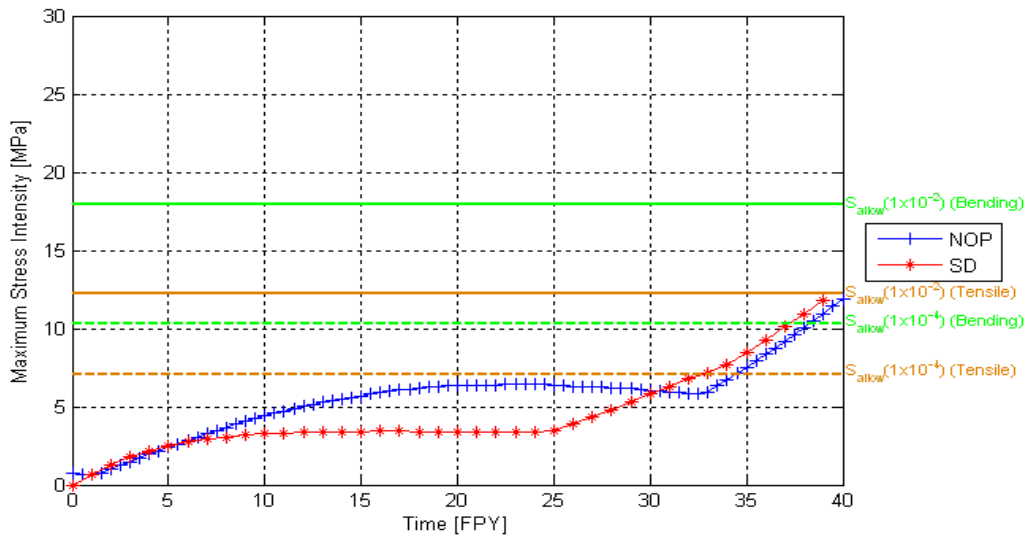


Figure A-13: Maximum stress intensity anywhere in the proposed key block at a given time. Blue line (+) for stress under normal operation. Red line (*) for stress at shutdown.

Based on the failure probability calculation, the proposed control rod block will achieve a life of 31.6 FPY, as shown in Figure A-14. The life of the key block is determined to be 36.6 FPY, as shown in Figure A-15.

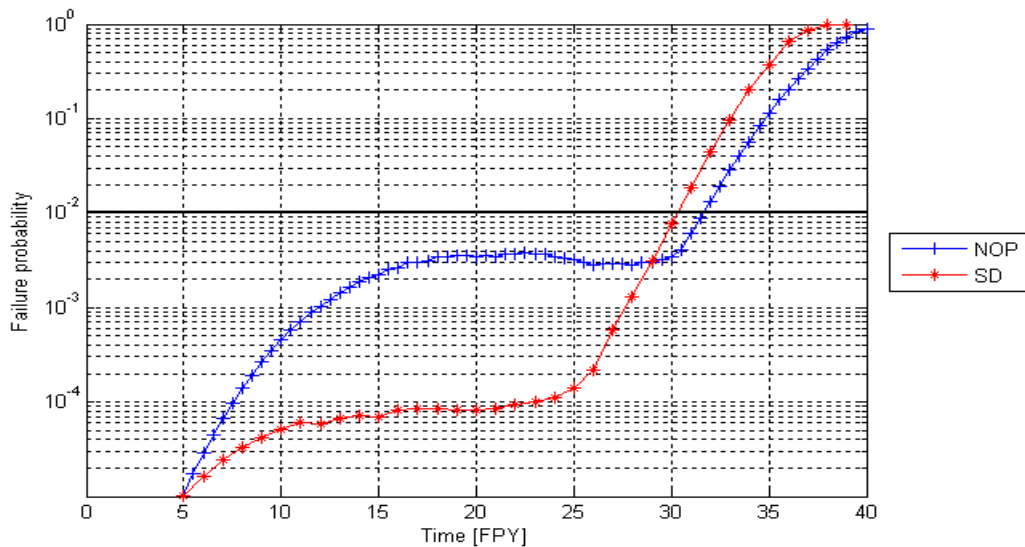


Figure A-14: Predicted failure probability for the proposed control rod block at a given time. Blue line (+) for stress under normal operation. Red line (*) for stress at shutdown.

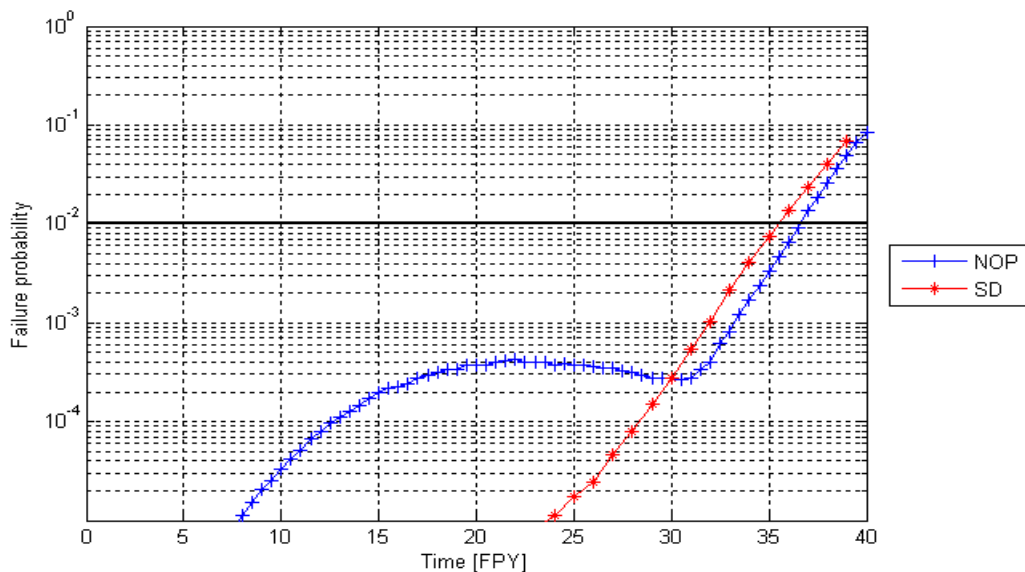


Figure A-15: Predicted failure probability for the proposed key block at a given time. Blue line (+) for stress under normal operation. Red line (*) for stress at shutdown.

Figure A-16 to Figure A-19 show that, in the proposed control rod block and key block, the maximum stress intensity at the time the failure probability exceeds allowable levels is no longer at the outside edges of the block, but has moved to

the centre of the block a few centimetres behind the front face. This is consistent with high stresses caused by the front-most material expanding while the material further back is still shrinking, giving rise to large differentials in strain and thus large stresses. Therefore, the high stresses in the blocks are caused by material turnaround.

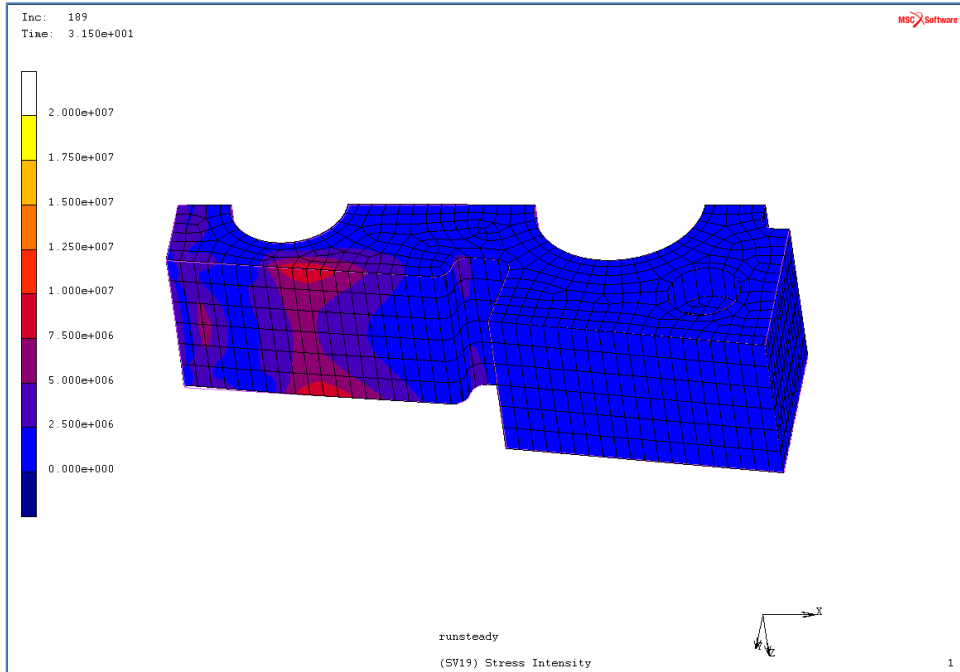


Figure A-16: Stress intensity contour plot of block at predicted end of life

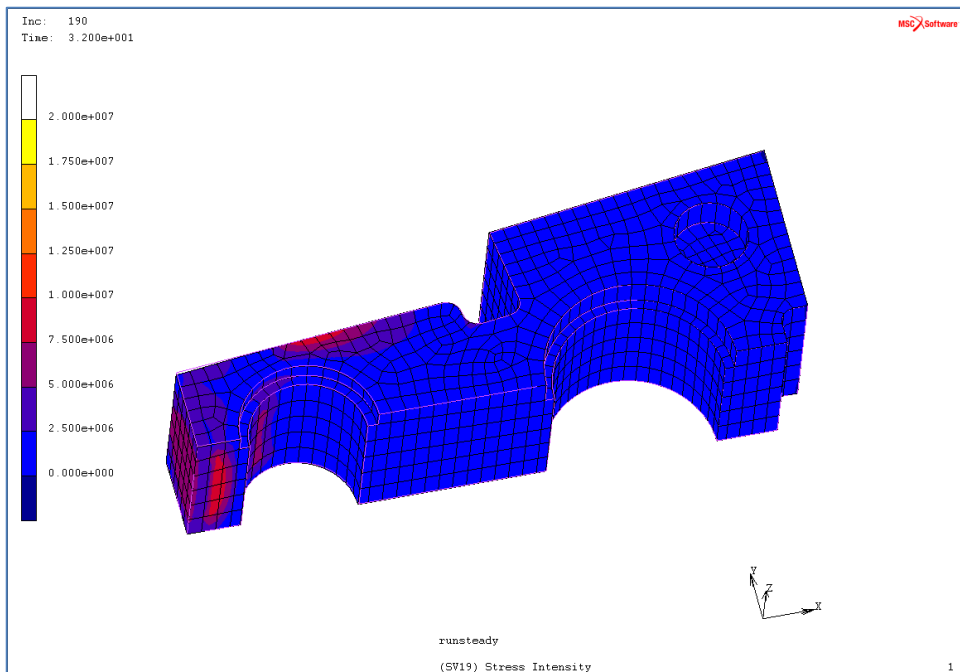


Figure A-17: Stress intensity contour plot of block at predicted end of life

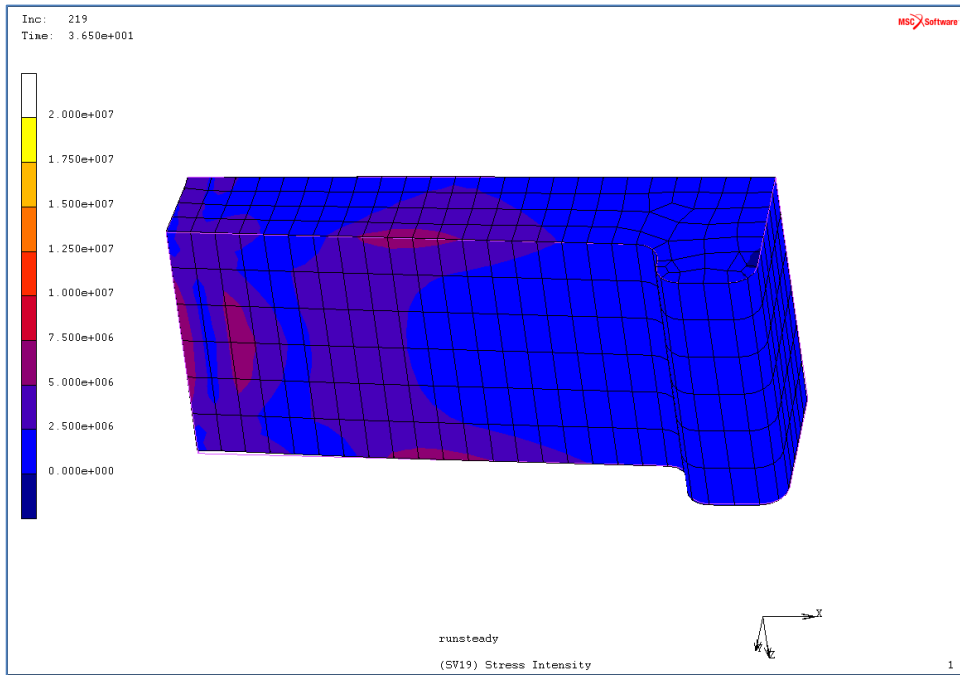


Figure A-18: Stress intensity contour plot of block at predicted end of life

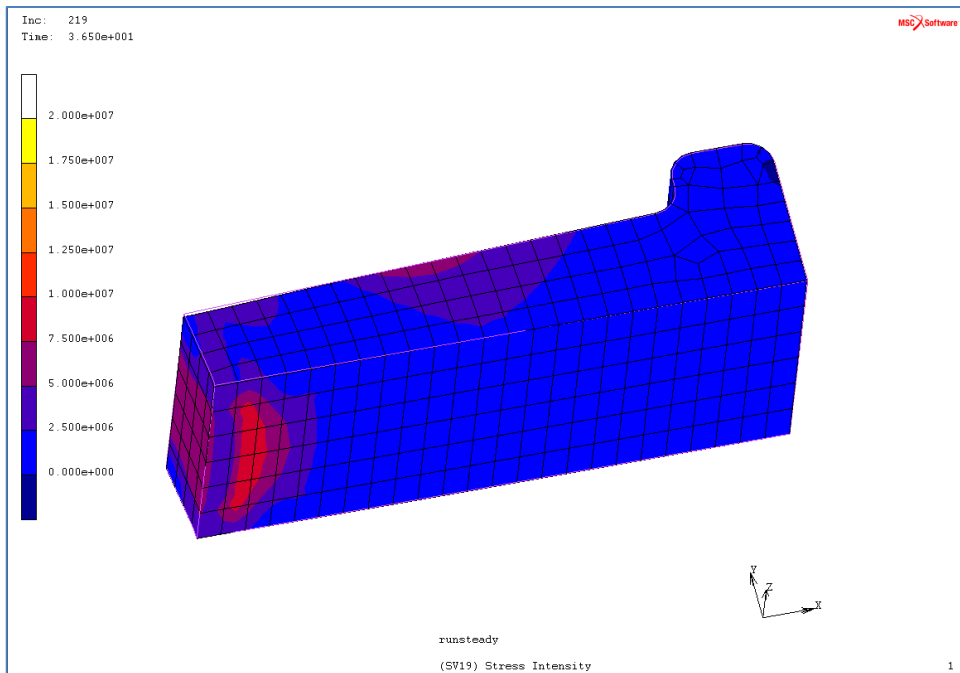


Figure A-19: Stress intensity contour plot of block at predicted end of life

A.5 Further development

Further topology optimisation of the block shape is possible. The following example shows that, by further decreasing the frontal area of the control rod

block while increasing the frontal area of the key block, a better balance between the lifetimes of the two blocks can be found. This design is shown in Figure A-20. The design also functions to maximise the effect of reducing neutron streaming by introducing curved sides.

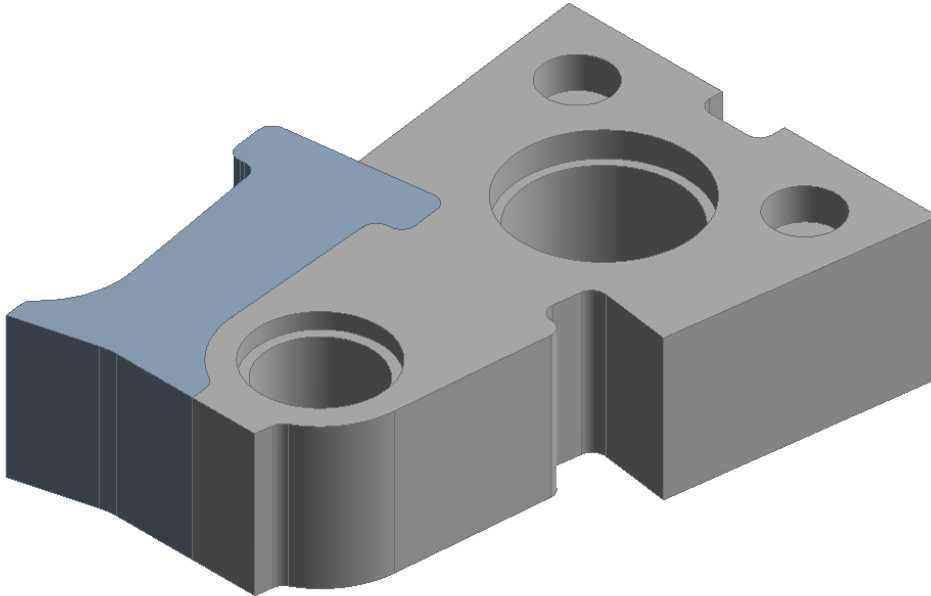


Figure A-20: Improved geometry using curved edges

Figure A-21 and Figure A-24 show that for the control rod block, the maximum stress intensity is reduced while the maximum stress intensity of the key block is increased. Figure A-23 and Figure A-26 show the stress intensity fields present in these blocks at the predicted failure point. Lower stress intensity in the control rod block is desirable as it houses the essential control rod channel and failure of one of these blocks could have more severe effects than failure of a key block.

The life predictions of the improved curved sided blocks are 33.5 FPY for the control rod block and 35.1 FPY for the key block. Thus, some of the key block life can be sacrificed in favour of improving the life of the control rod block, thereby bringing the lifetimes of the two blocks closer together.

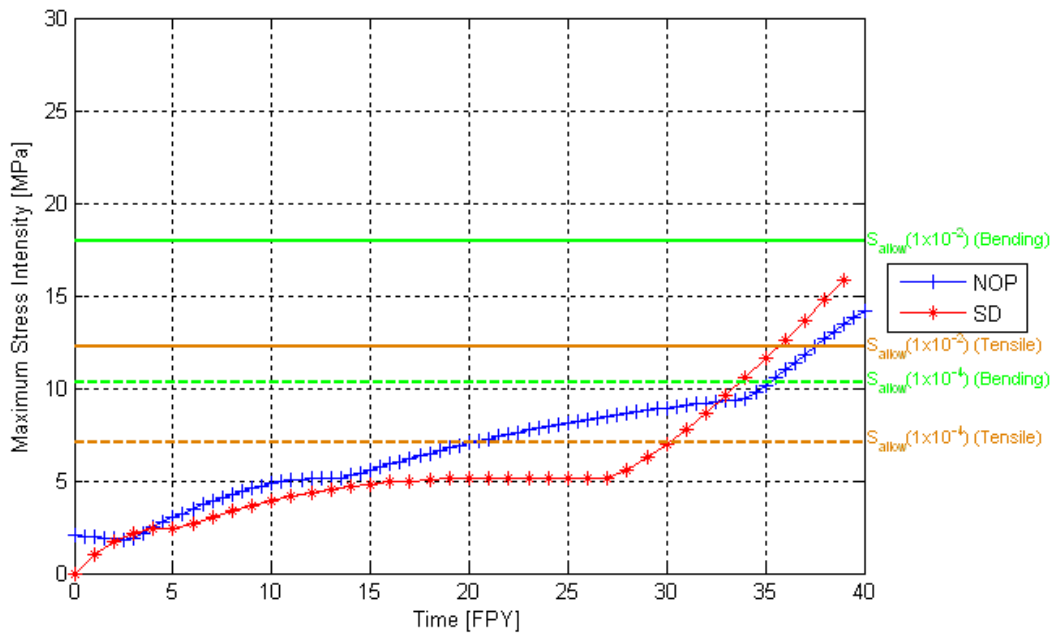


Figure A-21: Maximum stress intensity of curved sided control rod block

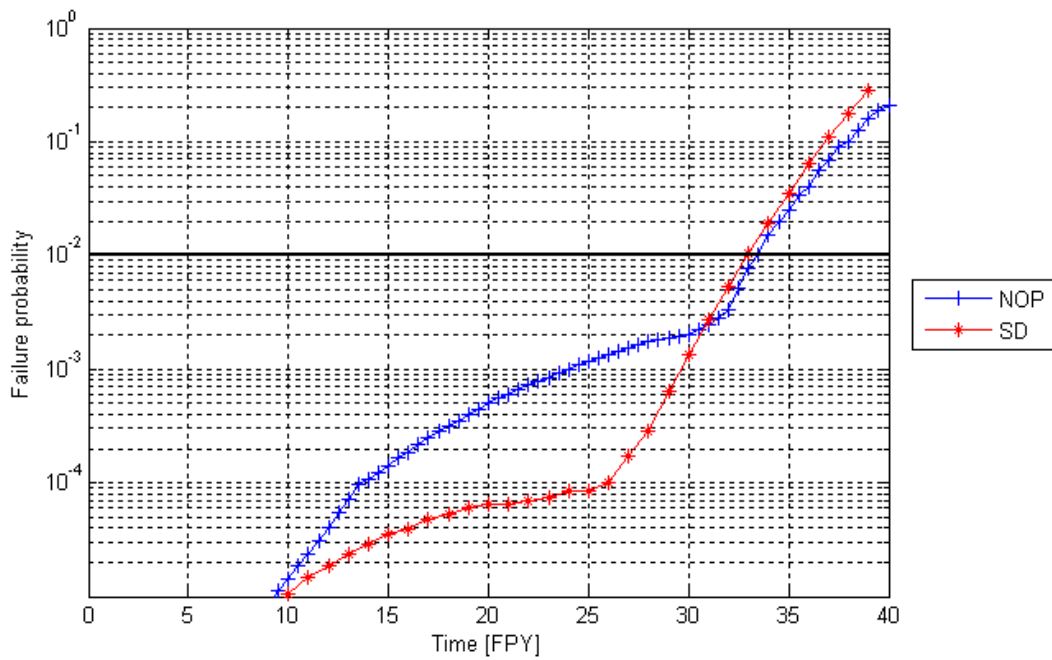


Figure A-22: Life prediction of curved sided control rod block

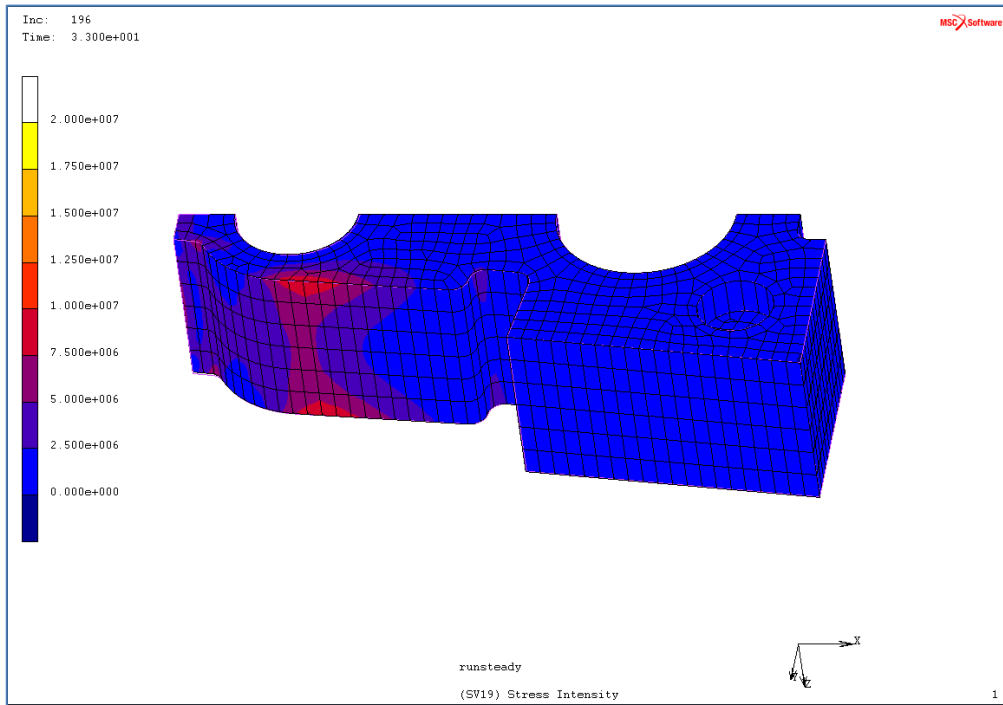


Figure A-23: Stress intensity contour plot of curved sided control rod block

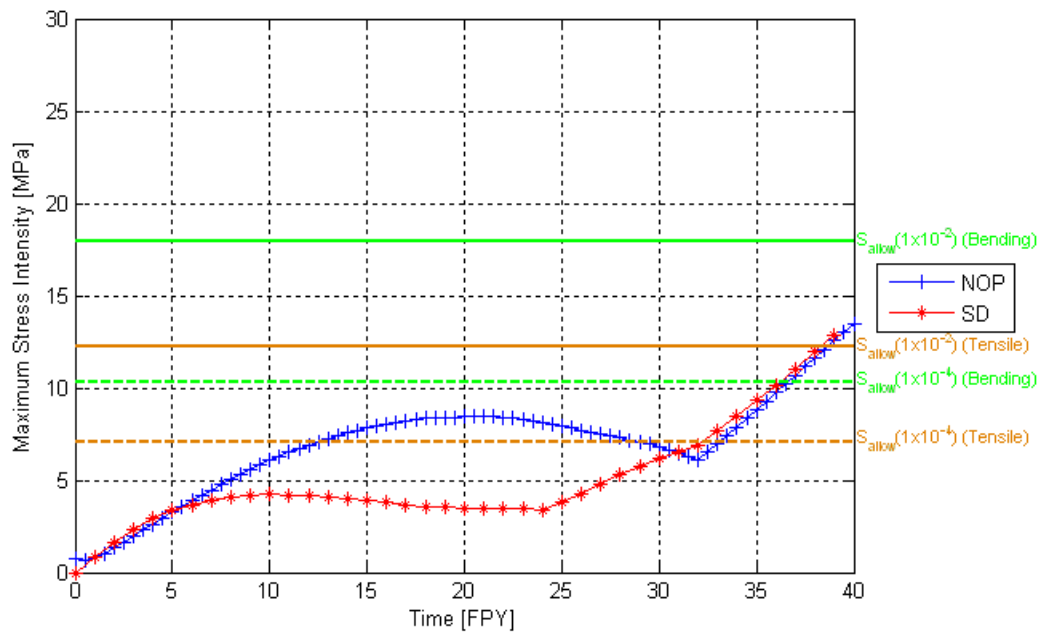


Figure A-24: Maximum stress intensity of curved sided key block

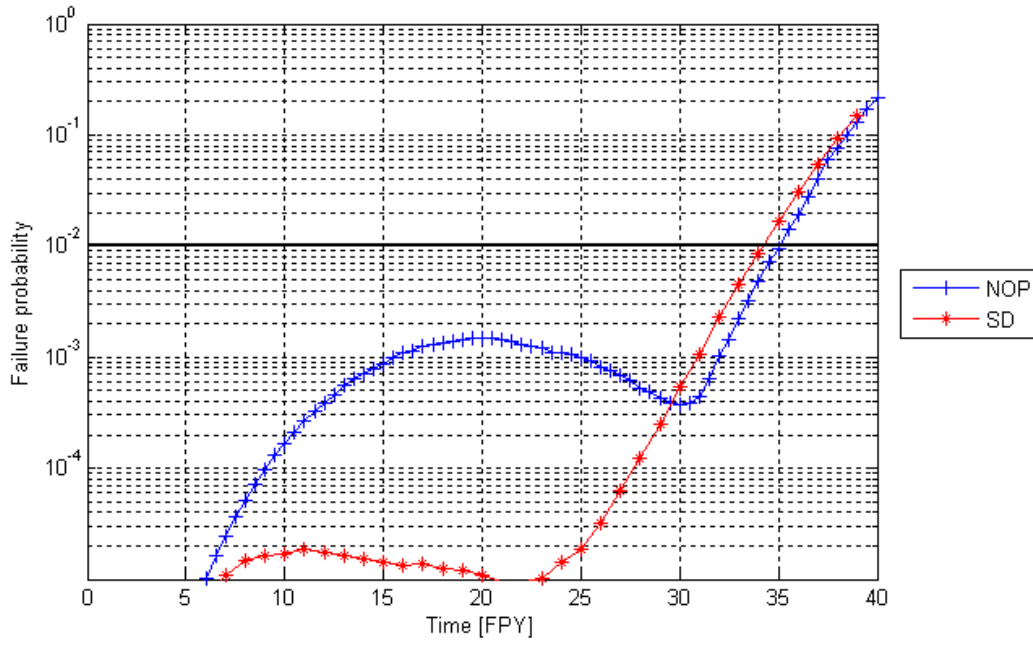


Figure A-25: Life prediction of curved sided key block

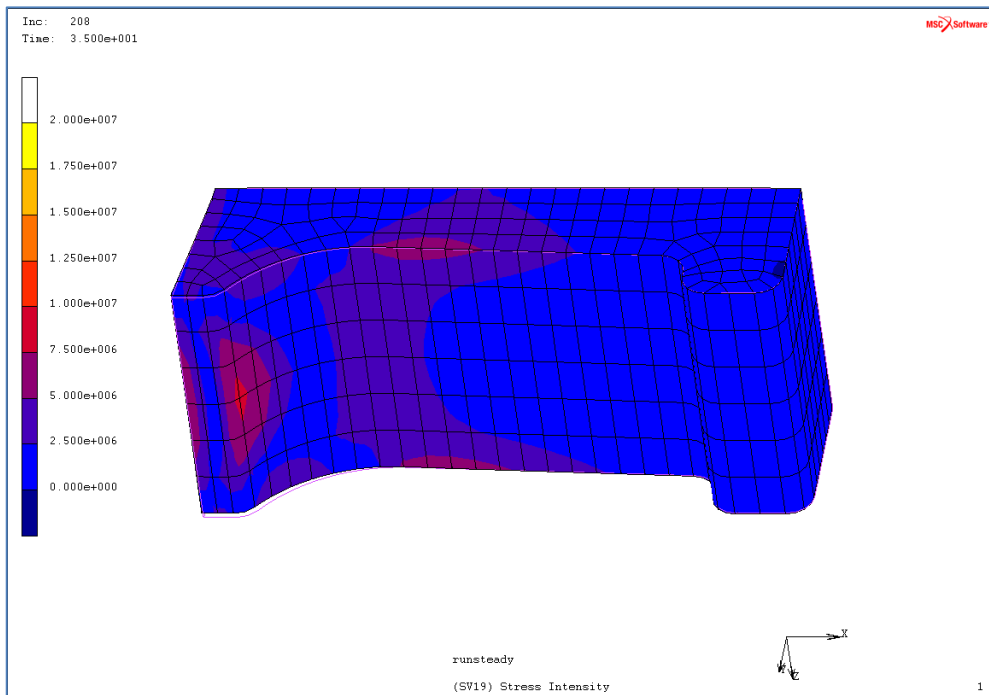


Figure A-26: Stress intensity contour plot of curved sided key block

A.6 Conclusion

We have found that it is possible to significantly increase the life of the SR blocks in a pebble bed reactor by changing the geometry of the blocks to minimise the volume of graphite in an individual block exposed to high fast neutron fluence.

The ability to perform quick and repeatable analyses of reflector block geometries facilitates the optimisation of the block design. By using such an automated method, a geometric optimum can be obtained for any HTR core design.

The optimisation of the lifetime of reflector components allows for a significant improvement to the economics of a pebble bed reactor. It would be prohibitively expensive to have four sets of core ceramics during a plant lifetime of 40 years. Except for the cost of the core components itself, replacement of the blocks will add additional downtime. At the cost of additional machining of core blocks, the life of the plant can be extended significantly, allowing an overall plant life of 60 years, with one core ceramic replacement mid-life.

B. APPENDIX: TEST CASE DESCRIPTIONS

Table B-1 to Table B-10 provide details of each test case analysed.

Table B-1: VP-00 test cases

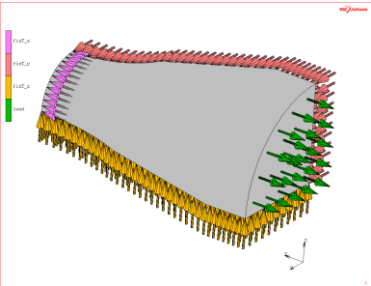
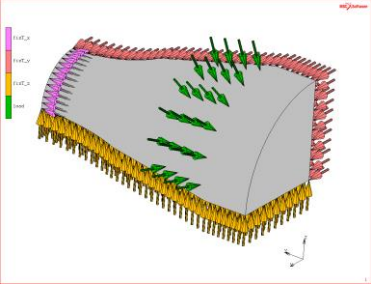
<i>VP</i>	<i>Test Case No.</i>	<i>Problem ID (from FE Analysis Report)</i>	<i>Mesh Refinement</i>	<i>FE Model Description</i>	<i>FE Model Illustration</i>
VP-00	1	VP-00.00	Coarse	End loaded	
	2	VP-00.01	Medium		
	3	VP-00.02	Fine		
	4	VP-00.03	Coarse	Clamped	
	5	VP-00.04	Medium		
	6	VP-00.05	Fine		

Table B-2: VP-01 test cases

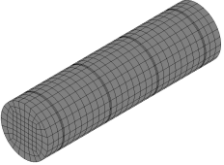
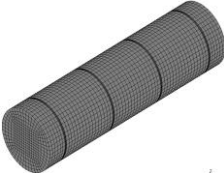
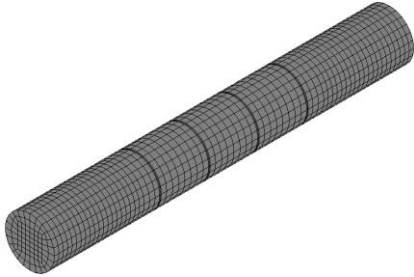
<i>VP</i>	<i>Test Case No.</i>	<i>Problem ID (from FE Analysis Report)</i>	<i>Mesh Refinement</i>	<i>FE Model Description</i>	<i>FE Model Illustration</i>
VP-01	7	VP-01.00	Medium	As in experiment	
	8	VP-01.01	Fine		
	9	VP-01.02	Medium	Extended lengthwise	

Table B-3: VP-19 test cases

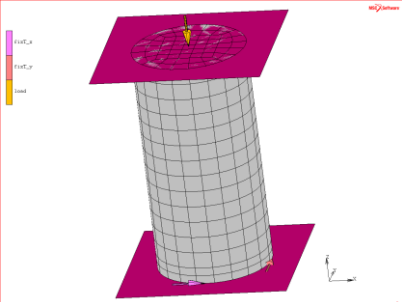
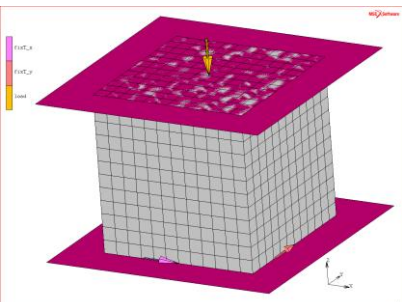
<i>VP</i>	<i>Test Case No.</i>	<i>Problem ID (from FE Analysis Report)</i>	<i>Mesh Refinement</i>	<i>FE Model Description</i>	<i>FE Model Illustration</i>
VP-19	10	VP-19.00	Coarse	Cylindrical sample	
	11	VP-19.01	Fine		
	12	VP-19.02	Coarse	Cubic sample	
	13	VP -19.03	Fine		

Table B-4: VP-15 test cases

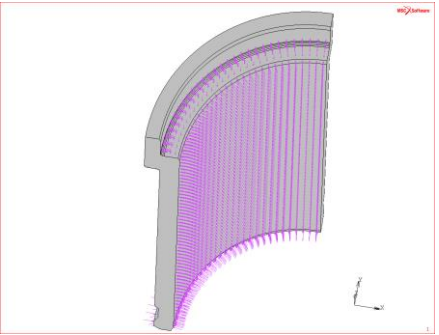
<i>VP</i>	<i>Test Case No.</i>	<i>Problem ID (from FE Analysis Report)</i>	<i>Mesh Refinement</i>	<i>FE Model Description</i>	<i>FE Model Illustration</i>
VP-15	57	VP-15.00	Coarse	As in experiment	
	58	VP-15.01	Fine		

Table B-5: VP-17 test cases

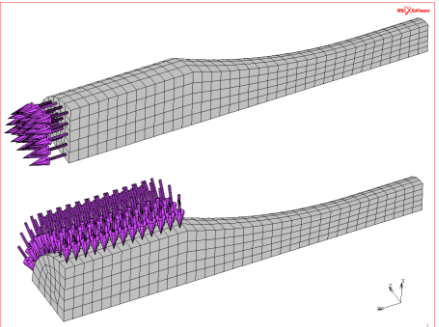
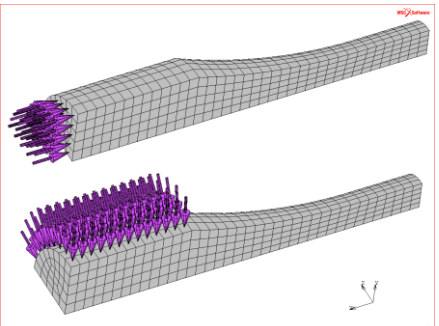
<i>VP</i>	<i>Test Case No.</i>	<i>Problem ID (from FE Analysis Report)</i>	<i>Mesh Refinement</i>	<i>FE Model Description</i>	<i>FE Model Illustration</i>
VP-17	59	VP-17.00	Coarse	Tensile test	
	60	VP-17.01	Fine		
	61	VP-17.02	Coarse	Compressive test	
	62	VP-17.03	Fine		

Table B-6: VP-18 test cases

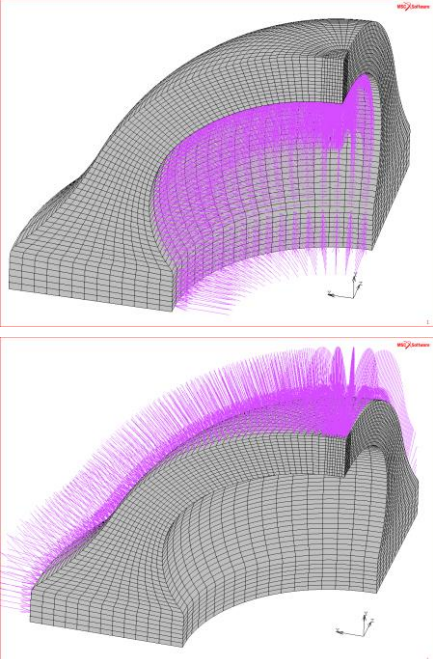
<i>VP</i>	<i>Test Case No.</i>	<i>Problem ID (from FE Analysis Report)</i>	<i>Mesh Refinement</i>	<i>FE Model Description</i>	<i>FE Model Illustration</i>
VP-18	63	VP-18.00	Coarse	Internal pressure	
	64	VP-18.01	Medium		
	65	VP-18.02	Fine		
	66	VP-18.03	Coarse	External pressure	
	67	VP-18.04	Medium		
	68	VP-18.05	Fine		

Table B-7: VP-12 Geometry 1, test direction 1 test cases

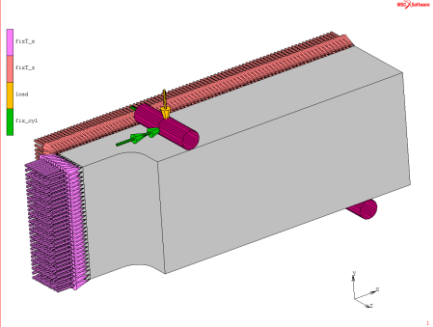
<i>VP</i>	<i>Test Case No.</i>	<i>Problem ID (from FE Analysis Report)</i>	<i>Mesh Refinement</i>	<i>FE Model Description</i>	<i>FE Model Illustration</i>
VP-12	14	VP-12.00	Coarse	Geometry 1, test direction 1, 1 mm radius	
	15	VP-12.01	Medium		
	16	VP-12.02	Fine		
	17	VP-12.03	Coarse	Geometry 1, test direction 1, 5 mm radius	
	18	VP-12.04	Medium		
	19	VP-12.05	Fine		
	20	VP-12.06	Coarse	Geometry 1, test direction 1, 10 mm radius	
	21	VP-12.07	Medium		
	22	VP-12.08	Fine		
	23	VP-12.09	Coarse	Geometry 1, test direction 1, 20 mm radius	
	24	VP-12.10	Medium		
25	VP-12.11	Fine			

Table B-8: VP-12 Geometry 1, test direction 2 test cases

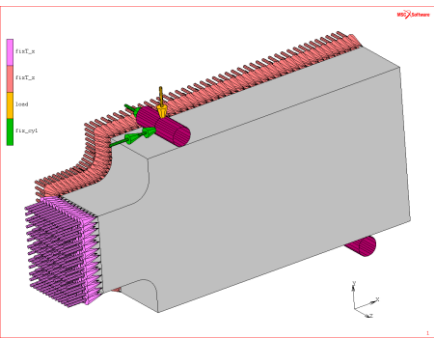
<i>VP</i>	<i>Test Case No.</i>	<i>Problem ID (from FE Analysis Report)</i>	<i>Mesh Refinement</i>	<i>FE Model Description</i>	<i>FE Model Illustration</i>
VP-12	26	VP-12.12	Coarse	Geometry 1, test direction 2, 1 mm radius	
	27	VP-12.13	Medium		
	28	VP-12.14	Fine		
	29	VP-12.15	Coarse	Geometry 1, test direction 2, 5 mm radius	
	30	VP-12.16	Medium		
	31	VP-12.17	Fine		
	32	VP-12.18	Coarse	Geometry 1, test direction 2, 10 mm radius	
	33	VP-12.19	Medium		
	34	VP-12.20	Fine		
	35	VP-12.21	Coarse	Geometry 1, test direction 2, 20 mm radius	
	36	VP-12.22	Medium		
37	VP-12.23	Fine			

Table B-9: VP-12 Geometry 2, test direction 1 test cases

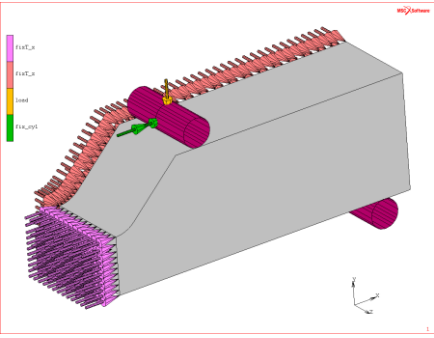
<i>VP</i>	<i>Test Case No.</i>	<i>Problem ID (from FE Analysis Report)</i>	<i>Mesh Refinement</i>	<i>FE Model Description</i>	<i>FE Model Illustration</i>
VP-12	38	VP-12.24	Coarse	Geometry 2, test direction 1, 1 mm radius	
	39	VP-12.26	Fine		
	40	VP-12.27	Coarse	Geometry 2, test direction 1, 5 mm radius	
	41	VP-12.29	Fine		
	42	VP-12.30	Coarse	Geometry 2, test direction 1, 10 mm radius	
	43	VP-12.32	Fine		
	44	VP-12.33	Coarse	Geometry 2, test direction 1, 20 mm radius	
	45	VP-12.35	Fine		

Table B-10: VP-12 Geometry 2, test direction 2 test cases

<i>VP</i>	<i>Test Case No.</i>	<i>Problem ID (from FE Analysis Report)</i>	<i>Mesh Refinement</i>	<i>FE Model Description</i>	<i>FE Model Illustration</i>
VP-12	46	VP-12.36	Coarse	Geometry 2, test direction 2, 1mm radius	
	47	VP-12.37	Medium		
	48	VP-12.38	Fine		
	49	VP-12.39	Coarse	Geometry 2, test direction 2, 5mm radius	
	50	VP-12.40	Medium		
	51	VP-12.41	Fine		
	52	VP-12.42	Coarse	Geometry 2, test direction 2, 10mm radius	
	53	VP-12.43	Medium		
	54	VP-12.44	Fine		
	55	VP-12.45	Coarse	Geometry 2, test direction 2, 20mm radius	
	56	VP-12.47	Fine		

C. APPENDIX: TEST CASE PREDICTION AT LOWER PROBABILITIES OF FAILURE

C.1 Best estimate failure predictions

Table C-1 compares the predicted failure loads to the experimentally determined median failure load for probabilities of failure (PoF) of 0.5, 10^{-2} and 10^{-4} .

Table C-1: Predicted failure loads and load scales for each test case

Test Case No.	Problem ID	Median Experimental Failure Load	0.5 PoF		10^{-2} PoF		10^{-4} PoF	
			Load Scale [%]	Predicted Load	Load Scale [%]	Predicted Load	Load Scale [%]	Predicted Load
1	VP-00.00	6.50 [kN]	100.2	6.52 [kN]	60.7	3.95 [kN]	31.5	2.05 [kN]
2	VP-00.01	6.50 [kN]	100.2	6.52 [kN]	60.8	3.95 [kN]	31.5	2.05 [kN]
3	VP-00.02	6.50 [kN]	100.2	6.52 [kN]	60.8	3.95 [kN]	31.5	2.05 [kN]
4	VP-00.03	6.50 [kN]	100.2	6.52 [kN]	60.7	3.95 [kN]	31.5	2.05 [kN]
5	VP-00.04	6.50 [kN]	100.2	6.52 [kN]	60.7	3.95 [kN]	31.5	2.05 [kN]
6	VP-00.05	6.50 [kN]	100.2	6.52 [kN]	60.8	3.95 [kN]	31.5	2.05 [kN]
7	VP-01.00	2.69 [kN]	92.1	2.47 [kN]	60.2	1.57 [kN]	30.9	0.83 [kN]
8	VP-01.01	2.69 [kN]	90.8	2.44 [kN]	57.8	1.62 [kN]	33.8	0.90 [kN]
9	VP-01.02	2.69 [kN]	92.1	2.47 [kN]	58.4	1.57 [kN]	30.9	0.83 [kN]
10	VP-19.00	24.91 [kN]	98.9	24.64 [kN]	58.8	14.65 [kN]	30.1	7.5 [kN]
11	VP-19.01	24.91 [kN]	99.0	24.66 [kN]	58.8	14.65 [kN]	30.1	7.5 [kN]
12	VP-19.02	33.74 [kN]	93.1	31.39 [kN]	55.3	18.65 [kN]	28.3	9.55 [kN]
13	VP-19.03	33.74 [kN]	93.1	31.39 [kN]	55.3	18.65 [kN]	28.3	9.55 [kN]
14	VP-12.00	9.66 [kN]	88.8	8.58 [kN]	54.1	5.23 [kN]	27.1	2.61 [kN]
15	VP-12.01	9.66 [kN]	87.6	8.46 [kN]	52.6	5.08 [kN]	22.7	2.19 [kN]
16	VP-12.02	9.66 [kN]	86.4	8.35 [kN]	52.2	5.04 [kN]	22.9	2.21 [kN]
17	VP-12.03	10.25 [kN]	93.5	9.59 [kN]	62.2	6.38 [kN]	35.7	3.65 [kN]
18	VP-12.04	10.25 [kN]	93.4	9.58 [kN]	62.1	6.37 [kN]	36.2	3.71 [kN]
19	VP-12.05	10.25 [kN]	93.5	9.58 [kN]	62.1	6.37 [kN]	36.9	3.77 [kN]
20	VP-12.06	10.99 [kN]	91.2	10.02 [kN]	59.7	6.56 [kN]	32.6	3.58 [kN]
21	VP-12.07	10.99 [kN]	90.9	9.99 [kN]	60.8	6.68 [kN]	33.8	3.71 [kN]
22	VP-12.08	10.99 [kN]	90.7	9.97 [kN]	61.3	6.73 [kN]	34.4	3.78 [kN]
23	VP-12.09	11.26 [kN]	95.3	10.74 [kN]	61.1	6.88 [kN]	32.7	3.69 [kN]
24	VP-12.10	11.26 [kN]	93.5	10.53 [kN]	60.8	6.84 [kN]	32.9	3.71 [kN]
25	VP-12.11	11.26 [kN]	93.1	10.49 [kN]	61.0	6.87 [kN]	33.3	3.75 [kN]

Test Case No.	Problem ID	Median Experimental Failure Load	0.5 PoF		10 ⁻² PoF		10 ⁻⁴ PoF	
			Load Scale [%]	Predicted Load	Load Scale [%]	Predicted Load	Load Scale [%]	Predicted Load
26	VP-12.12	7.10 [kN]	75.3	5.34 [kN]	46.8	3.32 [kN]	26.6	1.89 [kN]
27	VP-12.13	7.10 [kN]	72.9	5.17 [kN]	44.1	3.13 [kN]	21.7	1.54 [kN]
28	VP-12.14	7.10 [kN]	72.9	5.17 [kN]	36.6	2.60 [kN]	20.7	1.47 [kN]
29	VP-12.15	7.65 [kN]	81.2	6.21 [kN]	51.7	3.95 [kN]	28.0	2.14 [kN]
30	VP-12.16	7.65 [kN]	81.0	6.20 [kN]	52.4	4.00 [kN]	28.9	2.21 [kN]
31	VP-12.17	7.65 [kN]	81.0	6.20 [kN]	52.9	4.04 [kN]	29.5	2.25 [kN]
32	VP-12.18	8.01 [kN]	83.5	6.68 [kN]	51.6	4.13 [kN]	27.1	2.17 [kN]
33	VP-12.19	8.01 [kN]	81.8	6.55 [kN]	51.5	4.13 [kN]	27.4	2.20 [kN]
34	VP-12.20	8.01 [kN]	81.8	6.55 [kN]	52.3	4.12 [kN]	28.2	2.26 [kN]
35	VP-12.21	8.57 [kN]	84.9	7.28 [kN]	51.2	4.38 [kN]	26.4	2.26 [kN]
36	VP-12.22	8.57 [kN]	81.2	6.95 [kN]	49.8	4.27 [kN]	26.0	2.23 [kN]
37	VP-12.23	8.57 [kN]	81.1	6.95 [kN]	50.5	4.33 [kN]	26.5	2.28 [kN]
38	VP-12.24	4.43 [kN]	88.5	3.92 [kN]	55.2	2.44 [kN]	29.3	1.30 [kN]
39	VP-12.26	4.43 [kN]	88.4	3.91 [kN]	55.3	2.44 [kN]	29.4	1.30 [kN]
40	VP-12.27	4.17 [kN]	89.3	3.73 [kN]	55.3	2.30 [kN]	29.2	1.22 [kN]
41	VP-12.29	4.17 [kN]	89.2	3.73 [kN]	56.9	2.33 [kN]	29.7	1.24 [kN]
42	VP-12.30	4.08 [kN]	88.1	3.59 [kN]	54.7	2.23 [kN]	28.9	1.18 [kN]
43	VP-12.32	4.08 [kN]	87.5	3.57 [kN]	54.7	2.23 [kN]	29.0	1.18 [kN]
44	VP-12.33	3.91 [kN]	86.7	3.39 [kN]	53.8	2.10 [kN]	28.6	1.10 [kN]
45	VP-12.35	3.91 [kN]	86.7	3.39 [kN]	54.0	2.11 [kN]	28.6	1.11 [kN]
46	VP-12.36	2.36 [kN]	77.1	1.81 [kN]	40.8	0.96 [kN]	22.1	0.52 [kN]
47	VP-12.37	2.36 [kN]	71.8	1.69 [kN]	33.9	0.80 [kN]	18.8	0.44 [kN]
48	VP-12.38	2.36 [kN]	71.3	1.68 [kN]	34.4	0.81 [kN]	19.0	0.45 [kN]
49	VP-12.39	2.86 [kN]	85.9	2.46 [kN]	50.7	1.50 [kN]	27.5	0.79 [kN]
50	VP-12.40	2.86 [kN]	85.7	2.45 [kN]	49.7	1.42 [kN]	27.4	0.78 [kN]
51	VP-12.41	2.86 [kN]	85.6	2.45 [kN]	49.5	1.42 [kN]	27.3	0.78 [kN]
52	VP-12.42	3.09 [kN]	87.1	2.69 [kN]	54.1	1.67 [kN]	28.9	0.89 [kN]
53	VP-12.43	3.09 [kN]	86.6	2.68 [kN]	54.3	1.68 [kN]	29.4	0.91 [kN]
54	VP-12.44	3.09 [kN]	86.6	2.68 [kN]	54.6	1.69 [kN]	29.8	0.92 [kN]
55	VP-12.45	3.37 [kN]	84.2	2.84 [kN]	52.2	1.75 [kN]	27.7	0.93 [kN]
56	VP-12.47	3.37 [kN]	84.0	2.83 [kN]	53.0	1.78 [kN]	28.5	0.96 [kN]
57	VP-15.00	2.69 [MPa]	77.1	2.06 [MPa]	43.1	1.15 [MPa]	21.2	0.57 [MPa]
58	VP-15.01	2.69 [MPa]	76.5	2.05 [MPa]	42.8	1.14 [MPa]	21.0	0.56 [MPa]
59	VP-17.00	2.64 [kN]	100.9	2.67 [kN]	59.8	1.58 [kN]	30.5	0.81 [kN]
60	VP-17.01	2.64 [kN]	101.0	2.67 [kN]	59.8	1.58 [kN]	30.5	0.81 [kN]

Test Case No.	Problem ID	Median Experimental Failure Load	0.5 PoF		10⁻² PoF		10⁻⁴ PoF	
			Load Scale [%]	Predicted Load	Load Scale [%]	Predicted Load	Load Scale [%]	Predicted Load
61	VP-17.02	11.23 [kN]	89.9	10.09 [kN]	53.2	5.98 [kN]	27.2	3.05 [kN]
62	VP-17.03	11.23 [kN]	89.9	10.10 [kN]	53.3	5.98 [kN]	27.2	3.05 [kN]
63	VP-18.00	10.14 [MPa]	67.2	6.81 [MPa]	39.5	4.00 [MPa]	20.0	2.03 [MPa]
64	VP-18.01	10.14 [MPa]	67.2	6.80 [MPa]	39.4	4.00 [MPa]	20.0	2.03 [MPa]
65	VP-18.02	10.14 [MPa]	67.2	6.81 [MPa]	39.5	4.00 [MPa]	20.1	2.03 [MPa]
66	VP-18.03	34.82 [MPa]	50.0	17.42 [MPa]	29.0	10.10 [MPa]	14.6	5.08 [MPa]
67	VP-18.04	34.82 [MPa]	50.0	17.42 [MPa]	29.0	10.09 [MPa]	14.6	5.08 [MPa]
68	VP-18.05	34.82 [MPa]	50.1	17.44 MPa	29.1	10.12 MPa	14.6	5.09 [MPa]

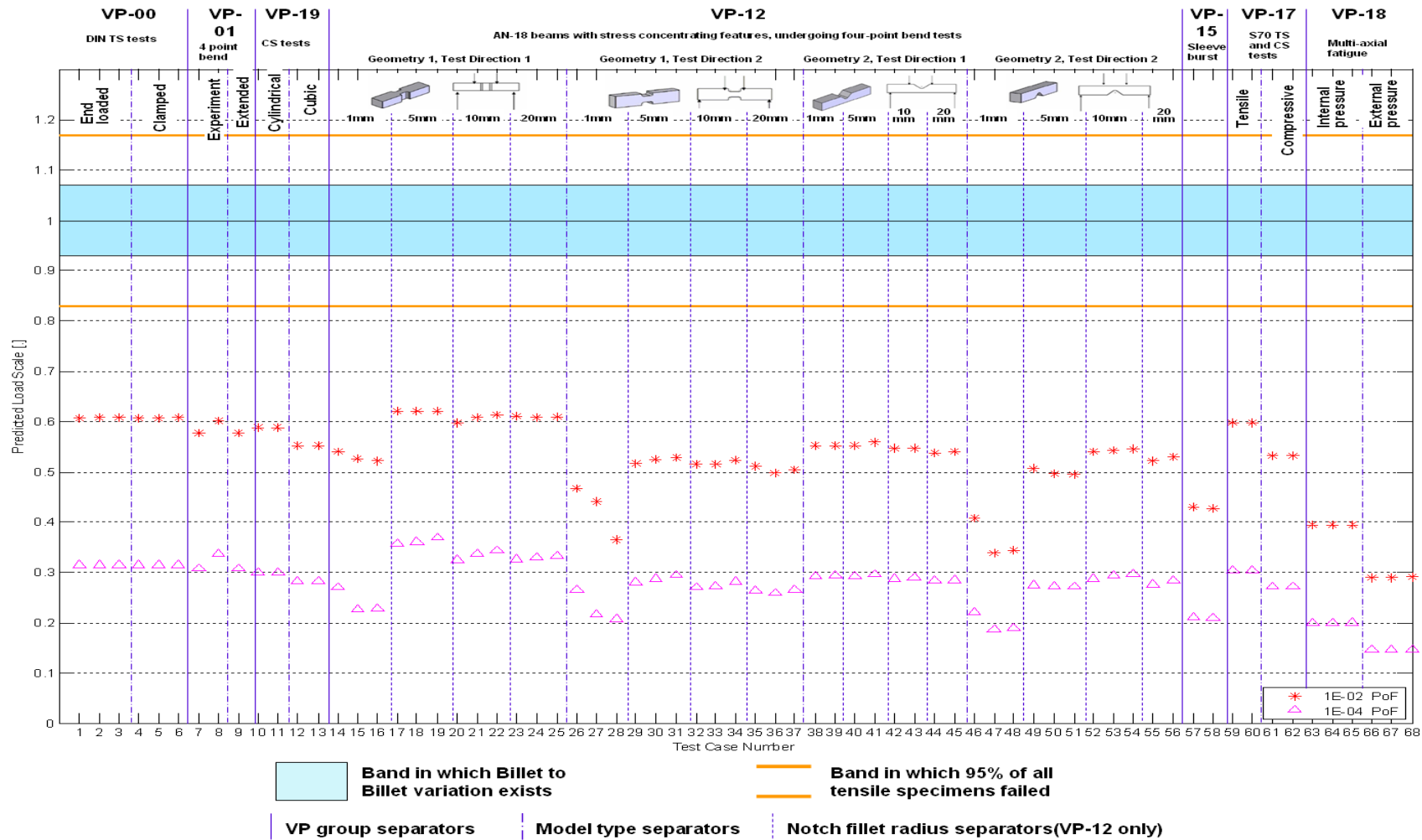


Figure C-1: Back off limit failure prediction

C.1.1 General trends and observations at median failure load

In general, the most accurate median failure load predictions (0.5 PoF data points lying close to 1.0) are made for specimens experiencing a uni-axial (or approximately uni-axial) stress state. The least accurate predictions are made for the multi-axial fatigue specimens (undergoing static loading) and notched beams with 1 mm fillet radii, which cause very localised stress concentrations.

With the exception of the uni-axial tensile specimens, all predictions fell on the conservative side of the experimental median failure loads. 0.5 PoF load predictions were within 2% of the experimentally determined median failure loads for uni-axial tensile specimens, with slightly non-conservative predictions.

C.2.1 Group observations at median failure load

C.1.2.1 VP-00: Tensile strength test

Test cases 1 to 6 represent the VP-00 failure methodology comparisons with the experiment. This is the test case for which the most experimental measurements are available. Three finite element (FE) meshes of varying refinement were analysed under two different methods of load application. Predicted failure loads for a 0.5 PoF agree to within 2% of the experimentally determined median failure load for all six test cases. Close agreement like this is expected in problems with a uni-axial stress state, upon which the failure methodology is based.

Stress solution convergence between the three meshes has been demonstrated in Mcmurty [96]. The load scales agree to within 0.1% between meshes, indicating that the methodology is not sensitive to the refinement of the FE mesh, at least as long as the stress solution is converged.

Two different methods of load application were modelled; a non-physical end-loaded model in test cases 1 to 3, and a simulation of a specimen clamped in the test rig in test cases 4 to 6. Less than 0.2% difference in the load scales between models indicates that the failure methodology predictions are mainly influenced by the peak stresses in the failure region and less so by smaller stresses away from the specimen gauge region.

C.1.2.2 VP-01: Four-point bend tests on cylindrical specimens

Test cases 7 to 9 represent the VP-01 failure methodology comparisons with the experiment. Cases 7 and 8 compare medium and fine FE mesh solutions. Case 9 investigates the effect of extending the specimen lengthwise beyond the test rig supports, away from the stressed region, in order to test the theory that extra unstressed material should not alter the PoF prediction. For further details on the FE models see Erasmus [93].

Between the medium and fine meshes for the non-extended model there is a small difference of 1.4% in the predicted loads for 0.5 PoF, which is comparable to the difference in the predicted peak stresses which were found to be 0.9% in Mcmurty [99].

As expected, there is no difference in the predicted loads for 0.5 PoF between the non-extended and extended models with medium refinement meshes. This is because the high-stress region, where high probabilities of failure are calculated, is not affected by the extended sections of the model.

C.1.2.3 VP-19: Compressive strength test

Test cases 10 to 13 represent the VP-19 failure methodology comparisons with the experiment. Cases 10 and 11 represent the cylindrical specimen model with a coarse and fine mesh, respectively. Cases 12 and 13 represent the cubic specimen model with a coarse and fine mesh, respectively.

Negligible difference is observed between the predicted failure loads for the coarse and fine meshes for either the cube or cylindrical model. This is as expected as stress solution convergence for the models has been demonstrated in Mcmurty [98].

Predicted failure loads for a 0.5 PoF agree to within 1% of the experimentally determined median failure load for the cylindrical model and to within 7% for the cubic model. Predicted failure loads are lower than the experimentally determined median failure loads for both models, thus making the methodology conservative in these test cases.

The reason for the ~6% difference in prediction accuracy between the cylindrical and cubic models is due to the fact that the tensile strength (TS) to compressive strength (CS) ratio used in the stress intensity calculation (see Section 7.3.2) is biased by the cylindrical specimens, for which much more test data were available (228 cylindrical specimens tested as opposed to 24 cubic specimens). The difference between the median CS measured on cylindrical and cubic specimens is 6.4%, with a lower strength measured for the cylinders.

Therefore, as the assumed CS used in the stress intensity calculation for the cube is lower than it really is for that specimen geometry, an extra degree of conservatism is added in the PoF prediction for the cubic test cases.

C.1.2.4 VP-12: AN-18 beams with stress-concentrating features

Test cases 14 to 56 represent the VP-12 failure methodology comparisons with the experiment. These four-point bend tests on beams with stress-concentrating geometric features were performed on two different specimen geometries: dogbone-shaped and V-notched, referred to as geometry 1 and geometry 2, respectively. Each geometry was tested in two different loading directions. In addition, specimens were tested with four different fillet radii (1 mm, 5 mm, 10 mm, 20 mm) at the notches. Illustrations and labelling is provided in Figure 7-2 to help differentiate between the various test cases. Mcmurty [99] documents the FE analyses for the VP-12 test cases.

As all of the VP-12 test cases have stress-concentrating geometric features, Mcmurty [99] has a strong focus on mesh refinement and demonstrating that stress solution convergence has been achieved for each model. It must be noted that for some of the VP-12 test cases used in this failure methodology comparison, the stress solutions are not converged. These test cases are still of

interest in order to assess the sensitivity of predicted PoF to stress solution convergence.

For VP-12 models where only two FE meshes were analysed (geometry 2, test direction 1 all fillet radii, and geometry 2, test direction 2, 20 mm radii only), stress solutions were found to be in acceptable agreement on first iteration. For the other VP-12 models, an extra iteration was required to obtain acceptable stresses between meshes, and failure comparison results for three different FE meshes are presented for each model. Mesh refinement increases from left to right for each model in Figure 7-2. Therefore, the left-most data points for the models with three compared meshes represent a non-converged stress solution.

Excepting the case of geometry 2, test direction 1, failure predictions for 1 mm fillet radius specimens are significantly more conservative than for other radii specimens. Within similar geometry and test direction groups, there is less than 5% difference in the predicted load scales for 5 mm, 10 mm and 20 mm specimens at PoFs of 0.5, even including the predictions for non-converged stress states.

Fillet radius has little effect on the prediction accuracy for the geometry 2, test direction 1 problems. This is because the region of peak stress intensity, and therefore high PoF, is located away from the root of the notch (see Mcmurty [99] for illustration) due to the direction of load application to the specimen.

The most accurate VP-12 0.5 PoF predictions are made for geometry 1, test direction 1, 20 mm fillet radius, with a predicted failure load within 6% of the experimentally determined median. This specimen and load application direction results in the least pronounced stress concentration of the VP-12 test cases and hence most accurate failure prediction.

The predicted failure load is seen (unsurprisingly) to have a significant sensitivity to mesh refinement, and hence stress solution convergence for some test cases, while in other test cases the differences are less pronounced. For the converged stress solution test case comparisons, however, predicted failure load scales agreed to within 0.6% for all test cases, while the peak stresses calculated in the failure regions for these test cases varied on average by 1.0% and by up to a maximum of 2.6%.

In effect, the failure prediction methodology appears to exhibit the useful characteristic of not being overly sensitive to the refinement of the FE mesh. This is probably because the calculations are based upon element volumes and the stresses are calculated within them, at the Gauss points, rather than at the peak stresses as extrapolated to the material surface.

C.1.2.5 VP-15: Sleeve burst test

Test cases 57 and 58 represent the VP-15 sleeve burst tests. The graphite sleeves were placed under an increasing internal pressure until rupture. Two FE meshes of different refinement were analysed as described in Mcmurty [101].

The difference between predicted failure loads at 0.5 PoF is less than 1% between FE meshes. This is expected as the peak stress intensities are shown to be within 1% in reference [101].

The predicted failure loads for a 0.5 PoF agree to within 23% of the experimentally determined median failure load for both FE meshes. This VP has an absence of stress-concentrating features in the sleeve geometry and the sleeve is thin walled, leading to a fairly uniform peak hoop stress.

C.1.2.6 VP-17: S70 uni-axial tension and compression tests

Test cases 59 to 62 represent the VP-17 tests of S70 specimens undergoing uni-axial TS and CS tests. Although these specimens were designed for fatigue testing, a small number of static strength tests were carried out as well. Only the static test cases are of interest in this analysis. Two FE meshes of different refinement were analysed for both the tensile and compressive models as described in Roberts [20]. Test case numbers 59 and 60 represent the tensile models. Predicted failure loads for a PoF of 0.5 agree to within 1% of the experimentally determined median failure load for both FE meshes. The accuracy of prediction is comparable to that for VP-00, the other uni-axial tension case discussed in Section C.1.2.1.

Test case numbers 61 and 62 represent the compressive models. Predicted failure loads for a PoF of 0.5 agree to within 10% of the experimentally determined median failure load for both FE meshes. This error is approximately 8% greater than that for the VP-19 cylindrical specimen discussed in Section C1.2.3. This is largely due to the fact that the experimentally measured median CS is higher (8%) for the S70 specimens than for the VP-00 cylinders.

The TS to CS ratio used in the stress intensity calculation (see Section 6) is biased by the cylindrical specimen measurements for which much more test data were available. Therefore, as the assumed CS used in the stress intensity calculation for the compressive S70 specimens is lower than it really is, an extra degree of conservatism is added in the PoF prediction.

The load scales agree to within 0.1% between meshes, indicating that the methodology is not sensitive to the refinement of the FE mesh, at least as long as the stress solution is converged.

C.1.2.7 VP-18: S60B multi-axial tension and compression tests

Test cases 63 to 68 represent the VP-18 tests of S60B specimens undergoing multi-axial TS and CS tests [20]. Although these specimens were designed for fatigue testing, a small number of static strength tests were carried out as well. Only the static test cases are of interest in this analysis. The hollow, dome-like specimens were placed in tension and compression by applying an internal and external pressure, respectively.

Test cases 63 through 65 represent the specimens under tension. Predicted failure loads for a PoF of 0.5 differ from the experimentally determined median failure load by 33% for each FE mesh.

Test cases 66 through 68 represent the specimens under compression. Predicted failure loads for a PoF of 0.5 differ from the experimentally determined median failure load by 50% for each FE mesh.

The 0.5 PoF load predictions made for the VP-18 test cases are among the worst of all 68 test cases in terms of accuracy.

The larger errors observed in these multi-axial problems are probably due to the inability of the failure methodology to take into account the stress and geometric stiffening occurring in these test cases, which effectively allows the material to withstand greater stresses without failing. However, all the VP-18 predictions err on the conservative side.

The load scales agree to within 0.1% between meshes, indicating that the methodology is not sensitive to the refinement of the FE mesh, at least as long as the stress solution is converged

C.2 Effect of finite element mesh refinement on prediction trends

Section C.1.2.1 discussed inconsistencies observed in the spread of load scale predictions between different FE meshes of the same models. These inconsistent trends can be shown to be due to the numerical implementation of the failure methodology, which is based upon the sorting, grouping and volumetric integration of stresses in discrete regions of the part, according to the stress magnitudes calculated in each. This section explains the phenomenon, using the four-point bend tests on cylindrical samples (VP-01) as an example. Figure C-2 is the cumulative distribution plot for the VP-01 problem, comparing the numerical predictions calculated using the coarse and fine FE meshes (the test data is also plotted for comparison). As the FE meshes are different, the Gauss point positions, associated volumes and stress intensity magnitudes will also be different. Hence the Gauss point results grouping is carried out differently for the different FE meshes. In Figure C-2 two points of interest have been identified, Line "A" which is at a PoF of 0.5 and Line "B" which is at a PoF of $1e-2$. At a PoF of 0.5 the coarse mesh is slightly more conservative than the fine mesh. At a PoF of $1e-2$ the fine mesh is more conservative than the coarse mesh. At low PoFs the stressed volume is very small and the fine mesh will group a smaller volume than the coarse mesh and subsequently deliver a more conservative answer.

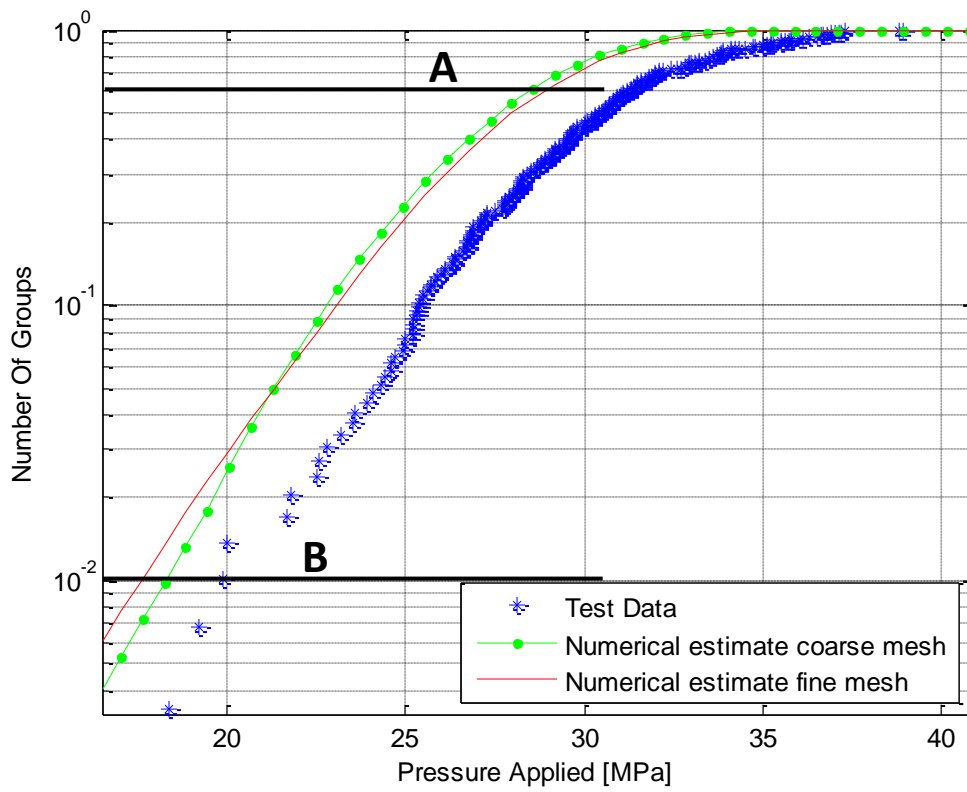


Figure C-2: Cumulative distribution plot for VP-01 with a log scale for clarity at low failure probabilities: comparing test data with predictions for two finite element meshes of different refinement

D. APPENDIX: MATLAB IMPLEMENTATION OF FAILURE METHODOLOGY

```

function [out] = hind_08(FileName,matdat,ps,gs)
%*****
% Inverse PoF cacluation.
% Read output from marc and calculate the load at which a given
failure
% probability is reached.
% By Michael Hindley
%*****
% Inputs:
% 1. FinaName : Name of the input data frile with the problem
data in it.
% 2. matdat : The material data file to be used for the problem.
% 3. ps : Target Probability of failure.
% 4. gs : Geometry Scale Factor. Allow for if the results are
for a
% partial FEA model.
%*****
% Returns
% out(1): max(data(:,2)). Maximum stress value.
% out(2): volume_int | the volume over which integration was
completed.
% out(3): volume_tot | the total volume of the problem (this
includes the
% geometry scaling).
% out(4): volume_90 | Volume of material that is stressed to
90% or more
% of the maximum stress.
% out(5): strmult
% out(6): xlv1
% out(7): v1
% out(8): dvall
% out(9): groups
% out(10): S0
%*****

%vrat = 0.90;
out = [ 0 0 0 0 0];

% define console output mode.
verbose = 1;

%Parameters
rg = 0.0016 ;
%Alpha=9.73;
Alpha=14.45;

```

```

vm = (Alpha*rg)^3 ; % volume of the maximum grain size
%delta = 0.00001; % not what is described in the docuemnt!
%delta = 0.20;
delta = 0.9975;

% convert the material data inputs to internal file variables.
Sc = matdat(1) ;
m = matdat(2) ;
compratio = matdat(3);
Nu(1) = matdat(4);
S0 = matdat(5);

% print problem outputs.
if verbose == 1
    disp(FileName);
    disp(sprintf('Sc = %1.3f [MPa]', Sc/1e6))
    disp(sprintf('S0 = %1.3f [MPa]', S0/1e6))
    disp(sprintf('m = %1.3f', m))
    disp(sprintf('R = %1.3f', compratio))
    disp(sprintf('nu = %1.3f\n', Nu(1)))
end

% load the problem into memory. Preporcess the file. This data is
sorted by
% equivalent stress value as well.
data2 = LoadDataFile(FileName,matdat);

%scale the volume of the model
data2(:,1) = gs.*data2(:,1);

% calculate the total volume of the problem (this includes the
geometry scaling).
volume_tot = sum(data2(:,1));

% intialise internal variables.
% strmults = [0.1:0.1:2];
strmults = [];
Lcs = [];
% for ii=1:length(strmults)
stop = 0;
strmult = 1;
dsm = 0.5;
ns = 0;
dx = 0;

while (stop ~= 1)

    ns = ns+1;
    strmults = [strmults strmult];
    data = data2;
    data(:,2) = strmult .* data2(:,2) ;
    S0 = matdat(5);

    % Now scale the thershold stress to ensure that it is never
zero.

```

```

%     full=max(data(:,2));
%     if full < Sc
%         S0=(full/Sc)*S0;
%     end

% edited. MNM 090522 - Remove the S0 scaling to be pure .
full=max(data(:,2));
if full < Sc
    S0= (full/Sc) * S0;
end

% truncate all stress values below the threshold.
%data(:,2) = (data(:,2) > S0) .* data(:,2);

n = sum((data(:,2) > S0));

%     hist(data(1:n,2));
%     pause

if verbose==1
    % Show the number of points that we count over.
    disp(sprintf('Integration over %d of %d data
points.',n,length(data(:,2))));
end

volume_int = sum(data(1:n,1));

volume_90 = sum( (data(:,2)>0.9*max(data(:,2))).* (data(:,1))
);

% Initialise the Xi value array. 090522. No effect.
data(1:length(data(:,1)),3) = zeros(size(data(:,1)));

% Compute the Xi values.
data(1:n,3) = ((data(1:n,2) - S0)./(Sc-S0)) .^m;

lvs = [];

i0 = 1;
i1 = i0;
% now hunt for i1 that meets the criteria:

%Vsi = sum(data(i0:i1,1)); % changed to improve speed. 7-Jun-
08
Vsi = data(i0,1);
while (i1<n)
    % increment i1
    i1 = i1+1;

    % check if the criteria are met.
    % compute the volume for the group.

```

```

08      Vsi = Vsi + data(i1,1); % changed to improve speed. 7-Jun-
% note that the behaviour around 1/2 and 1/4 models needs
to be % considered. The volume is already factored in but should
more be % done as this lumps failure sites.

if (Vsi >= vm) || (i1>=n)
    % changed to improve speed. 7-Jun-08
    dval = abs(data(i1,3)-data(i0,3))/data(i0,3);

    if ( dval >= delta) || (i1>=n)
        % we can complete the integration.

        XiVi = data(i0:i1,3) .* data(i0:i1,1);

        % This is just for auxillairy debug info.
        if length(lvs) <1
            xlv1=sum(XiVi);
            v1=Vsi;
            dval1=dval;
        end

        lvs = [lvs exp(-sum(XiVi)/Vsi)];

        %disp(sprintf('%d,%d] : Delta = %1.6e : LI =
%1.6e ',...
            %i0,i1,max(data(i0:i1,3)) - min(data(i0:i1,3)),
exp(-sum(XiVi)/Vsi) ));

        % it appears in this case the i1 point is computed
twice.

        ii = i1+1; %090522
        i0 = i1;

        % 090522 Fix. reset the volume integration.
        %          Vsi
        Vsi = data(i0,1);
    end
end
end
%      disp(sprintf('%d,%d',i0,i1))

% compute the component life.
groups=length(lvs);
Lc = prod(lvs);
if verbose == 1
    disp(sprintf('Strmult: %1.3f = Failure Probability: %1.3e
and number of groups %2.2f',strmult ,(1-Lc),groups))
end

```

```

Lcs = [Lcs Lc];
if (ns>1)
    if (ns==2) && (Lc < 0.5) && (strmult>=0.5)
        strmult = 1e-6;
    else

        dx = strmult;

        if ps<0.9

            [val,mx] = min(((ps-Lcs)>0).*strmults + ((ps-
Lcs)<0).*100);
            [val,nx] = max(((ps-Lcs)<0).*strmults + ((ps-
Lcs)>0).*-100);

            x=[strmults(mx) strmults(nx)];
            y=[Lcs(mx) Lcs(nx)];

            % now interpolate linearly to find the value at
0.5

            %           ps2
            strmult = (ps*x(1)-ps*x(2)+x(2)*y(1)-
x(1)*y(2))/(y(1)-y(2));
            else
            [val,mx] = min(((ps-Lcs)>0).*strmults + ((ps-
Lcs)<0).*100);
            [val,nx] = max(((ps-Lcs)<0).*strmults + ((ps-
Lcs)>0).*-100);

            x=[strmults(mx) strmults(nx)];
            y=[Lcs(mx) Lcs(nx)];
            y = y - ((1-y)<1e-12).* (1e-12 );
            y=log10(1 - y);

            % now interpolate linearly to find the value at ps

            ps2 = log10(1-ps);

            strmult = (ps2*x(1)-ps2*x(2)+x(2)*y(1)-
x(1)*y(2))/(y(1)-y(2));

            end

            if abs((strmult-dx)/dx) < 0.0001 % close enough for
initial work.

                stop = 1;
            end

```

```
        end

    else

        if (Lc > ps)
            strmult = strmult + dsm;
        else
            strmult = strmult - dsm;
        end

    end

    if strmult < 1e-6
        strmult = 1e-6;
    end
    %   strmult

    %   if (ns > 2)
    %       return
    %   end

end

out = [max(data(:,2)) volume_int volume_tot volume_90 strmult
xlvl v1 dval1 groups S0];

return
```